Bulk optical properties and magnetic properties of monolayers of Er(III) cyclooctatetraenide-based single-molecule magnets

Inauguraldissertation
zur
Erlangung der Würde eines Doktors der Philosophie
vorgelegt der
Philosophisch-Naturwissenschaftlichen Fakultät
der Universität Basel

von

Vladyslav Romankov

2024

Genehmigt von der Philosophisch-Naturwissenschaftlichen Fakultät

auf Antrag von

First Supervisor: Prof. Dr. Frithjof Nolting, Dr. Jan Dreiser

Second Supervisor: Prof. Dr. Ernst Meyer

External expert: Dr. Markus Etzkorn

Basel, 19.09.2023

Prof. Dr. Marcel Mayor, Dekan

Abstract

Fundamental investigation in the field of molecular complexes displaying magnetic hysteresis opening, called single-molecule magnets (SMMs), has been very active in the past few decades for the outstanding magnetic properties and potential technological applications displayed by these compounds. Sandwich lanthanide organometallic complexes have recently been reported displaying magnetic bistability up to 80 K, which is very interesting for potential applications in technology featuring spintronics systems and data storage devices. However, the study of these systems deposited on metal substrates has shown that the hysteresis opening tends to be lost due to the interaction of the complexes with the surface in the monolayer regime. SMMs with planar ligands like cyclooctatetraenide (COT^{2-}) dianion and pentamethyl-cyclopentadienide (Cp*) anion are good candidates to form ordered layers on surfaces, although the self-assembly and the complex-substrate interaction can play a fundamental role in the properties of those systems. Moreover, complexes containing the trivalent Er ion have potential use in spintronic technology through the optical manipulation of the electronic states in the 4f shell. The details of the ligand field effect on the intra-4f transitions in the near-infrared range often remain elusive, relying on simulations or indirect techniques.

We present a study of the molecular self-assembly and the magnetic properties of two sandwich Er^{3+} COT^{2-}-based SMMs deposited on the (100) surface of an Ag crystal in the monolayer range and a comparison of the optical properties of four structurally similar sandwich Er^{3+} SMMs in the infrared region. Combining low-temperature scanning-tunneling microscopy, X-ray photoemission spectroscopy and polarized X-ray absorption spectroscopy we show that the heteroleptic Cp*ErCOT complex self-assembles in a mixed standing-up and lying-down configuration forming alternating compact parallel rows, oriented parallel to the crystallographic [010] and [001] directions of the surface. On the other side, the homoleptic $K[Er(COT)_2]$ complex, produced from the sublimation of $[K(18\text{-c-}6)][Er(COT)_2]\cdot 2THF$ precursor (18-c-6 = 18-crown-6 ether, THF = tetrahydrofuran), forms ordered domains with the COT rings standing perpendicular to the substrate and the complexes aligned along specific directions.

The polarization-dependent X-ray absorption spectra are compared to the simulations performed by multiX, an ab-initio model based on point charges emulating the electrostatic effect acting onto the central Er ion. The simulations suggest that the strong in-plane magnetic anisotropy of $K[Er(COT)_2]$/Ag(100) and the mixed in-plane and out-of-plane magnetization of Cp*ErCOT/Ag(100) can be attributed to the strikingly different surface ordering of these two complexes. With comparison to

the magnetic properties of the bulk precursors, the surface-supported K[Er(COT)$_2$] shows a similar large hysteresis opening, while Cp*ErCOT shows a rather small opening. The different net magnetic properties on the metal substrate are attributed to the different orientation/interactions of the ligand rings to the surface.

At the same time, Fourier-transform infrared spectroscopy in the range of the transitions between the Er^{3+} ground state ($^4I_{15/2}$) and the first excited state ($^4I_{13/2}$) manifolds unveils the ligand-field induced differences of four Er^{3+}-based SMMs. While [K(18-c-6)][Er(COT)$_2$]·2THF displays few intra-4f transitions attributed to the low admixing of different m_J states, [Li(DME)$_3$][Er(COT")$_2$] (COT" = bis(trimethylsilyl)-cyclooctatetraenide; DME = dimethoxyethane), Cp*ErCOT and Cp^{ttt}ErCOT (Cp^{ttt} = tris(tert-butyl)cyclopentadienide) complexes show multiple transitions due to a stronger admixing of states. The differences are attributed to the details of the ligand field induced by the different aromatic rings in the different complexes.

Moreover, the splitting of 4f-4f transition peaks at low temperature is attributed to the presence of static disorder of the complexes in the form of different stacking configurations (rotamers) of the ligands. Temperature-dependent spectra reveal thermally activated vibrations of the ligand rings, with activation energies in range of those found for $FeCp_2$ and CpTiCOT. The results show how the temperature affects the dynamics of the complexes featuring COT and/or Cp* ligands and how this influences the intra-4f transitions.

IN conclusion, the study how the substitution of one or both ligand rings of structurally similar Er^{3+}-based sandwich SMMs can drastically affect the magnetic properties in the monolayer range on Ag(100) and the optical properties of those compounds in bulk. Specifically, the research sheds light on the behavior and suggests the key parameters affecting the SMM properties on metal surfaces and the intra-4f transitions in the NIR window of Er^{3+}-based organometallic sandwich complexes, giving a novel insight into these technologically promising complexes and lying the base to improve the design and understanding of similar systems.

Table of Contents

Chapter 1
Er(III) – based single-molecule magnets

1.1 Introduction

Molecules are small groups of atoms bound together that span in the sub- to nanometer scale size and constitute the core units of all our daily aspects, from biological entities to technology and to all those compounds that make life itself possible. The understanding of the chemical properties and the physical behavior of the different molecules brings answers regarding the mechanisms governing nature and helps to improve the quality of life of the human species and its surroundings. To achieve that, the scientific community have learned to design and engineer new molecular compounds to tailor specific desired properties. In particular, small clusters of metallic ions coordinated with organic and/or inorganic ligand molecules gained an increasingly higher interest in the past years after manifesting interesting magnetic properties. About 30 years ago, a poly-nuclear molecular cluster based on manganese ions, nicknamed “Mn12-ac”, was reported to exhibit a residual magnetization, also called remanence, after applying an external magnetic field at temperatures below 4 K.[1,2] The discovery showed that at those temperatures the Mn12-ac manifests magnetic hysteresis opening of an entirely molecular origin, which before was known to be a typical behavior found in classical 3d-metal ferromagnets. Contrary to ferromagnets, this compound displayed strong magnetization without the necessity of long-range ordering of its units, meaning that each one of these molecules could be considered as a single magnet of nanometer size. The cluster was the first example of a family of compounds called single-molecule magnets (SMMs), molecular aggregates that exhibit slow relaxation of magnetization below a certain temperature T_B, called blocking temperature. The effect itself consists of an anisotropic bipolar uniaxial orientation of the magnetization given by the metal ion(s) for a certain characteristic time, which can span from milliseconds to several hours.[3] The bipolar orientation of the magnetization is given by the so-called magnetic bistability[2] of the systems, since two stable magnetic states with opposite directions of the magnetization are separated by an energy barrier. In most cases, the thermal fluctuations at room temperature stimulate the crossing of this barrier, which forces to keep the temperatures of these compounds close to zero Kelvin in order to observe the SMM behavior.

The magnetic bistability of single-molecule magnets generated a great interest in the scientific community due to potential applications in data storage devices and spintronics, since SMMs can remain magnetized in either of the two "spin" states.[4] Moreover, the sub-nanometer size of the SMMs make them very appealing for the storage of information given the higher density of "bits" these systems can offer when compared to the current CMOS technology. The information is stored for a characteristic time, which depends on the system, temperature and the relaxation processes that affect the compounds, described in detail in the next section. A sub-category of SMMs includes complexes based on a single metal ion of the 3d or 4f series, called also single-ion magnets (SIMs). SIMs bound to ligands containing carbon bonds are also referred to as organometallic complexes, which are the central topic of the current thesis. Organometallic complexes have shown to display outstanding magnetic properties through an opportune choice of ligands and coordination environment,[3,5–7] especially when using lanthanide atoms due to their large unquenched orbital magnetic moments and accessibility to high spin-orbit ground states.[8,9]

The use of aromatic phthalocyanine dianion (Pc^{2-}), cyclopentadienide (Cp^{-}) and/or cyclooctatetraenide (COT^{2-}) ligands and their derivatives have shown to induce large magnetic anisotropy on trivalent lanthanides in sandwich-type complexes, especially when using Tb^{3+}, Dy^{3+} and Er^{3+} ions.[10–16] Such complexes have displayed an exceptional potential for technology applications, especially when in 2018 one of these compounds, a metallocene containing Dy^{3+}, showed a very large effective energy barrier to reversal of the magnetization, manifesting hysteresis opening up to 80 K.[17] This showed that such systems could operate at above the liquid nitrogen temperature, further fueling the research of complexes with even higher energy barriers.

To move toward device application, it is also very important that those complexes can be transferred on suitable surfaces, often metals to simulate typical interfaces in devices. In many cases, the systems are fragile and/or air-sensitive, making the deposition process itself a big challenge. Also, the arrangement and self-assembly of those complexes on surfaces influences both the magnetic properties and the accessibility to the information carried by SMMs.[18] Indeed, molecule-substrate interaction have proven to be a crucial factor affecting the molecular magnetization, as several studies of SMMs with large hysteresis loop openings in the bulk showed poor magnetic properties upon deposition on substrates due to fast relaxation rates of the magnetization.[19–24] In other cases, strong complex-surface interaction can promote charge transfer that alters the magnetic properties of compounds on metals in the regime of a single layer of these complexes.[25] The exceptions usually rely on the use of buffer layers, non-magnetic and often insulating spacer materials between the substrate and the complexes, to quench relaxation pathways.[26,27] For this reasons, when transferring these complexes on the surface it is important to ensure the structural integrity and the preservation of the

bulk magnetic properties in the regime of single complexes interacting with the substrate. One of the main research topics discussed in the current text is connected to these two fundamental characters of few structurally similar Er(III)-based SMMs, which are introduced and explained in the following Section.

1.2 Er(III)-cyclooctatetraenide SMMs

1,3,5,7-Cyclooctatetraene (COT)[28] is a polyunsaturated hydrocarbon with formula C_8H_8 whose dianion, cyclooctatetraenide (COT^{2-}), forms a planar aromatic ring, commonly used in the synthesis of coordination compounds containing lanthanides and actinides.[29–32] The peculiarity of this dianion is that it has π orbitals oriented perpendicular to the plane containing the ring, with a doubly-negative charge delocalized across the orbitals of the carbon atoms. It was shown that homoleptic complexes including the $[Er(COT)_2]^-$ anion in form of a sandwich of two cyclooctatetraenide rings and a central Er ion in the trivalent state manifests SMMs properties up to ~10 K, due to the planar ligand field of the COTs around the prolate ground state of the lanthanide.[32,33] The synthesis of the neutral complex containing this anion usually requires the presence of a cation featuring potassium, like the $[K(18\text{-c-}6)]^+$ (with 18-c-6 = 18-crown-6 ether), and sometimes the tetrahydrofuran (THF) solvent. The organometallic complex containing both is called $[K(18\text{-c-}6)][Er(COT)_2]\cdot 2THF$ and it displays a strong magnetic anisotropy along the axis that goes through the Er^{3+} and the two almost-parallel COT^{2-} ligands, shown in Figure 1.1a.[32] The COT rings form a dihedral angle of 2.8° between the planes containing them (at 240 K), departing from the otherwise perfect D_{8h} symmetry, which affects the electronic properties of the compound and the relaxation of the magnetization, addressed further below. In addition, the complex shows static disorder over two conformations in the staggered and eclipsed positions of the rings with respect to each other, shown by the top-view in Figure 1.1b, impacting even more the electronic properties, as explained further on in this Chapter. In general, the $[Er(COT)_2]^-$ anion generated great interest in the scientific community as a highly symmetric magnetic unit and a prototype system to understand the effect of COT ligands and their functionalized versions on late lanthanides, with the purpose of enhancing the magnetic anisotropy and the SMM behavior of these compounds.[33–37]

One of the compounds based on a sandwich complex containing the functionalized 1,4-bis(trimethylsilyl)cyclooctatetraenide dianion (COT"), namely $[Li(DME)_3][Er(COT")_2]$, was shown to have SMM properties.[37] The complex, shown in Figure 1.1c, displays magnetic hysteresis opening up to 8 K and uniaxial magnetic anisotropy along the pseudo-rotational axis that goes between the center of the COT"s and the lanthanide, similarly to the non-functionalized erbium bis-COT from above.

Similarly, the $[Er(COT'')_2]^-$ anion deviates from a perfect linear structure by a larger dihedral angle of 3.6° between the planes of the ligands. Also, the functionalization of the COTs with the silyl groups reduces even more the symmetry of the anion, affecting the ligand field and the ground state of the complex, as explained further below.

Heteroleptic sandwich complexes based on an Er ion and containing the COT ligand have also been reported to show magnetic hysteresis openings and axial magnetic anisotropy, as in the case of Cp*ErCOT and Cp^{ttt}ErCOT (with Cp* = 1,2,3,4,5-pentamethylcyclopentadienide, Cp^{ttt} = tris(tert-butyl)cyclopentadienide).[38,39] The Cp*ErCOT is a neutral complex showing SMM behavior up to 5 K, with the structure in Figure 1.1.d.[38] This organometallic complex features a derivative of the cyclopentadienide, a ligand anion widely used in the synthesis of metallocenes.[40,41] The crystallographic data of the complex show the presence of two static conformers (rotamers) at 10 K, which can be represented as in the top-view sketch shown in Figure 1.1e. Just as the previous compounds, the planes containing the two ligand rings have a dihedral angle of 8.0°. This compound was also extensively studied with the aim to understand its anisotropy and its magnetic behavior in the polycrystalline bulk phase.[42–44]

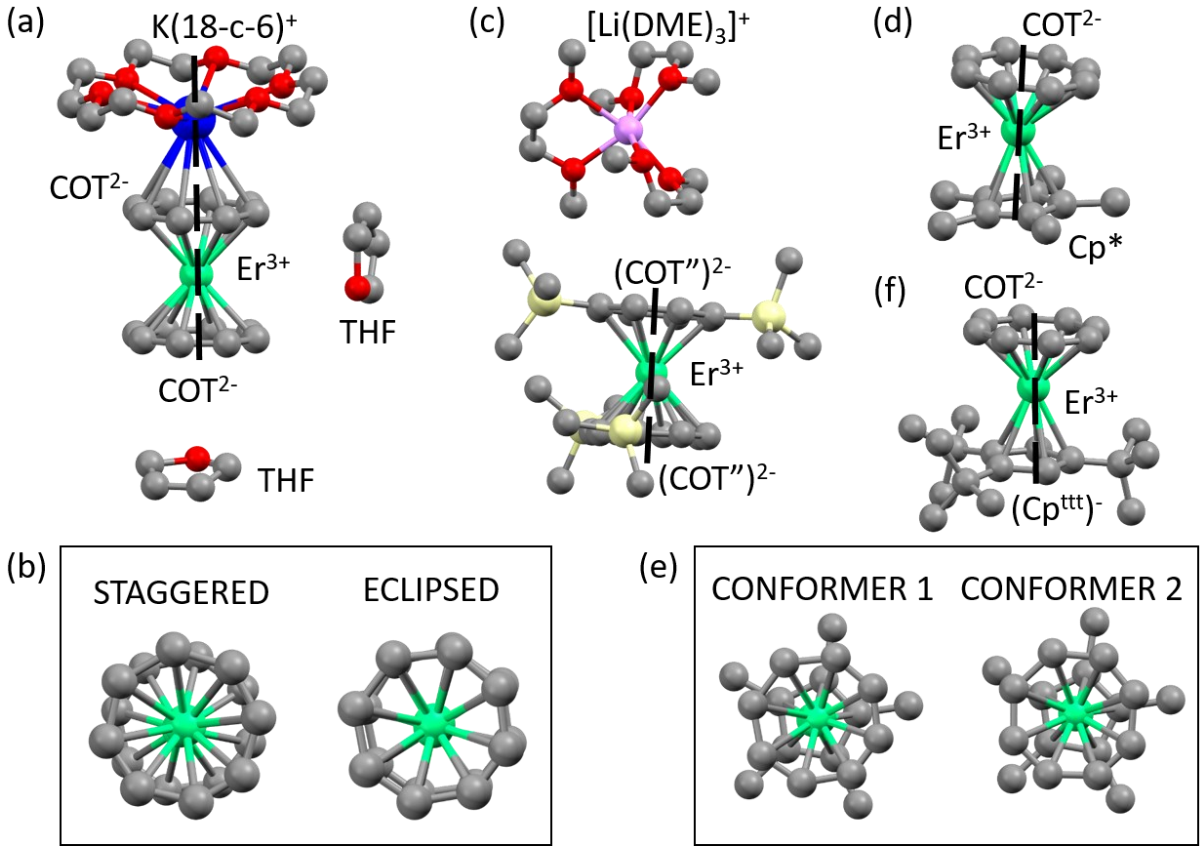

Figure 1.1. Molecular structure of (a) $[K(18\text{-c-}6)][Er(COT)_2]\cdot 2THF$ and (b) the two static conformers of the $[Er(COT)_2]^-$ anion,[32] (c) $[Li(DME)_3][Er(COT'')_2]$,[37] (d) Cp*ErCOT and (e) its two static conformers,[38] and (f) Cp^{ttt}ErCOT SMMs,[39] obtained from published CIF files. Color code: green is Er, grey is C, red is O, blue is K, pink is Li and yellow is Si. Hydrogens are omitted for simplicity.

The Cp^{ttt}ErCOT is another heteroleptic sandwich SMMs featuring a larger and heavier variant of the cyclopentadienide, the tris(tert-butyl)cyclopentadienide, as shown in Figure 1.1f.[39] The complex shows a hysteresis opening at 2 K, with a similar axial magnetic anisotropy described for the Cp*ErCOT. In this case, the dihedral angle of the compound amounts to 4.1°, presumably decreasing the admixing of states in the ground state manifold, due to the higher symmetry with respect to the similar Cp*ErCOT. However, only one conformer was reported for this complex, caused by the steric pressure generated by the neighboring complexes in the crystal lattice.

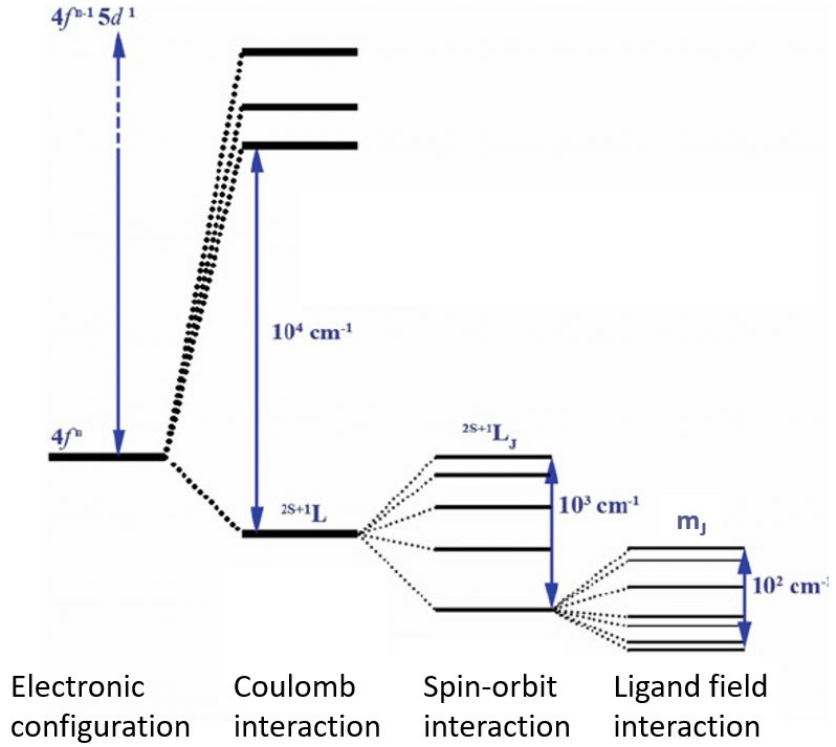

Figure 1.2. Electronic 4f-level diagram of a trivalent lanthanide ion surrounded by a ligand field, as in the case of Er-COT based SMMs. The diagram shows the effect and the magnitude of the induced level splitting, starting from the electronic configuration of the free ion on the left, adding the repulsive electron-electron Coulomb interaction, the spin-orbit splitting and ultimately the effect of the ligand field. Graph adapted from ref. 3.

The advantage of using lanthanides when designing SMMs lies in the fact that the magnetism of these elements is located in the 4f shell, which is electrostatically shielded by the presence of the more external 5s and 5d levels, thus poorly interacting with the environment.[3] Compared to 3d metals, lanthanides show a strong spin-orbit interaction with respect to the crystal or ligand field generated by the surroundings. An electronic level diagram of a lanthanide can be represented by the scheme in Figure 1.2, with the Hamiltonian in the Equation 1.1, where $\hat{\boldsymbol{p}}$ is the momentum operator, *m* the electron mass, *Ze* the nuclear charge, ε_0 the vacuum permittivity, ***r*** the position vector, ξ_i the spin-orbit coefficients, $\hat{l}$ and $\hat{s}$ are the orbital and spin momentum operators, B_q^k the ligand field

coefficients and $C_q^{(k)}$ are spherical tensor operators, all summed over the multi-electronic configuration of the atom, as described in detail in literature.[45]

$$\text{(1.1)} \quad \widehat{H} = \sum_i \left(\frac{\widehat{\boldsymbol{p}_i}^2}{2m} - \frac{Ze^2}{4\pi\varepsilon_0|\boldsymbol{r}_i|}\right) + \sum_{i<j} \frac{e^2}{4\pi\varepsilon_0|\boldsymbol{r}_i - \boldsymbol{r}_j|} + \sum_i \xi_i(r)\hat{l}_i \cdot \hat{s}_i + \sum_{i,k,q} B_q^k \, C_q^{(k)}(i)$$

For the present discussion, the Hamiltonian $\widehat{H}$ in Equation 1.1 can be conveniently summarized in four terms, representing the electronic configuration $\widehat{H}_e$, the electron-electron interaction $\widehat{H}_{ee}$, the spin-orbit interaction $\widehat{H}_{SO}$ and the ligand-field interaction $\widehat{H}_{LF}$, respectively, as reported in Equation 1.2.

$$\text{(1.2)} \quad \widehat{H} = \widehat{H}_e + \widehat{H}_{ee} + \widehat{H}_{SO} + \widehat{H}_{LF}$$

In energy terms, the Coulomb interaction $\widehat{H}_{ee}$ induces an energy splitting of the states on the scale equivalent to few 10^4 cm^{-1} (~10 eV), while the spin-orbit interaction induces a splitting of several thousands of cm^{-1} (~1 eV). However, the splitting induced by the ligand field $\widehat{H}_{LF}$ spans only up to a thousand cm^{-1}(~100 meV), with the levels split only by few hundreds of cm^{-1} (~10 meV).[3]

Since lanthanides usually possess a large unquenched orbital moment, the spin-orbit splitting of the levels is usually denoted by the quantum number of the total angular momentum *J* with the nomenclature $^{2S+1}L_J$, where *S* is the spin quantum number and *L* the term symbolizing the total orbital quantum number. The ligand field generated by the environment surrounding the lanthanide removes the degeneracy on each *J* level, splitting it into a manifold of m_J levels, which go in steps of 1 from +*J* to –*J*.[45] The energy positions of the m_J states of the manifolds are solutions to the Hamiltonian $\widehat{H}_{LF}$, which can be calculated from first principles[46] and/or experimentally determined. Techniques like electron paramagnetic resonance, absorption spectroscopy and luminescence are the main tools to obtain the energy level positions induced by the ligand field.

In case of the Er^{3+}, the ground state can be obtained by the Hund rules and it corresponds to *J* = 15/2 ($^4I_{15/2}$), which due to the spin-orbit interaction is separated from the first excited state $^4I_{13/2}$ by ~6500 cm^{-1}, corresponding to ~1500 nm.[46,47] Formally, the 4f-4f transitions in lanthanides are not allowed by the electric dipole selection rules, but the strong spin-orbit coupling in the $4f^n$ configuration mixes states of different *S* and *L* values, which induces the violation of the selection rules. Moreover, in case of inversion symmetry breaking with respect to the position of the Er ion, induced by the ligand field, the mixing of the states with opposite parity allows these transitions to happen.[48] The intra-4f transitions in Er(III)-based complexes have been experimentally observed and have shown a very narrow character of absorption/emission lines,[49] which sometimes makes them hard to access with resonant absorption techniques without the specific knowledge of the energy level transitions.[50]

The advantage of using the intra-4f transitions of erbium in the near infrared (NIR) range lies also in the possible applications in the communication and sensing technology.[51] This range includes also the typical roto-vibronic bonds of molecular systems, allowing to use the excellent lasing capabilities of Er

for interfacial applications.[52] In addition, coherent transitions between 4f states have been suggested to participate in the optical manipulation of the nuclear spins, acting as a fundamental process in the read-out of systems emulating qubits for quantum computing.[53] Therefore, the Er^{3+} based SMMs have the additional advantage to be potential candidate for optical manipulation of the magnetic states by coherent transitions in the NIR range. However, the optical properties of these complexes are strongly sensitive to the specific ligand field experienced by the metal ion, since it affects the transition rates (cross section), expressed in terms of oscillator strengths (probability of absorption/emission of radiation between energy levels of an atom or molecule), and the energy positions of the *J*–manifold levels. [54,55] The technique of choice to obtain quantitative information about these transitions is infrared spectroscopy, as described in the next Chapter.

An example of an energy level scheme of the $^4I_{15/2}$ ground state manifold of an Er^{3+} ion is reported in Figure 1.3. The diagram shows that in a pure J = 15/2 ground state, the manifold splits in 8 doubly-degenerate states (doublets), states at the same energy but opposite magnetization, typical behavior for a Kramers ion.[56] The doublets are separated by an energy barrier, which depends on the details of the ligand field parameters of $\widehat{H}_{LF}$. In most cases, the strong spin-orbit coupling and the low symmetry of lanthanide-based organometallic complexes induce the mixing of the ground state with higher energy levels, including the 4f-5d mixing, which affects the purity of the doublets. These ligand field states then become an admixture of weighted (and properly normalized) contributions α_{m_J} of states with different m_J values as:

$$|\Psi\rangle_{CF} = \sum_J \sum_{m_J} \alpha_{m_J} \left|\Psi_{J,m_J}\right\rangle \quad (1.3)$$

Er^{3+} sandwich complexes have often shown a large contribution of a specific m_J value for the ground state doublet, often identified with $m_J = \pm 15/2$.[38,39,44,57] The mixing of the states induced by a distortion from the axial symmetry, and thus departing from being centrosymmetric, produces the relaxation of the magnetization of the complexes in a temperature-independent process, called quantum tunneling of magnetization (QTM). At low temperature and zero external magnetic field, the tunneling between the two states with opposite m_J value in the lowest energy doublet is the main relaxation pathway for SMMs. As indicated in Figure 1.3, other relaxation processes can concur to the magnetization relaxation. These processes are phonon-assisted and temperature-dependent.[58] If an external magnetic field H is applied, a direct single-phonon process that involves a transition between the states of a doublet (without crossing the barrier) happen when the phonons are in resonance with the (energy of the) external magnetic field H. The second, called Raman process, involves two phonons interacting with the ground state doublet and inducing the transition via a virtual state. The third, called Orbach process, is a two-phonon resonant process that induces the transition via a higher excited doublet, when the temperature is high enough to overcome the energy barrier of the process.

All the three processes affect the relaxation time τ of a Kramers ion-based SMM as in Equation 1.4 (excluding the non-thermal processes), with A, C and τ_0 constants of the 3 relaxation processes, respectively (*k* is the Boltzmann constant).

$$(1.4) \quad \tau^{-1} = AH^4T + CT^9 + {\tau_0}^{-1}\exp\left(-U_{eff}/kT\right)$$

The effective anisotropy barrier U_{eff} is one of the main parameters determining the SMM behavior of a complex and is connected to the splitting of the ground state manifold.[46] Other than measuring the relaxation times, another way to determine the SMM properties of a complex is by measuring the magnetic hysteresis opening.

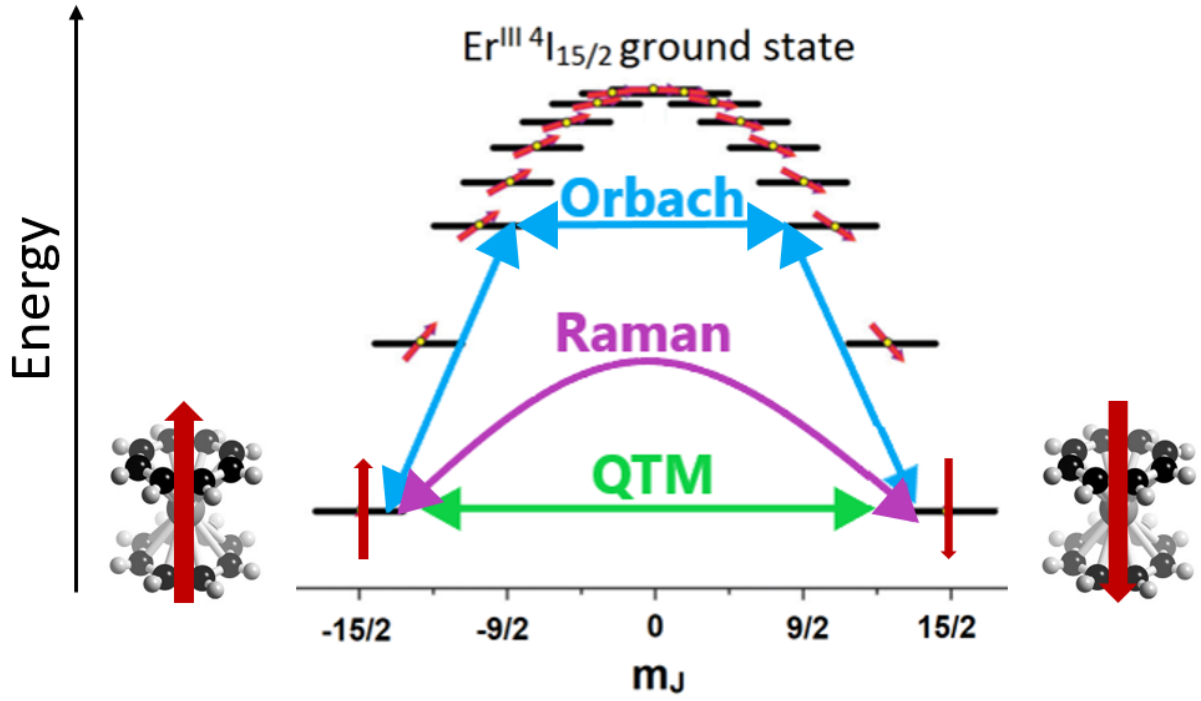

Figure 1.3. Scheme of the ground state multiplet $^4I_{15/2}$ of a typical Er^{3+} SMM, showing the lowest energy doublet m_J = ±15/2 and increasingly higher energy doublets, with associated projections of the magnetization (red arrows). The main relaxation of magnetization processes are sketched, such as the quantum tunnelling of magnetization (QTM), and the double-phonon-assisted Raman and Orbach processes, described in the text.

When an external magnetic field $\vec{H}$ is applied onto a Ln SMM, such as the Er^{3+} organometallic complexes presented previously, the degenerate doublets shown in Figure 1.3 are split in energy. In the case of purely isotropic compound, the complex shows an alignment of the magnetization towards the direction of the magnetic field, with the magnetization following the Brillouin function in Equations 1.5:

$$(1.5) \quad M = Ng_J\mu_B J \cdot B_J(y), \text{ with } B_J(y) = \frac{2J+1}{2J}coth\frac{(2J+1)y}{2J} - \frac{1}{2J}coth\frac{y}{2J} \text{ and } y = \frac{g_J J\mu_B\mu_{0H}}{kT},$$

where *N* is the number of molecules, g_J the Landé factors corresponding to the total magnetic moment *J*, μ_B the Bohr magneton and $\mu_0$the magnetic permeability in vacuum.[46] In case of an

anisotropic system, the factors in equation 1.5 change according to the so-called “easy-” or “hard-“ axis/plane of magnetization, depending on the anisotropic direction of the magnetization.

However, at temperatures below the blocking temperature T_B, the complexes remain magnetized when the external magnetic field is removed, causing the opening of the magnetization curve due to the hysteresis of the magnetization. An ideal representation of the hysteresis opening is shown in Figure 1.4, pointing out the remanance magnetization M_R, the residual magnetization at zero external magnetic field, and the coercitive magnetic field H_C, the magnitude of the applied field necessary to remove the magnetization. However, the relaxation processes discussed previously affect the ideal shape of the magnetization curve. In particular, when the QTM is strong, the magnetization curve tends to close at zero field, showing a typical butterfly-like shape displayed by many SMMs.[46] In case the rate of the sweeping external magnetic field is faster compared to the rate of the relaxation of the magnetization in Equation 1.4, a hysteresis opening is detected. For this reason, the sweeping rate of the magnetic field affects the shape of the magnetic hysteresis curve, as discussed extensively in literature.[46]

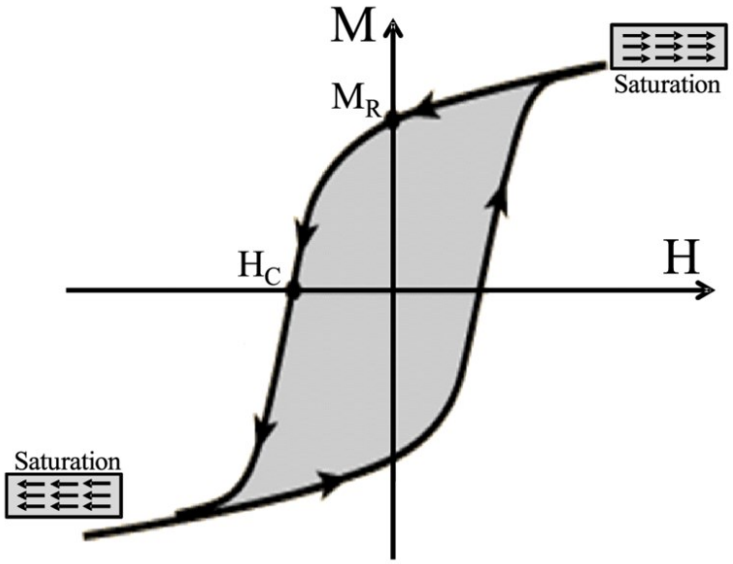

Figure 1.4. Scheme of an ideal magnetization curve *M(H)* displayed by SMMs below the blocking temperature T_B. The remanance magnetization M_R and the coercive magnetic field H_C are shown. Figure adapted from ref. 59.

The relaxation of the magnetization is the main process limiting the SMMs properties of organo-metals and the different relaxation mechanisms are actively studied in novel complexes. However, these relaxation pathways can be enhanced or quenched when depositing those systems on the surface, changing completely their magnetic behavior. Moreover, the details of the ground state manifold due to the different ligand fields of structurally similar sandwich Er SMMs can affect both the optical and magnetic properties of those systems. In order to use of Er^{3+} - based organometallic

sandwiches for technological applications it is important to understand the behavior of those systems when deposited on surfaces, as well as the details of the optical transitions in the NIR spectral range. In the present work, we aim to understand both the magnetic properties and the surface self-assembly of the introduced complexes on the prototypical metal Ag(100) surface, as well as the optical properties in the bulk phase related to the transitions between the ground state and first excited state *J* manifolds of those complexes. To find the answers to both questions in the regime of a single layer of molecules on the surface and bulk crystallites, two sets of samples were prepared and studied with different techniques, which brings the next chapters to be generally split in two parts, addressing the two type of samples and techniques.

After the introduction, the main experimental methods and the equipment used to perform this research are explained in Chapter 2. Starting from a brief introduction of the synchrotron radiation, the main aspects of the linearly and circularly polarized X-ray absorption spectroscopy, the X-ray photoemission spectroscopy and the Fourier-transform infrared spectroscopy, as well as the general idea behind the scanning-tunneling microscopy are discussed. The last part introduces the experimental setup used, with a brief explanation of the working principles of the three beamlines used at the Swiss Light Source synchrotron at Paul Scherrer Institut (PSI, Switzerland), namely the X-Treme, PEARL and IR beamlines.

Chapter 3 elucidates the preparation of the samples and their characterization, with a focus on the integrity of the compounds, given their extreme air-sensitivity. The first section explains the sublimation and deposition of Cp*ErCOT and the $K[Er(COT)_2]$ onto the Ag(100), with a focus on the latter compound, since the thermal treatment of the $[K(18\text{-c-}6)][Er(COT)_2]\cdot 2THF$ precursor affects the presence of the solvent molecules. The second section shows the preparation of pellet samples used for infrared spectroscopy and their characterization for structural integrity of the four Er^{3+}-based complexes introduced in this Chapter.

Chapter 4 presents the main experimental results and the discussion of the data, separated in two sections. The first is dedicated to the structural and magnetic properties of Cp*ErCOT and the $K[Er(COT)_2]$ complexes deposited on Ag(100), showing the main differences that the two compounds display. The second section illustrates the temperature-dependent infrared absorption spectra of $[K(18\text{-c-}6)][Er(COT)_2]\cdot 2THF$, $[Li(DME)_3][Er(COT'')_2]$, Cp*ErCOT and $Cp^{ttt}ErCOT$ complexes relative to the transitions between the Er^{3+} ground state ($^4I_{15/2}$) and the first excited state ($^4I_{13/2}$) manifolds, connected to the energy level scheme of these compounds.

The thesis is concluded by a summary of the main results of the studied systems relative to the scientific questions set in this chapter, as well as further perspectives for future investigations of these and similar complexes.

Chapter 2
Methods and experimental details

This Chapter presents the methods used, starting with an overview of the basics of synchrotron radiation, the main synchrotron related techniques for surface science studies and techniques used to study complexes in bulk crystallites. This part also includes a section about the details of the multiX simulations used to compare with the experimental spectra of the polarization-dependent X-ray absorption. The second part introduces the experimental details/setups and in particular the beamlines used at the Swiss Light Source, Paul Scherrer Institut, focusing on the relevant parameters.

2.1 Methods

2.1.1 Synchrotron radiation

Synchrotron radiation is an electromagnetic radiation produced when electrons at relativistic speeds are compelled to follow curved trajectories by external magnetic fields. The advantage of the synchrotron radiation is that of being highly spatially collimated, have high brilliance (high flux per unit area) and a broad spectral range, properties which require special conditions for the acceleration of the electrons and special machines to control the electron beams. For this purpose, facilities called synchrotrons are used, which consist of particle accelerators shaped in a circle with diameters from few tens to hundreds of meters. Such machines use highly energetic electromagnetic fields to accelerate electrons along a specific path, and keep them into closed loops, corresponding to the so-called storage ring. In the storage ring, the electrons are bound to travel in the loop with the use of special bending magnets while the speed of the electrons is kept constant with the use of resonating-frequency cavities, which help to bunch electrons in small packets.

The synchrotron radiation is produced by bending magnets and special insertion devices, such as wigglers and undulators, and is usually linearly or circularly polarized (see below). While the light emitted by a bending magnet can be considered as a ”pulse” in the time frame (Figure 2.1), the photon energy bandwidth *Δhν* is proportional to the magnetic field *B* of the magnet, as:

$$\Delta h\nu = h\gamma^2 eB/(\pi m_e), \quad (2.1)$$

with hν the photon energy, *γ* the relativistic constant, *e* and m_e the electron charge and mass.[59] This corresponds to a broad bandwidth, which depends on the details of the magnet and the speed of the electrons, but it usually ranges from infrared (~meV) to hard X-rays (~keV).

On the other side, undulators are machines composed by parallel arrays of N magnets with opposite polarity and the electrons travel between the arrays in an oscillating pathway, producing a signal detected on a broader timescale (Figure 2.1). The constructive interference generated by the emitted radiation at every curvature of the electrons on a period λ_u results in a narrow bandwidth energy peak with central energy $h\nu_c$ (Equation 2.2), together with *n* higher energy harmonics (*n* is an integer number, multiplying Equation 2.2).

$$(2.2)\ h\nu_c \approx 2\gamma^2(\mathrm{hc}/\lambda_u)/(1 + K^2/2),$$

with *c* the speed of light in vacuum, *K* being the so-called undulator parameter and depending on the strength of the magnetic field B_0 and the period of the array of magnets λ_u, as in Equation 2.3:

$$(2.3)\ K = eB_0\lambda_u/(2\pi c m_e)$$

For undulators the value of K is usually below 1, while for higher values the oscillation amplitude of the electron becomes larger and the emitted spectrum becomes a sum of independent "pulses", generating a broadband spectrum. This behavior is typical for devices called wigglers (Figure 2.1).[59]

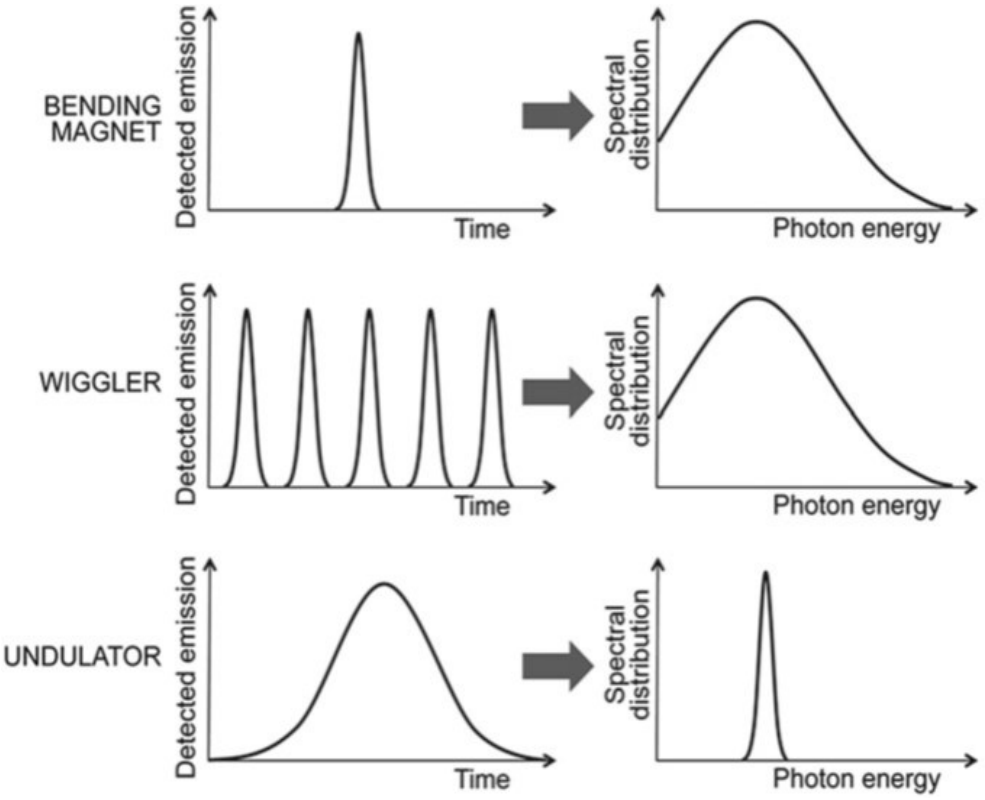

Figure 2.1. Time structure and its emission spectrum counterpart for different types of sources. Top: short pulse and broad emission band from a bending magnet. Middle: series of short pulses from a wiggler, again corresponding to a broad emission band. Bottom: longer pulse from an undulator and narrower bandwidth. Image taken from ref. 60.

A scheme of a typical storage ring is shown in Figure 2.2. The generated radiation is guided through straight sections after the bending magnets/insertion devices, called beamlines. In these sections, optical devices focus and produce monochromatic photon beam to deliver to the end-station, which is a group of machines that use the synchrotron radiation for scientific investigation. The end-stations are usually designed to use one (or few) technique(s) and are used to study scientific cases in fields like physics, chemistry, material science, biology and geology.

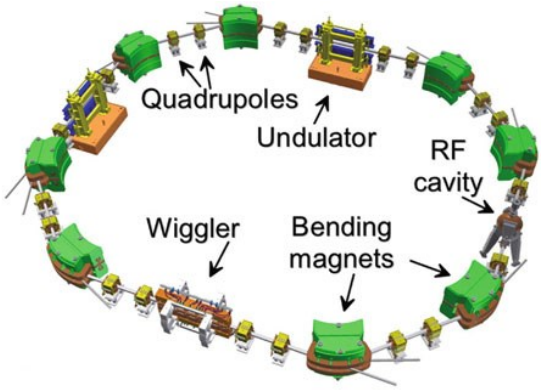

Figure 2.2. Schematic view of a storage ring where bending magnets, focusing and de-focusing magnets (quadrupoles), insertion devices (undulators, wigglers) and the RF (radio frequency) cavity are presented; the injection system is omitted for clarity. Image taken from ref. 60.

2.1.2 X-ray absorption spectroscopy

In semi-classical terms, when an electromagnetic wave is transmitted through matter, the intensity of the wave is attenuated exponentially with the travelled distance z.[45,59] This process is called absorption and the intensity of the electromagnetic wave follows the Beer-Lambert law:

$$(2.4)\ I_z = I_0 e^{-\mu z},$$

where I_0 and I_Z are the incident and the attenuated intensities of the incoming wave, μ the absorption coefficient and z the travelled distance/depth. The absorption coefficient μ is element specific and is proportional to the absorption cross section σ^{abs} of the atoms constituting the sampled specimen. The material-dependent absorption cross section itself is a function of the energy of transmitted radiation and it can assume a complicate behavior in different energy ranges. In the range of X-rays, which are highly energetic electromagnetic waves spanning between 100 eV and 100 keV, the cross section is a decaying function with increasing energy of the light. The importance of X-rays in the study of materials lies in the fact that these electromagnetic waves have the same energy range as the bound core electrons constituting the atoms. The absorption cross section σ^{abs} is a quantity representing the probability of interaction between an atom and a photon of a certain energy $h\nu$ (h = Planck's constant,

v frequency). In particular, when the energy of the photon coincides with the energy difference of a bound electron (in an atom) between it's ground state and an empty state, the maximum probability of interaction occurs. The electron transitions from the unperturbed initial (core) level $|i\rangle$ of energy E_i to a final excited (unoccupied) state $|f\rangle$ of energy E_f, following the Fermi golden rule:

$$(2.5)\ T_{if} \propto\ |\langle f|H_{int}|i\rangle|^2 \rho(E_f)\delta(E_f - E_i - h\nu)$$

where T_{if} is the transition probability per unit time (in the first-order approximation), $\rho(E_f)$ is the density of unoccupied final states, δ_{if} the Kronecker delta for the energy conservation and H_{int} is the time-dependent perturbation generated by the interacting photons. In this contest, the transition probability is given by the total absorption cross section times the incident photon flux. Ignoring the time-dependent evolution of the perturbation and under the electric dipole approximation, the perturbation can be simplified as $\widehat{H}_{int} \propto\ \widehat{\boldsymbol{p}} \cdot \hat{\boldsymbol{\epsilon}}$, where $\widehat{\boldsymbol{p}}$ is the electron dipole operator and $\hat{\boldsymbol{\epsilon}}$ is the electric polarization operator of the photons. The electron dipole operator is proportional to the operator $\hat{r}$, symbolizing the position (amplitude) that the bound electron can assume within the electron probability density of the electron orbital. Therefore, the transition probability depends on the polarization vector $\vec{\epsilon}$ direction compared to the distribution of the probability density of the electron orbital.

When a resonant absorption happens, the absorption energy spectrum displays a characteristic element-specific "jump", commonly referred to as absorption edge (or "white line"). According to the IUPAC notation, these electronic transitions are labelled with a letter and number representing the initial state from which the electronic transition happens. For example, the M_4-edge represents the transition from the $3d_{3/2}$ orbital (in atomic notation), while the M_5-edge represents the transition from $3d_{5/2}$ orbital. Every element has absorption edges at different energies, depending on the atomic number and the oxidation state of the absorbing atom.[59]

When an excitation happens with an electron transition to the continuum above the vacuum level, the event is called non-resonant absorption and a photoelectron is created (see also Section 2.1.6). In both the resonant and non-resonant excitations, the electron leaves a core hole, which is filled by an electron through a de-excitation process that can generate an emission of a photon (fluorescence) or electrons (Auger). The most intense electron transitions of the absorption edges follow dipole selection rules, according to which the orbital angular momentum ℓ between the initial and the final state can change by ±1, while the spin has to be conserved.

The X-ray absorption spectroscopy (XAS) is a technique that studies the local geometric and electronic structures of a sampled material, by measuring the so-called X-ray absorption fine structure (XAFS). The detailed structure from few eV lower and up to the resonant edge of a sampled material constitute the pre-edge/edge position region, giving information about the empty valence states, the oxidation

state, the effects of the coordination environment on the absorbing atom, as well as information on transitions to bound localized states (example in Figure 2.3a). This region can also provide information on the magnetic properties of the sampled material, as discussed further below. The structure within ~50 eV above the edge is called X-ray absorption near-edge structure (XANES), also sometimes referred to as near-edge absorption fine structure (NEXAFS), and it gives information about local electronic and geometric structure of the sample. The fine structure in the extended region above the edge, which can span up to ~1 keV above the edge, is called the extended X-ray absorption fine structure (EXAFS), and it gives information on the local environment of the absorber that (back)scatter photo-emitted electrons transitioning to the continuum (non-bound states).

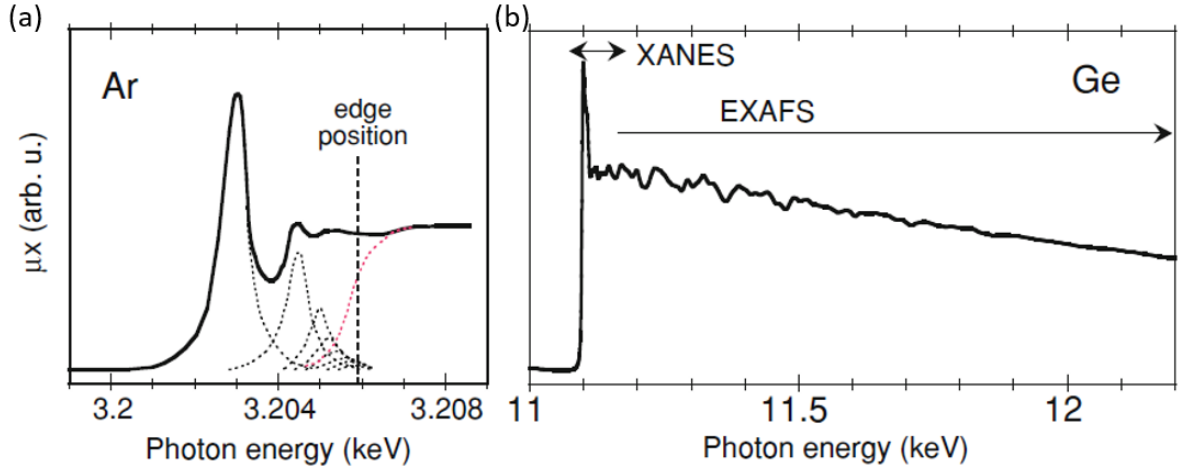

Figure 2.3. X-ray absorption fine structure at the K-edge of (a) Ar and (b) Ge. The edge position, the XANES and EXAFS regions are indicated. Image taken from ref. 60.

In the present work, we will focus on the study of the fine structure of the energy region adjacent to the edge position, and the spectra will be referred with the general term "X-ray absorption spectra" (XAS) for simplicity. The information on the local structural and magnetic properties of the studied samples will be extracted from polarization-dependent XAS. With this regard, the polarization of light is defined as the geometrical direction of oscillation of the electric field with respect to its propagation direction. In particular, for linearly polarized waves the oscillation is orthogonal to the propagation vector. For circularly polarized light the oscillation rotates clockwise or anticlockwise with respect to the propagation vector $\vec{k}$, having respectively a negative (*C-*) or a positive (*C+*) polarization, with the electric field $\vec{E}$ evolving according to Equation 2.6 (the propagation is assumed along the *z* direction, without losing its generality).

$$(2.6)\ \vec{E}_{C\pm} = \mp {E_0}/{\sqrt{2}}\,(\hat{\epsilon}_x \pm i\hat{\epsilon}_y)e^{i(kz-\omega t)+i\varphi},$$

with ω the angular frequency, E_0 the magnitude of the electric field, φ an arbitrary phase and *t* time.[45]

The polarization vectors in a circularly polarized wave are always orthogonal, with the relation 2.7:

$$(2.7)\ \hat{\epsilon}_x \pm i\hat{\epsilon}_y = \hat{\epsilon}_x + e^{\pm i\pi/2}\hat{\epsilon}_y$$

The concept of polarization is also illustrated in Figure 2.4.

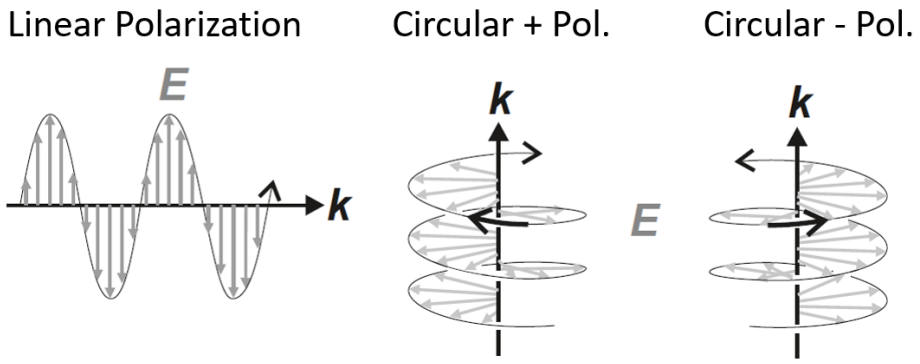

Figure 2.4. Illustration of linearly and circularly polarized light, showing the motion of the polarization vector **E** with respect to the propagation direction **k**. Image adapted from ref. 45.

While for a given photon frequency *v* linearly and circularly polarized photons carry the same amount of energy $E_0 = h\nu$, only the circular polarized ones have a spin angular momentum (+*h* for C+, -*h* for C-), which can be transferred to the absorbing electron. When probing different atomic orbitals of a sample material, the polarization of the photon beam becomes the main tool to detect the natural and the magnetic dichroism, as explained in the next section.

2.1.3 X-ray linear and circular dichroism

As introduced in the previous section, the absorption at a given edge is proportional to the projection of the photon polarization with respect to the symmetry of the empty orbitals (holes) probed by the excitation process. In particular, linearly polarized X-rays are strongly sensitive to the anisotropy of empty valence orbitals of the sample and can detect the dichroism of a material due to a change of the charge distribution of the local environment. The measured intensity of the absorption edge is directly proportional to the number of holes in the projected direction of the photon polarization. By using two different orientation of the photon polarization (usually shifted by 90°) and by rotating the sample compared to the incoming photon beam, different polarization-dependent spectra are obtained. The difference between the two absorption spectra gives the X-ray linear dichroism (XLD) for a specific sample orientation. An example is shown in Figure 2.5 for the Er $M_{4,5}$-edge where the photon beam of wavevector $\vec{k}$ impinges the sample at an angle θ with two distinct polarizations,

labelled as linear vertical (LV) and linear horizontal (LH) polarization. This results in two different absorption spectra and the difference of the absorptions μ(LV) – μ(LH) is called XLD.

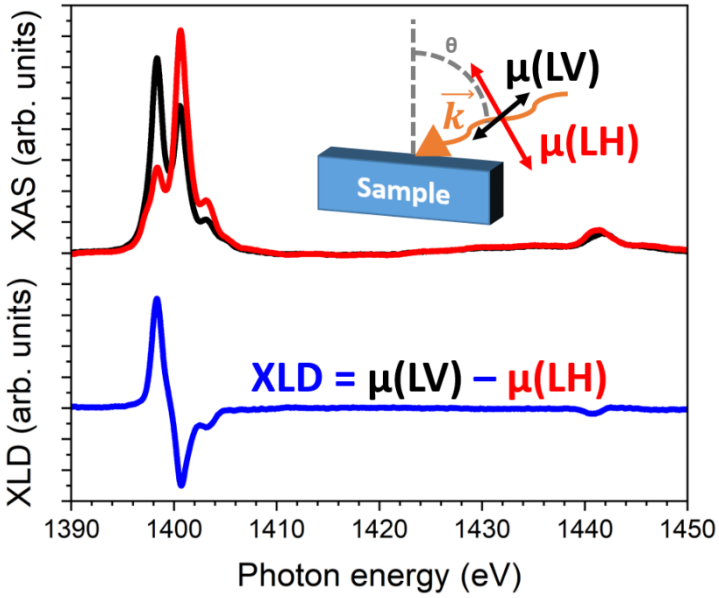

Figure 2.5. Example of linearly polarized XAS and XLD spectra of the Er $M_{4,5}$-edge, together with a sketch of the incident wavevector $\vec{k}$ of photons impinging the sample at an angle θ with two orthogonal polarizations, linear horizontal (LH) and linear vertical (LV).

When the difference in the absorption spectra is caused by an intrinsic low symmetry of the system or the breaking of the symmetry at a surface/interface or due to the strain, the effect is properly called X-ray natural linear dichroism (XNLD). As opposed to that, when the atomic charge is distorted by an axial alignment of spins from the spin-orbit interaction, the dichroism generated has a magnetic origin, so the measured effect is called X-ray magnetic linear dichroism (XMLD). For the scope of the present work, the complex symmetry of the 4f orbital shells of lanthanides in single-molecule magnets makes it hard to disentangle the natural from the magnetic contribution, making the XLD a useful tool in connection with the simulations of the Ln $M_{4,5}$ edge (see also section 2.1.5).

A large advantage of the organometallic complexes is their strong magnetic anisotropy, which can be measured by X-ray magnetic circular dichroism (XMCD) technique. The XMCD spectrum can be obtained as the difference between the absorption spectra with circular polarization vector parallel and antiparallel to an external magnetic field applied onto the sample material. The XMCD signal is proportional to the projection of the magnetization *M* of the sample onto the beam direction, such that (here θ is the angle between the beam incidence and the magnetic moment of the sample):

$$(2.8)\ XMCD = \mu(C-) - \mu(C+) \propto Mcos(\theta)$$

When circularly polarized photons interact with core electrons, they excite preferentially spin up/down electrons, according to the transferred spin angular momentum and the orientation of the

orbital moment. The excited electrons fill unoccupied valence states and, in case there is an imbalance between empty spin up/down states, an XMCD spectrum is obtained.[60]

The XAS and XMCD spectra can be used to determine information about the orbital and spin components as well as the magnetic moment of the sample, as explained in the next Section.

2.1.4 Spin and orbital sum rules

The XMCD sum rules relate the integrated XMCD spectra to the ground state expectation values of the orbital and spin moments of the studied sample.[61,62] Focusing on the orbital sum rules for the $M_{4,5}$-edge, particularly useful to measure the magnetism of 4f elements, the expectation value of the orbital angular moment $\langle L_Z \rangle$ of a sample is proportional to the total integral of the XMCD spectrum over M_4 and M_5 edges times the number of holes n_h in the 4f shell, normalized to the total integral of the polarization-independent X-ray absorption over the same edges:

$$\langle L_Z \rangle = \frac{-3n_h \int_{M_{4,5}} (\mu^+(E) - \mu^-(E)) \cdot dE}{\int_{M_{4,5}} (\mu^+(E) + \mu^-(E) + \mu^0(E)) \cdot dE} \quad (2.9)$$

The denominator of the Equation 2.9 is the sum of the absorption of two circular polarizations ($\mu^+ + \mu^-$) and the polarization μ^0 in the transversal direction, which for practical applications is assumed as the average of the two circular polarizations.

In a similar way, the spin $\langle S_Z \rangle$ of the studied system can also be extracted from XMCD spectra, considering that it can be obtained from the effective spin $\langle S_Z \rangle^{eff}$ of the system, defined as follows:

$$\langle S_Z \rangle^{eff} = \frac{2}{3}\langle S_Z \rangle + 2\langle T_Z \rangle = -n_h \frac{\int_{M_5} \left(\mu^+(E) - \mu^-(E)\right) \cdot dE - {}^3/_2 \int_{M_4} \left(\mu^+(E) - \mu^-(E)\right) \cdot dE}{\int_{M_{4,5}} \left(\mu^+(E) + \mu^-(E) + \mu^0(E)\right) \cdot dE} \quad (2.10)$$

where $\langle T_Z \rangle$ is the expectation value of the magnetic dipole moment, which takes into account an anisotropic distribution of the spin.[63] The value of the magnetic dipole moment was extensively studied and for the rare earths it can also be evaluated analytically since it is proportional to $\langle S_Z \rangle$.[62,64] The numerator of Equation 2.10 corresponds to the difference of the area integrals of the M_5 and M_4 edges, respectively, multiplied by numerical factors. The agreement of the quantum numbers extracted from the sum rule analysis with the ones calculated from first principles is generally good, although in some cases the uncertainty can be quite high.[65] In the case of samples deposited on surface in the monolayer or sub-monolayer range in particular, the uncertainty can be large due to low signal-to-noise ratio of the spectra or difficulty in the removal of non-linear background signal, as explained in the data analysis section. The total magnetic moment of an atom can be obtained as $m_B = \mu_B(\langle L_Z \rangle + 2\langle S_Z \rangle)$, with μ_B the Bohr magneton and $\langle L_Z \rangle$ and $\langle S_Z \rangle$ expressed in Planck's constant $\hbar$ units.

2.1.5 XAS simulations

The performed XAS, XLD and XMCD measurements are complemented by simulations based on a point-charge model implemented by multiX.[66] The method uses the information about core and valence electronic shells and is based on first-principle approach for the calculation of the matrix elements of the electron-electron and spin-orbit interactions, as well as single-electron orbitals, relying on only few semi-empirical parameters. In particular, the electronic states are generated by parametrizing the ligand field with an effective electrostatic field coming from point charges surrounding the absorbing atom. The advantage of the point-charge model is the possibility to enter the position of the ions constituting the ligand environment without implementing symmetry relations, which leads to sufficiently accurate XAS/XMCD/XLD spectra with only few "fitting" parameters.[66] In most cases, the method have shown to model all possible splitting of the localized valence states with the presence of one or few coordination shells represented by point charges, without taking into account effects such as hybridization.[67–69] Moreover, the method allows simulating any experimental geometry by a simple parametrization of the system and the interacting external magnetic field. The resulting spectra take in account the polarization and the direction of the impinging photon beam. Further details can be found in the original paper.[66]

By simulating Cp*ErCOT and K[Er(COT)$_2$] complexes, the delocalized electron cloud of the π orbitals of the ligand rings and the almost parallel planes of the ligands act on the Er ion with a symmetry of the effective charge that can be modelled as $C_{\infty v}$.[38] Due to the point-charge nature of the method, however, for both complexes the used model relies on a structure with an imposed D_{8h} symmetry given by the position of the carbons of the first coordination shell surrounding the central Er ion, with the Er-C distance taken from literature.[32,33] The choice is justified by the similarity in the structure of the delocalized π orbitals and the low sensitivity of the 4f orbitals to small changes of the external ligand field. The strongest change in the XAS spectra was identified by the orientation of the main rotational axis of the complexes (coinciding with the anisotropic orientation of the magnetic moment of the complexes) with respect to the polarization of the incoming photon beam. To keep the model simple and the number of parameters low, the charge of the carbon atoms was manually varied, as well as the fraction of complexes oriented with the molecular axis in-plane or out-of-plane, compared to the substrate plane. Such an elegant, simplified model system is useful to understand the main features of the XAS, XLD and XMCD spectra and their dependence on the X-ray incidence angle and the applied magnetic field.

The simulated spectra of the Er $M_{4,5}$-edge shown in Chapter 4 are based on a linear combination of three configurations of the complexes on the surface: the "standing-up" configuration, with the axis

normal to the surface plane (with parameters reported in Table 2.1), and two lying-down configurations, with the axis rotated by 90° around the x- and y-axis, respectively. The method was initially used to simulate the Er $M_{4,5}$-edges of a simple case of a standing-up complex, to study the effect of the orientation of the molecular axis with respect to the polarization vector of the incoming X-rays, and to prove the validity of the simulated ligand field according to the anisotropy of the complexes. Linearly polarized X-rays impinging on the model complex with LV polarization parallel to the rotational axis of the complex and LH polarization parallel to the plane of the ligands shows a simulated absorption spectrum as reported in Figure 2.6a. The LV polarization give rise to a single absorption peak around 1398 eV, identified in the Figure and through the whole text as *, while the LH polarization shows an intense absorption peak at around 1401 eV, identified as °, with almost negligible intensity at the energy around 1398 eV. Since the experiments were performed in the grazing incidence of the beam at an angle of 60° with respect to the normal of the surface of the samples, the method was used in this configuration, leading to the spectra in Figure 2.6b. While the LV polarization is again parallel to the plane containing the ligand rings, the LH polarization shows contributions of both * and ° peaks, due to the projections of the polarization vector on the orbitals of the system. Similar simulations were repeated for different orientations of the complex with respect to the incident photon beam, as explained previously. In case of the circularly polarized spectra, the same procedure is used, presented in Chapter 4. The magnetic field is always assumed parallel to the beam direction and varied between 50 mT for the linearly polarized XAS and 6.8T for the circularly polarized spectra. A sample of the multiX input file is reported in Appendix A, referred to the model shown in Figure 2.6b.

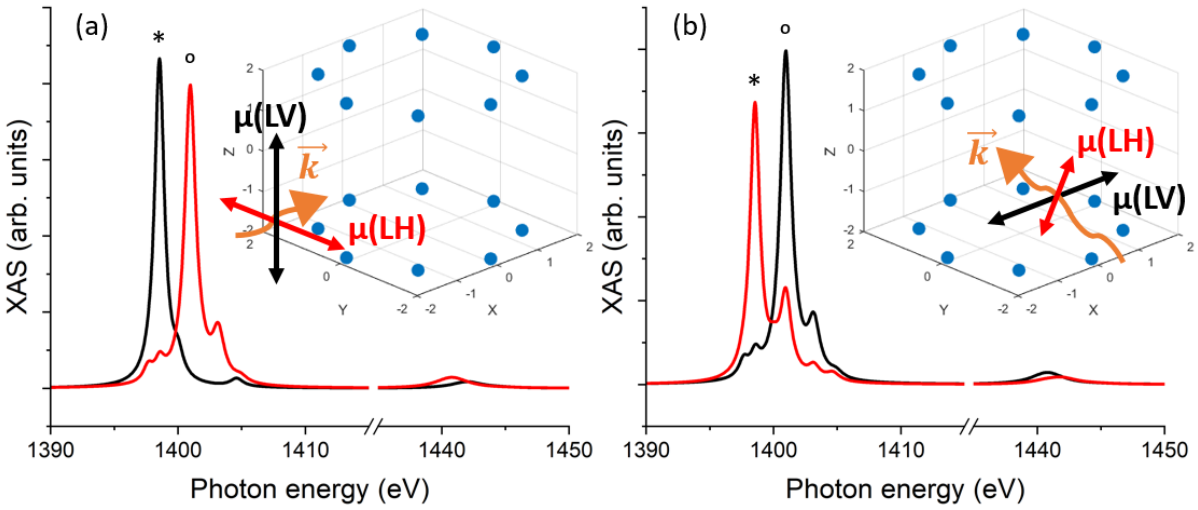

Figure 2.6. Simulated linearly polarized XAS at the Er $M_{4,5}$-edge using multiX, with the model complex in the "standing-up" configuration (insets, with blue representing the position of charges). The spectra change intensity of * and ° peaks according to the orientation of the linear polarization $\vec{k}$ with respect to the axis of the complex, along the z direction, (a) perpendicular and (b) at 60°. The orientation of the polarization follows the description in the text.

Table 2.1. Atomic positions and point charges used to generate the ligand field of a standing-up generic molecule in the D_{8h} symmetry implemented in the multiX code. The positions were extracted from ref. 32.

Atom	x (Å)	y (Å)	z (Å)	q (e)
C	0	1.831	1.912	0.25
C	1.2947	1.2947	1.912	0.25
C	1.831	0	1.912	0.25
C	1.2947	-1.2947	1.912	0.25
C	0	-1.831	1.912	0.25
C	-1.2947	-1.2947	1.912	0.25
C	-1.831	0	1.912	0.25
C	-1.2947	1.2947	1.912	0.25
C	0	1.831	-1.912	0.25
C	1.2947	1.2947	-1.912	0.25
C	1.831	0	-1.912	0.25
C	1.2947	-1.2947	-1.912	0.25
C	0	-1.831	-1.912	0.25
C	-1.2947	-1.2947	-1.912	0.25
C	-1.831	0	-1.912	0.25
C	-1.2947	1.2947	-1.912	0.25

2.1.6 X-ray photoemission spectroscopy

X-ray photoemission spectroscopy (XPS) is a technique that investigates the occupied electronic states, gives information about the dielectric and chemical states, as well as the local structure and the magnetic properties of the sample.[59] The study is performed by analyzing the kinetic energy E_K of photoemitted electrons from a sample absorbing monochromatic X-ray light (with energy $h\nu$) and relating it to the binding energy E_B, representing the energy of the bound electrons compared to the (pseudo)Fermi level, by using the Einstein relation 2.11:

$$E_B = h\nu - E_K - \Phi, \quad (2.11)$$

with Φ the work function of the detector. The binding energy of the core levels is an elemental fingerprint that identifies the chemical species composing the sample. The chemical environment is probed by "shifts" of the core-electron level position due to a change of the local electron density (for example valence state, coordination environment, surface-induced effects, etc.). In addition, the core levels of p, d and f orbitals are spin-orbit split in distinct peaks, whose area ratio is bound by the transition selection rules. In particular, the area ratio between peaks of $p_{1/2}$ and $p_{3/2}$ core levels is 1/2, the ratio between $d_{3/2}$ and $d_{5/2}$ peaks is 2/3, while between $f_{5/2}$ and $f_{7/2}$ peaks is 3/4. In most

photoemission spectra, there are also peaks whose position depends on the incoming photon energy, which are caused by Auger electrons coming from the core-hole de-excitation. The spectra typically show increasingly more intense background with increasing binding energy, which is given by the detection of inelastically scattered secondary electrons in the sample.[59]

The intensity *I(hν)* of the core level XPS peaks is given by the photon flux J_0 at monochromatic photon energy *hν,* the photoionization cross section *σ(hν)*, the angular distribution coefficient $L(\theta)$ which depends on the probing geometry, the number of absorbing atoms *N* in the probed volume and the energy-dependent transmission function of the detector $T(E_K)$, as in Equation 2.12:

$$(2.12)\quad I(h\nu) = J_0\sigma(h\nu)L(\theta)NT(E_K)$$

Under the one-electron dipole approximation explained previously, when a linear polarization of the synchrotron light is used, the asymmetric photoemission of p, d and f orbitals has to be taken into account, which is done by calculating the differential cross section measured in the solid angle acceptance Ω of the experimental setup:

$$(2.13)\ \frac{d\sigma(h\nu)}{d\Omega} = \frac{\sigma(h\nu)}{4\pi}[1 + \beta(h\nu)P_2(\cos\ \alpha)]$$

with $\sigma(h\nu)$ the shell-specific cross section, $\beta(h\nu)$ the energy specific asymmetry parameter and $P_2(\cos\ \alpha) = \frac{1}{2}(3cos^2\alpha - 1)$, with α the angle between the X-ray polarization vector $\vec{\boldsymbol{\varepsilon}}$ (perpendicular to the photons propagation vector in linear polarization) and the direction of outgoing photoemitted electrons (Figure 2.7). The asymmetry parameters $\beta(h\nu)$ can be found tabulated[70] while the angle α is usually imposed by the experimental geometry. By using Equations 2.12 and 2.13 it is possible to quantify the number of absorbing atoms, although it is more common to find the ratios of atoms of different elements in the sample, thus giving the stoichiometry.

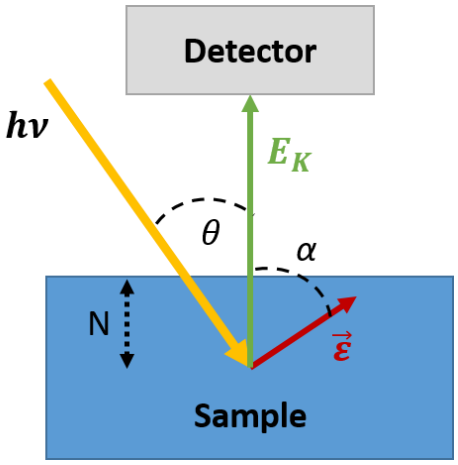

Figure 2.7. Scheme of a generic experimental XPS setup, with the monochromatic photon beam of energy $h\nu$ and linear polarization vector $\vec{\boldsymbol{\varepsilon}}$ probing the volume of the sample containing *N* atoms, and inducing the photoemission of electrons of energy E_K at an angle θ with respect to the incoming beam. Note that $\alpha = 90° - \theta$.

When depositing an adsorbate on a substrate, the coverage/thickness of the adlayer can be estimated by the reduction of the intensity of the absorbance of core level peaks of the substrate compared to the "clean" surface, which follows the Lambert-Beer law (Equation 2.4). Assuming a constant photon flux and same experimental conditions, the coverage thickness *d* can be obtained[59] from the ratio of the absorbance peak intensities I_{ad} and I_0 (peak integral) of the adlayer and substrate, respectively, by taking the tabulated values of the material-dependent mean free path $\Lambda(E_K)$ and the different cross sections of the substrate (σ_0) and the adlayer (σ_{ad}), as in the Equation 2.14:

$$(2.14)\ d = \frac{I_{ad}}{\sigma_{ad}} \frac{\sigma_0}{I_0} \Lambda(E_K)$$

(Note: the absorbance is defined as the natural logarithm of the absorption intensity, as in eq. 2.16).

2.1.7 Fourier-transform infrared spectroscopy

The absorption spectroscopy described in Section 2.1.2 can also be performed in the energy range below that of the visible light, which is called infrared spectral region (IR). This range is important in the study of material sciences because it corresponds to the range of the roto-vibrational modes of molecules, so that the chemical environment can be characterized by measuring the specific photon energies absorbed by the sample. Among the several ways to perform spectroscopy in this energy range, the Fourier-transform infrared (FTIR) spectroscopy[71] uses a combination of partially and fully reflecting moving mirrors to modulate the different frequencies of the incoming light and send them onto a sample material. The modulation is performed by constructive/destructive interference generated by the different optical path produced by a moving mirror of the instrument, called Michelson interferometer. Two different branches of the interferometer create a different pathway λ for the light of frequency ν_0, which creates an interference when the light is recombined again in a single beam, caused by the retardation of one of the two branches. The recorded intensity of the recombined beam is shown in Equation 2.15:

$$(2.15)\ I(\lambda) = \frac{1}{2} I(\nu_0)(1 + \cos(2\pi n\lambda\nu_0)),$$

with $I(\nu_0)$ the intensity of the light at the source and $n\lambda$ an integer multiple of the pathway difference λ created by the mirror.[71] If the incoming light has a broad bandwidth, different frequencies satisfy the constructive/destructive interference for different positions z of the mirror, with $z = n\lambda/2$. As the position of the mirror changes, the modulation of the intensity in Equation 2.15 for each frequency *ν* creates an interferogram, a graph of the reflected or transmitted light through the sample as shown in Figure 2.8a. The shape of the oscillations and the beatings are given by selective absorption of the

different frequencies of the recombined light in the interferometer by the studied sample, convoluted with the oscillating behavior of Equation 2.15.

At this point, computer processing is used to perform the Fourier-transform of the interferogram in the domain of the mirror position to obtain a spectrum in the domain of the photon wavenumber of the incoming light, which is proportional to the photon energy. An example of a transmission FTIR spectrum is reported in Figure 2.8b, showing absorption lines in the near infrared range (~6000 cm^{-1} or ~1500 nm). The advantage of the FTIR spectroscopy over the dispersive/monochromatic spectroscopy is the possibility to acquire a broad energy spectrum at once. The longer the optical path achieved by the motion of the mirrors, the higher the spectral resolution that can be obtained by the interferogram. A more detailed discussion of the interferograms and their Fourier-transforms can be found in literature.[71]

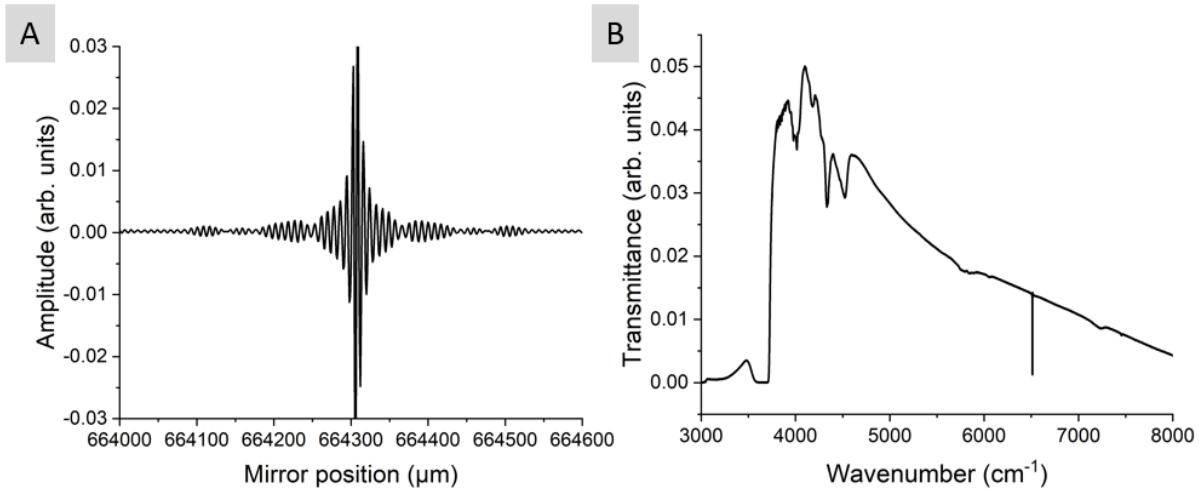

Figure 2.8. Example of (A) a fraction of an interferogram as a function of the mirror position (with respect to the local reference system) obtained by the interferometer at the IR beamline at SLS and (B) its Fourier-transform transmission spectrum as a function of the photon wavenumber in the near infrared range. The data refers to transmission measurements at 3 K of [K(18-c-6)][Er(COT)$_2$]·2THF dispersed in a matrix of KBr, presented in the following Chapters.

When the measurements are performed in transmission, the transmission signal $I_T(\nu)$ can be used to obtain photon frequency-dependent absorbance *A(ν)* as in Equation 2.16, with the transmission normalized to the incident signal $I_I(\nu)$, that eliminates all the "background" signal coming from the optical components of the interferometer:

$$(2.16)\ A(\nu) = -\ln\left(I_T(\nu) \Big/ I_I(\nu)\right)$$

The absorbance is proportional to the absorption coefficient μ introduced by Equation 2.4 through the thickness of the probed sample *d*, with $A(\nu) = \mu d$. As anticipated, the absorbance of a sample in the IR region can be used to identify the nature of the sample according to the bond-specific resonances of the chemical bonds of the sample and the roto-vibrational modes.

It is possible to calculate the absorption cross sections for the electron transitions by using the relation of Equation 2.17:

$$(2.17)\ \sigma_i = {}^{A(\nu)}/_{C_i d} = {}^{-1}/_{C_i d} \log\left({}^{I_T(\nu)}/_{I_I(\nu)}\right),$$

with $C_i = {}^{m_i}/_{V}$ the density of the sample, $V = Ad$ volume (A is the area) and m_i the mass fraction of the i-th specie. By using the molar mass of the different species, the cross section σ_i can be extracted. This information can be used to estimate the oscillator strength of the transitions/transition probabilities per unit time, as introduced in Section 2.1.2.

2.1.8 Scanning-tunneling microscopy

The scanning-tunneling microscopy is a technique that samples the topography of a sample on the nanometer scale.[72] The working principle is based on imaging the local density of states of a biased sample by measuring the tunneling current through a sharp metal tip in proximity (fraction of a nanometer) of the sampled surface. When the tip is very close to the surface without direct contact, the electron wavefunctions of the two materials overlap, giving rise to a finite tunneling current upon the application of a bias voltage between the two. The current $I(z)$ measured by the metal tip depends exponentially on the distance z to the surface and can happen only in the presence of empty electronic states in the hosting material, tip or surface, depending on the polarity of the current. According to the Bardeen model, with the electron density of states expressed by ρ_S (S = surface) and ρ_T (T = tip), the tunneling current is proportional to the applied voltage *V* as in Equation 2.17:

$$(2.17)\ I(z) = 2\pi^2 G_0 \int_{\varepsilon} |M_{ST}(z)|^2 \rho_S(E_F - \varepsilon)\rho_T(E_F + \varepsilon) V d\varepsilon,$$

with $M_{ST}(z)$ the tunneling matrix elements, $G_0 = 2e^2/h$ the conductance quantum and ε the energy of the filled/empty states of the tip/surface, close to the Fermi energy E_F (the validity of the model is limited to an interval of states close to the Fermi energy, which is fulfilled for relatively low voltages).[72] In a typical microscope uses bias voltages below 10 V, for currents up to ~1 µA. In the most common setup, the studied surface of the sample is grounded, while the bias is applied to the metal tip, but the opposite polarity is also possible. The tip itself is mounted on a piezo scanner capable to move along all the three axial directions (X, Y and Z). The measurement is performed by the motion of the tip over the surface and the instrument records a bi-dimensional map of the current intensity, which depends on the local DOS of the sample. Alternatively, the measured current can be compared to a pre-selected value I_{SET} through a feedback system, which controls the vertical position *z* of the tip on the surface, giving a map of z-values instead. Such STM maps can be related to the topography of the surface in

case of a homogenous DOS, while in other cases interpretations of the images are required. A scheme of an STM setup is shown in Figure 2.9, highlighting the relevant parameters described above.
To minimize the influence of the external environment, the STM chamber is mechanically insulated from vibrations and the instrument is kept under vacuum. To reduce the drift of the piezo motors and the atomic diffusion on the sample surface, many microscopes (tip and/or sample) are cooled to low temperatures by the use of either liquid nitrogen or liquid helium.

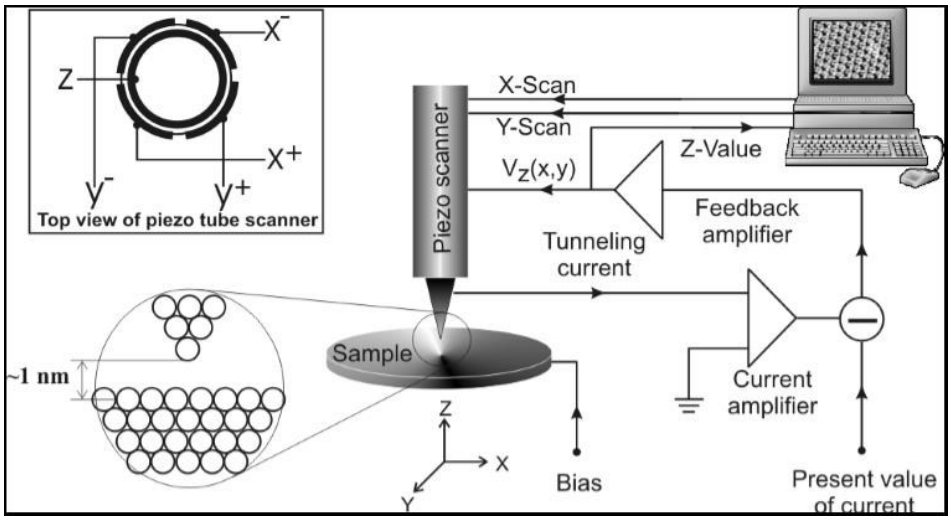

Figure 2.9. A scheme of a typical STM setup, with a piezo stage hovering over the sample and using the measured current with a feedback system controlled by a PC. The image shows the setup for a grounded tip. Adapted from ref. 74.

2.2 Experimental details

2.2.1 Swiss Light Source synchrotron

The Swiss Light Source (SLS) is a third-generation synchrotron light source located at the Paul Scherrer Institut, Switzerland. It uses 2.4 GeV of energy to generate photon beams of high brightness, both in hard and soft X-ray range, to promote research in areas such as materials science, biology, physics and chemistry. The synchrotron itself comprises an electron storage ring of 288 m circumference, which is formed by 36 dipole magnets generating a magnetic field of 1.4 T for achromatic deflection of the electron beam. The SLS hosts multiple beamlines, each using a group of instruments to perform studies by using different investigation techniques. In this Section, three beamlines will be described in a detail, as they were used to perform the main part of the research explained in Chapters 3 and 4.

2.2.2 X-Treme beamline

The X-Treme beamline is a soft X-ray beamline designed to employ linearly and circularly polarized soft X-rays to study the absorption properties of samples under external magnetic field and variable temperature.[73] The X-ray beam is generated by an elliptical Apple II undulator and guided to a plane-grating monochromator that selects energies between 400 and 1800 eV, for a spot size on the sample of ~1 mm^2 in the defocused configuration (when focused the size is ~100 times smaller). The energy range covers the $L_{2,3}$ –edges of 3d transition metals, the $M_{4,5}$ -edges of lanthanides as well as the most common K-edges of organic and inorganic ligands (C, N, O and F). The end-station of the beamline, reported in Figure 2.10, is equipped with a superconducting magnet generating a field up to 7 T in the direction of the photon beam and up to 2 T transverse field. The liquid He cooling of the end-station allows reaching temperatures between 2 and 320 K. The samples can be introduced to the UHV of the system by using a load-lock chamber and positioned in the cryostat via magnetically driven transferring stages. In the cryostat, the sample can be aligned by a vertical motion in a range of 50 mm and can be rotated up to 355° around the vertical axis of the cryostat. The horizontal shift perpendicular to the photon beam is achieved by the motion of the end-station frame. The absorption signal can be measured by total electron yield, transmission or fluorescence. In the current work, the total electron yield was used to measure the absorbed X-rays, as it is the most sensitive technique to measure samples with a thickness up to a few nanometers. The signal is detected by two Keithley multimeters, one connected to the sample and one to the gold mesh grid, positioned before the sample and used to normalize the XAS spectra. The on-the-fly scan mode can be used to acquire spectra with high-density point and a fine resolution. To avoid beam-induced damage of the samples a reduced photon flux can be used by minimizing the exit slit openings and the defocused beam mode. For the present scope, the Er $M_{4,5}$-edge was measured by using the third harmonic of the undulator.
A sample preparation chamber is connected to the measuring chamber through a transfer chamber. The preparation chamber is used to prepare *in situ* samples and it is equipped with different ports allowing connecting molecular evaporators and other instruments. The sample stage can be used for sputtering the substrates with argon and can be heated up to 1800 K and cooled down to 30 K with liquid helium. The system offers a quartz crystal microbalance (QCMB) to measure absorption rates and coverages, and is equipped with a low-energy electron diffractometer (LEED), a mass spectrometer and a chamber with an Omicron variable-temperature scanning tunneling microscope (VT-STM).

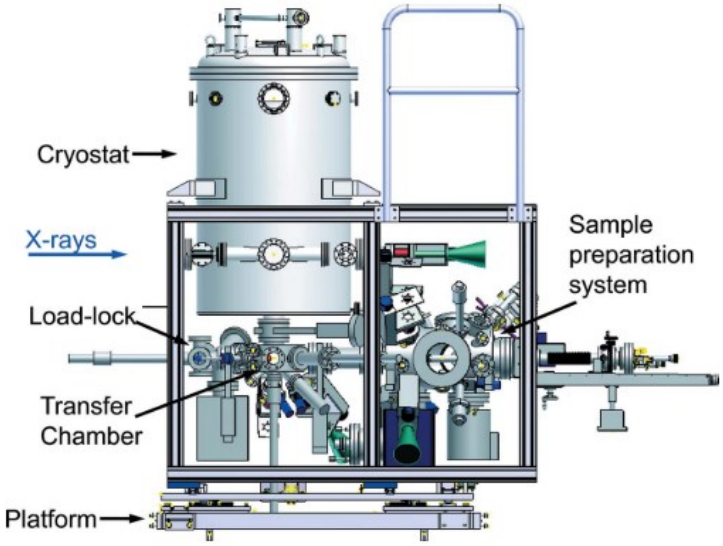

Figure 2.10. Side view of the end-station at the X-Treme beamline. Figure taken from ref. 75.

2.2.3 PEARL beamline

The PEARL beamline is a soft X-ray beamline performing mainly (angle-resolved) X-ray photoemission spectroscopy (XPS) and X-ray photoelectron diffraction (XPD).[74] A bending magnet is used to generate the photon spectrum, which can be linearly polarized in the synchrotron plane or partially circularly polarized. The monochromatic photon beam is selected by a planar grating monochromator in the energy range of 60-2000 eV, with a resolving power E/ΔE of 7000 at 400 eV. The spot size of the beam is about 1.4 mm^2 (used in the present case), while the refocusing mirror can focus the beam onto a spot of ~0.01 mm^2. A Scienta EW4000 hemispherical electron analyzer is oriented to accept photoemitted electrons from the sample at a fixed angle of 60° with respect to the incoming synchrotron light. The analyzer chamber hosts samples that can be rotated by 360° around the vertical axis, as well as around the transversal axis, virtually allowing to orient the sample at any angle toward the beam (with the limitations coming from the Omicron plates used to host the sample). The sample stage can also be moved vertically and along the direction toward the electron analyzer, allowing tweaking the focusing spot of the photo-emitted beam. An analyzer exit-slit is used to control the electron beam flux onto a two-dimensional detector. The end-station, reported in Figure 2.11, consist of the X-ray photoemission setup connected to an Omicron low-temperature scanning-tunneling microscope (LT-STM) via a sample transfer system, which in turn is connected to a sample preparation chamber. The preparation chamber itself is equipped with a multi-pocket molecular beam evaporator based on resistive heating and a QCMB to measure the evaporation rates, while the sample stage can be heated up to 1500 K and actively cooled with liquid nitrogen/helium. An ion gun can be used to

sputter substrates/samples. The samples are generally mounted on specially designed metal Omicron plates, which can be transferred between the different chambers under ultra-high vacuum, with a base pressure of low 10^{-11} mbar. The STM chamber allows cooling down the sample and the STM tip to a temperature of 4.5 K.

The XPS scans were performed using a monochromatic (Δ = 0.1 eV) synchrotron light at 800 eV. For all the scans, a front-end aperture of 3×4 mm^2, an exit slit of 30 µm and a dwell time of 0.5 s per step were used. Survey scans were acquired of all the prepared samples and the freshly prepared Ag(100) surface. Detailed scans were performed with energy steps between 0.03 eV to 0.5 eV. The pass energy was set to 20 eV for the C 1s region and to 50 eV for the other edges. C 1s and Er 4d core levels were acquired for Cp*ErCOT and $K[Er(COT)_2]$, while K 2p and O 1s were acquired only for $K[Er(COT)_2]$.

STM images were acquired by the Omicron LT-STM at 4.5 K and post-processed with Gwyddion (rows alignment, mean plane background removal and scar correction).[75]

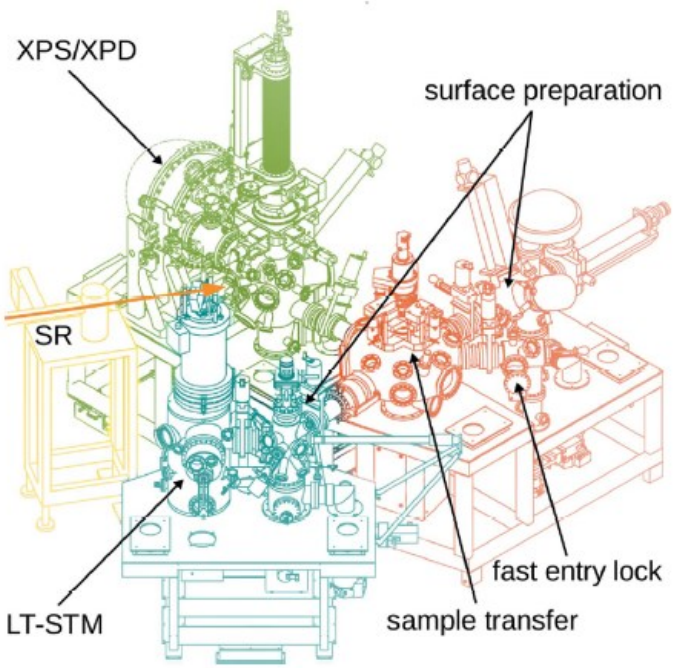

Figure 2.11. Schematic view of the end-station at the PEARL beamline. Figure from ref. 76.

2.2.4 IR beamline

The IR beamline at SLS is designed to study samples in the infrared region of the spectrum generated by the bending magnet of the beamline.[76] The end-station is designed to transport light to four experimental stations, which are performing infrared spectroscopy operating in vacuum, microscopy, high resolution Fourier-transform spectroscopy in vacuum and a pump-probe experiments,

respectively. For the present research, the focus is on the FTIR spectroscopy setup, which is composed by a Bruker HR 125, an interferometer with an optical path of 11.7 m that can provide a high resolution FTIR spectra of up to 0.0008 cm^{-1}. The energy range covered by the instrument extends from far infrared (~10 cm^{-1}) up to the visible/ultraviolet range (~13000 cm^{-1}), with the possibility to optimize the energy range by selecting the appropriate swappable optical components and the detector itself. The photon source can be selected between synchrotron light and the embedded internal source in the form of three different lightbulbs, specifically for far-, mid- and near-infrared. The entire optical section of the interferometer is actively pumped to a base pressure of few mbar in order to minimize the contribution of air to the FTIR spectra. The instrument is equipped with a sample holder compartment for transmission measurements, with the possibility to cool samples down to ~3 K using a specially designed cryostat. Such cylindrical cryostat has two coaxial windows for the transmission of the photon beam and is equipped with a liquid He cooled cold finger and an embedded resistive heater, while the cryostat itself is actively pumped through an external turbo pump. In the near-infrared (NIR) region (3000-9000 cm^{-1}), the interferometer operates with a CaF_2 beam-splitter and a liquid nitrogen-cooled InSb detector. For NIR transmission measurements, the cryostat of the sample holder can be equipped with KBr windows and pumped down to a base pressure of 10^{-6} mbar. The measurements are performed as consecutive scans of the interferogram generated by the moving mirror of the interferometer. The recorded interferograms in the space domain are Fourier-transformed by the OPUS software provided at the beamline into energy spectra, averaged by the number of scans performed.

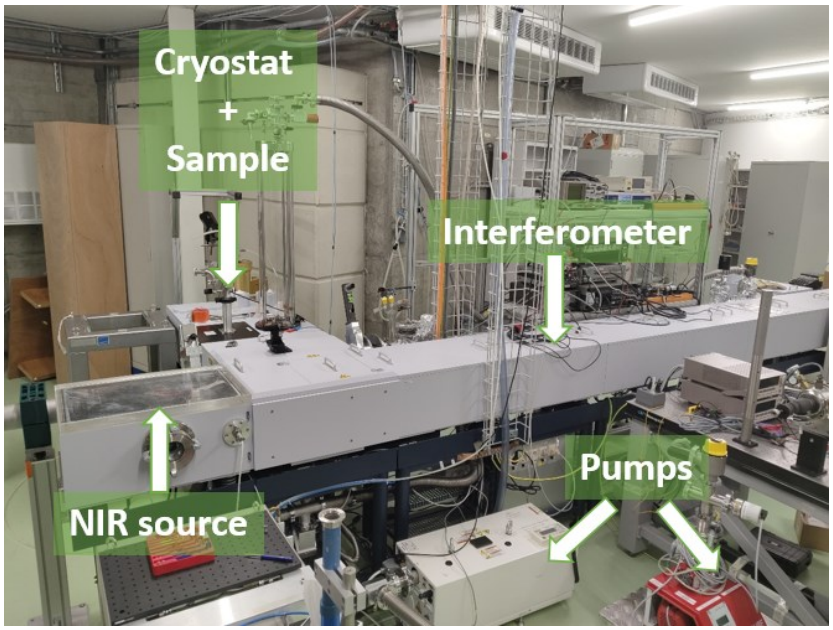

Figure 2.12. Picture of the Brucker HR 125 and the FTIR instrumentation at the IR beamline.

CHAPTER 3

Sample preparation and characterization

In this Chapter the details of the sample preparation employed to study organometallic complexes in the bulk phase, as well as deposited on the (100) surface of Ag in the monolayer range are explained. Polycrystalline powder of [K(18-crown-6)][Er(COT)$_2$]·2THF (also labelled as **1**),[32] [Li(DME)$_3$][Er(COT")$_2$] (**2**),[37] Cp*ErCOT[38] (**3**), Cp^{ttt}ErCOT[39] (**4**) and Cp*YCOT[77] (**5**) complexes were used for the preparation of all samples shown throughout the text. The compounds **1** and **2** were synthesized by the collaborators from the group of Prof. Murugesu of the Department of Chemistry and Biomolecular Sciences of University of Ottawa, while compounds **3**, **4**, **5** and additionally **1** by the group of Prof. Copéret at the Department of Inorganic Chemistry and Applied Biosciences ETH Zurich, following the published recipes in the original papers. Given that the compounds are highly reactive to air and moisture, they were always handled in the inert He environment of a glovebox (H_2O/O_2 < 1 ppm) at the Paul Scherrer Institut. Pictures of the complexes are shown in Figure 3.1. All the equipment used to treat the compounds was previously cleaned by acetone/ethanol, thermally outgassed and/or treated by ultrasonic cleaning. The samples were transferred to the measuring facilities in inert gas overpressure by use of specially designed vacuum-tight suitcases and immediately pumped to high vacuum, minimizing air/moisture interaction.

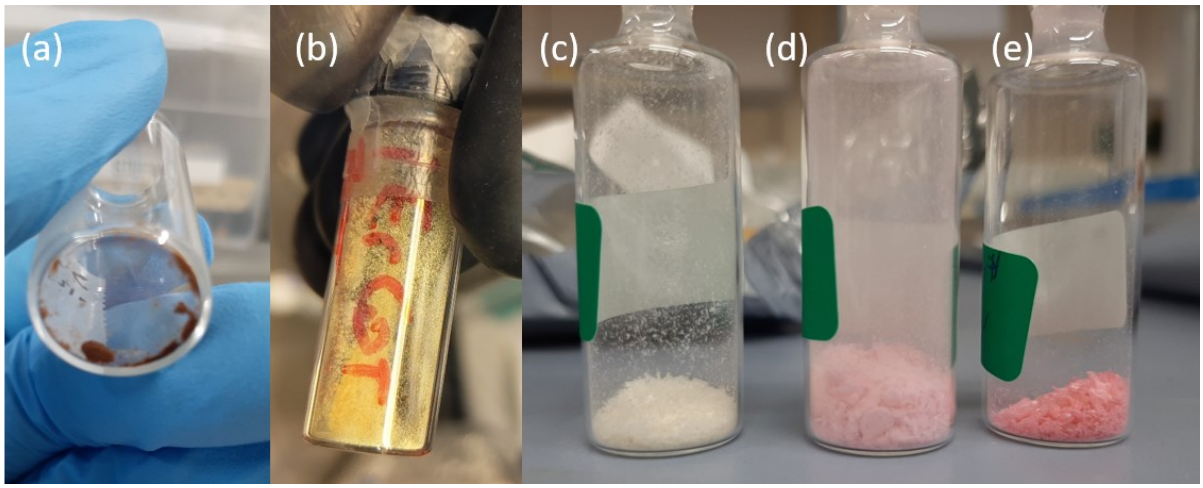

Figure 3.1. Powders/crystallites of the studied organometallic complexes. (a) [K(18-crown-6)][Er(COT)$_2$]·2THF (dark yellow),[32] (b) [Li(DME)$_3$][Er(COT")$_2$] (bright yellow),[37] (c) Cp*YCOT (faint yellow/white), (d) Cp^{ttt}ErCOT (pink)[39] and (e) Cp*ErCOT (bright pink).[38]

3.1 Surface deposition

3.1.1 Thermal sublimation of complexes on Ag(100)

For the preparation of samples deposited on the surface, small quartz crucibles of about 15 × 5 mm (Kentax) were filled with ~10 mg of polycrystalline powder of complexes and transferred via suitcase to the preparation systems of both X-Treme[73] and PEARL[74] beamlines. The degassing and sublimation in ultra-high vacuum was performed by using water-cooled multiple-cell UHV thermal evaporators (Kentax) at the X-Treme beamline and the embedded molecular evaporator at the PEARL beamline. Figure 3.2a shows the quadruple cell evaporator used, where the front side with four cylindrical apertures (labelled) hosting the crucibles are visible. All samples were deposited on a freshly prepared (100) surface of an Ag single crystal, obtained by multiple cycles of Ar^+ sputtering and annealing (up to ~500 °C). Figure 3.2b shows the setup during the sputtering/annealing process of the substrate performed in UHV of the sample preparation chamber at X-Treme beamline.

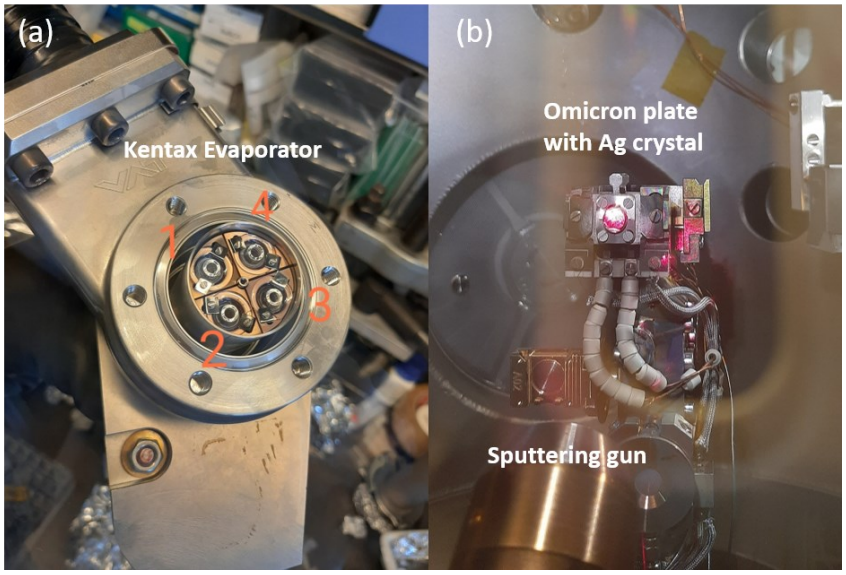

Figure 3.2. (a) Front view of the quadruple-cell evaporator (Kentax) with four labelled crucibles containing powder compounds and (b) view of the sputtering/annealing setup used to prepare fresh Ag(100) surface.

The compounds were thermally degassed up to ~100 °C in ultra-high vacuum (UHV) and moved to the preparation chambers, with base pressures of mid-10^{-10} mbar for both beamlines. The sublimation rate of the compounds was measured as a function of temperature by a quartz crystal microbalance and monitored by changes in the pressure of the preparation chambers. In order to determine the

correct sublimation temperature, test samples were prepared at different temperatures and measured by XPS/XAS. The deposition of **3** was performed by keeping the crucibles at temperatures starting at 100 °C and increasing over the span of several days up to 195 °C, in order to keep the sublimation rate constant. Compound **1** was sublimed at 340 °C to prepare samples at X-Treme beamline and at 360 °C at PEARL beamline. The difference between the two temperatures is linked to the different setups/instrumentations of the beamlines and it was established based on XAS/XPS/STM measurements of test samples. As shown in the next section, sublimations of **1** at lower temperatures produced samples with unreliable stoichiometry of the deposited compound. Higher temperatures induced the degassing of the THF adduct and the crown ether molecules which allowed to deposit $K[Er(COT)_2]$ complexes instead. The latter complex proved to have similar magnetic properties to the bulk precursor, specifically the **1** (see next Chapter for details).[33] Moreover, the stability of the sublimation rate by the quartz balance at 340/360 °C allowed us to deposit reproducible samples of $K[Er(COT)_2]$.

The coverage of the surface was estimated by cross-referencing the rate measured by the quartz balance with the adlayer thickness obtained from the intensities of Ag 3d levels of the substrate (see next section for details) by Equation 2.14, as well as the coverage extracted from the STM scans. The thickness/coverage through the whole text is reported in monolayers (ML), where a ML corresponds to a densely packed coverage of the surface by the sublimed compound, with the height of a sandwich complex.[32,38]

The measurements of the relevant surface-deposited samples are presented and discussed in Chapter 4, while the spectra of additional samples are reported in Appendix B.

3.1.2 Preparation and characterization of $K[Er(COT)_2]$/Ag(100)

To obtain monolayers of $K[Er(COT)_2]$, compound **1** was sublimed onto Ag(100) at increasingly higher temperatures of the crucible, from 107°C up to 360°C. Test samples produced at different temperatures were analyzed to understand the nature of the deposited complexes. Five of those samples, reported in Table 3.1 were selected. Sample B and C were deposited as subsequent sublimation of compound **1** in 3 and 5 depositions at increasing temperatures, respectively, labelled as eg. 200 - 320 °C and 320 - 360 °C. These two samples are useful to understand the type of species that are sublimed at these temperatures, as described further below. Although all the samples have different coverages and stoichiometry, their chemical composition could be estimated from the photoemission spectra. The stoichiometry is extracted from survey scans similar to the one shown in Figure 3.3a, with the fractions of elements reported in Table 3.1 and compared to the expected

fractions of K[Er(COT)$_2$] and its precursor **1**. The error bars were estimated on average as ~15% of the signal (with larger errors for smaller coverages). To obtain the stoichiometry from the spectra, the energy-dependent cross sections and asymmetry parameters were taken from tables reported in the literature (see also Section 2.1.6).[70] The Lambert-Beer law was used to estimate the sample coverage from the attenuation of the 3d core level peaks of the Ag substrate, shown in Figure 3.3b, considering the electron escape depth of incoming electrons with energy E_{el} = 800 eV. [78]

Table 3.1. Fraction of the elements detected by XPS survey scans present on the test samples obtained by evaporating [K(18-crown-6)][Er(COT)$_2$]·2THF onto the Ag(100) surface, compared to the expected fractions of the precursor and K[Er(COT)$_2$]. The error bars amount to ~15% of the value indicated for samples A – E. Hydrogens are omitted from the fractions.

Label	Sample	Carbon (%)	Oxygen (%)	Erbium (%)	Potassium (%)
	Calculated K(18-crown-6)Er(COT)$_2$·2THF	78	17.6	2.2	2.2
A	0.4 ML (107 °C)	66	33	< 1	0
B	1 ML (200 – 320°C)	76.7	17	1.3	5
C	7 MLs (320 – 360 °C)	86.3	4.8	5.1	3.8
D	0.5 ML (360 °C)	82.6	10.5	4	2.9
E	8 ML (360 °C)	90.3	< 1	4.4	4.3
	Calculated K[Er(COT)$_2$]	89	0	5.5	5.5

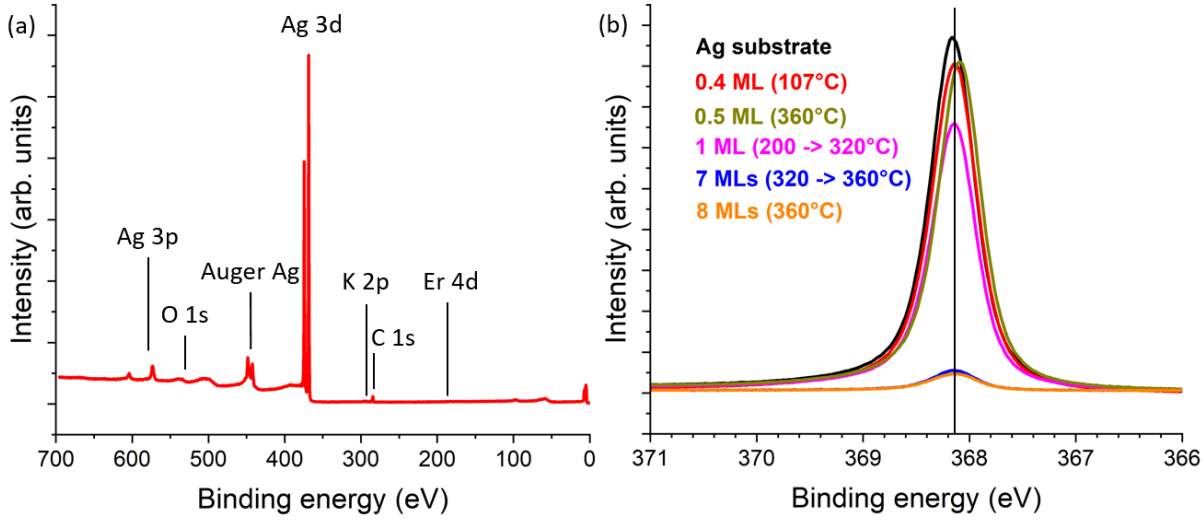

Figure 3.3. (a) XPS survey scan at 800 eV photon energy of 0.5 ML K[Er(COT)$_2$]/Ag(100) deposited (for 20 s) at 360 °C. The position of core levels is indicated by vertical lines. (b) Normalized Ag 3d$_{5/2}$ core level of the samples reported in Table 3.1. The vertical line indicates the position of the level.

Detailed XPS core level scans of C, O, Er and K as a function of the crucible temperature and coverage of the samples are reported in Figure 3.4. The spectra were normalized by the Fermi level position.

The background removal was performed by subtraction of a Shirley function in the C 1s and K 2p spectra, as well as spectra of Er 4d level of higher coverage samples (7 and 8 MLs), which display a larger signal-to-noise ratio. The Er spectra of samples with lower coverage and all the O 1s spectra a simple straight line was subtracted, due to a poor fit of the Shirley function. The spectra of the C 1s core level shown in Figure 3.4a have the main carbon peak normalized to unity, for a better comparison of the features and chemical shifts. The intensities of the other levels are normalized by the same factors used to normalize the C 1s, to visualize the scaling of the intensity relative to that of the carbon.

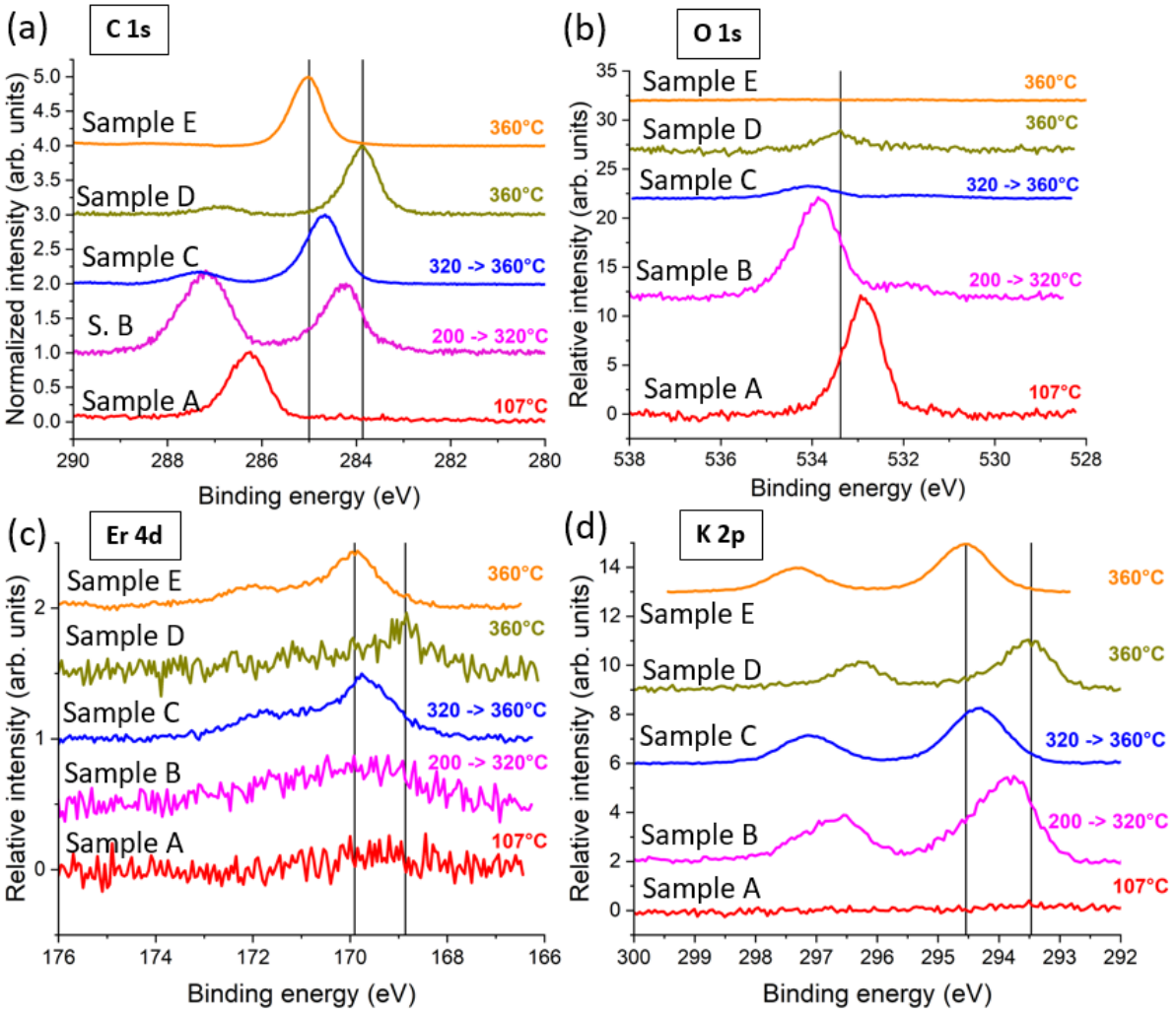

Figure 3.4. XPS spectra of (a) C 1s, (b) O 1s, (c) Er 4d and (d) K 2p core levels of compound **1** deposited at different crucible temperatures on a Ag(100) substrate. While the C peak is normalized to unity, the other peaks are scaled by the same factors used for the C peak. The details of the samples from A to E are reported in Table 3.1. The black vertical lines indicate the central position of the main core levels of samples prepared at 360 °C.

From the spectra in Figure 3.4 and the stoichiometry of the samples reported in Table 3.1 it is possible to guess the chemical species present on the surface. Figure 3.4 shows that when the complex is

sublimed at 107°C (red curves), a strong presence of carbon at 286.3 eV and oxygen at 532.9 eV are detected, while the amount of erbium and potassium is essentially negligible. The peaks are attributed to the carbon and oxygen of the C-O bond, due to the deposition of large amounts of (18-c-6) crown ether molecules on the surface.[79,80] This is more reinforced by the absence of a clear sp^2 carbon peak that would appear in the presence of tetrahydrofuran (THF) and/or $K[Er(COT)_2]$ complex.[81]

A subsequent deposition at crucible temperatures from 200°C to 320°C was used to prepare sample B (purple curves). The presence of C, Er and K elements is detected. Together with a strong O 1s peak, the presence of these elements and two different carbon species suggests that the sample has similarities with the stoichiometry of compound **1**. Indeed, the starting compound has 16 aromatic carbon atoms of the two COT^{2-} ligands and 4 carbon atoms of the 2 THF molecules contributing to the same peak, while 12 oxygen-bound carbon atoms in the crown ether and 4 in the 2 THF contribute to a second peak, at higher binding energy. An XPS spectrum of the pure compound would have an area ratio of the two peaks amounting to 1.25, assuming negligible chemical shifts. Sample B shows a ratio of the two carbon peaks areas of 1.36 (obtained from fits using Voigt functions), which is in good agreement with the expected ratio, although the amount of K and Er deviate from the expected values.

Similarly, to sample B, sample C was prepared by subsequent depositions at crucible temperatures between 320-360°C (blue curves). The sample shows a dominant peak corresponding to the carbon specie of the aromatic rings. The strong Er and K presence, the weak C-O carbon signal at higher binding energies and the weak contribution of oxygen suggest that the dominant specie on the surface is $K[Er(COT)_2]$. From the blue curve in the C 1s spectra it is possible to deduce that the ratio between the C-O and aromatic carbon peaks is only 0.23, corresponding to about 1 crown molecule every 3 $K[Er(COT)_2]$ complexes.

At a temperature of 360°C (dark yellow and orange curves), the presence of potassium, erbium, the (almost) negligible oxygen and mainly the carbon peak ascribed to the aromatic specie suggests that $K[Er(COT)_2]$ is deposited at this temperature, in agreement with the reported stoichiometry (Table 3.1). While for sample D (0.5 ML) the presence of oxygen suggests residual THF/crown ether molecules, the multilayer sample E (8 MLs) matches well the expected stoichiometry of $K[Er(COT)_2]$, possibly because of a stronger Er and K signals, used in the normalization of the signal. For the sample with larger coverage, the negligible traces of carbon bound to oxygen in the C 1s range and the absence of the oxygen peak is the confirmation that the (18-c-6) crown ether and the THF molecules are sublimed at temperatures lower than 360°C.

In order to deposit monolayers of $K[Er(COT)_2]$ on Ag(100) the temperature of 360°C was used. As explained in the Results and discussion section, the stoichiometry and designation of the samples with the $K[Er(COT)_2]$ molecule fits with the results obtained with other experimental techniques.

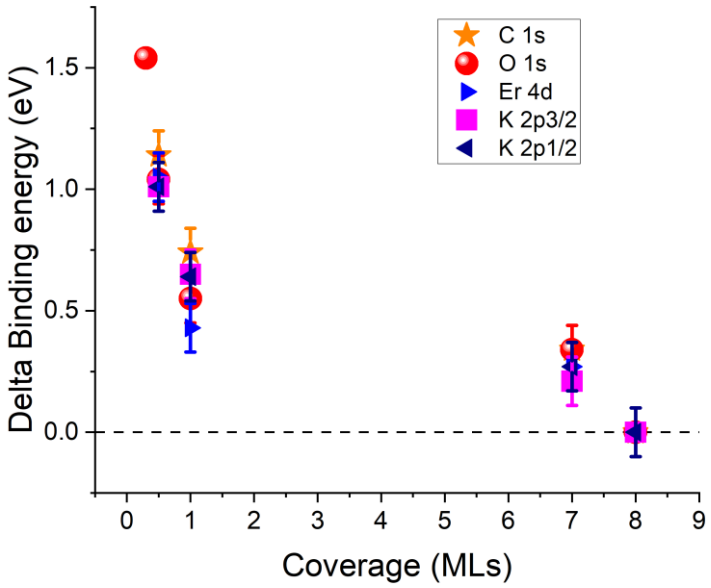

Figure 3.5. Thickness-dependent shift of the XPS core levels of $K[Er(COT)_2]$ SMMs deposited on Ag(100), extracted from the core level positions in Figure 3.4. The error bars are given by the FWHM of the different peaks.

Moreover, the spectra reported in Figure 3.4 show a thickness-dependent shift of all core levels toward higher binding energies with increasing thickness of the samples. While the sub-monolayer samples have the lowest binding energy for all core levels, samples with increasingly larger coverage, represented by purple, blue and orange curves, show a progressive shift of all levels toward higher binding energy. The two boundaries, given by the ~0.5 ML (dark yellow) and the ~8 MLs (orange) samples, have the core levels shifted on average by 1.05 ± 0.06 eV with respect to one another, as indicated by the position of black vertical lines in Figure 3.4 (excluding oxygen). This effect is also reported in the Figure 3.5, where the relative shift of all the peaks toward lower binding energy vs estimated coverage is plotted. The shifts have been attributed to the charge segregation of the complex at the surface, which causes the formation of a built-in potential, affecting the XPS core levels, as discussed in Chapter 4.

3.2 Bulk spectroscopy

3.2.1 Embedding of complexes in solid matrices

To measure the FTIR spectra of the organometallic complexes in transmission mode, the powder of the compounds was dispersed in solid matrices such as KBr and eicosane. KBr is a rock salt material transparent in the NIR range that can be used to dilute other powders and then press them into solid pellets, which are practical for transmission measurements. Ground KBr (Sigma Aldrich) was degassed at 120 °C in a Schlenk line under vacuum, sealed and introduced to the glovebox where the sample preparation occurred. To produce the pellets of the molecular complexes, two setups were used: a manual press constituted by a nut and two bolts with polished surfaces, producing cylindrical pellets with a diameter of 10 mm, and a mechanical press, producing pellets with a diameter of 13 mm.
The equipment was degassed at temperatures above 100 °C in inert He environment of the glovebox prior to the sample preparations and care was used to minimize the contamination of the highly reactive complexes. To obtain a good signal-to-noise ratio, an amount of complexes equivalent to 10-15% of the total mass was used, with a typical total mass of ~100 mg (KBr + complexes). The sample parameters are reported in Table 3.2.

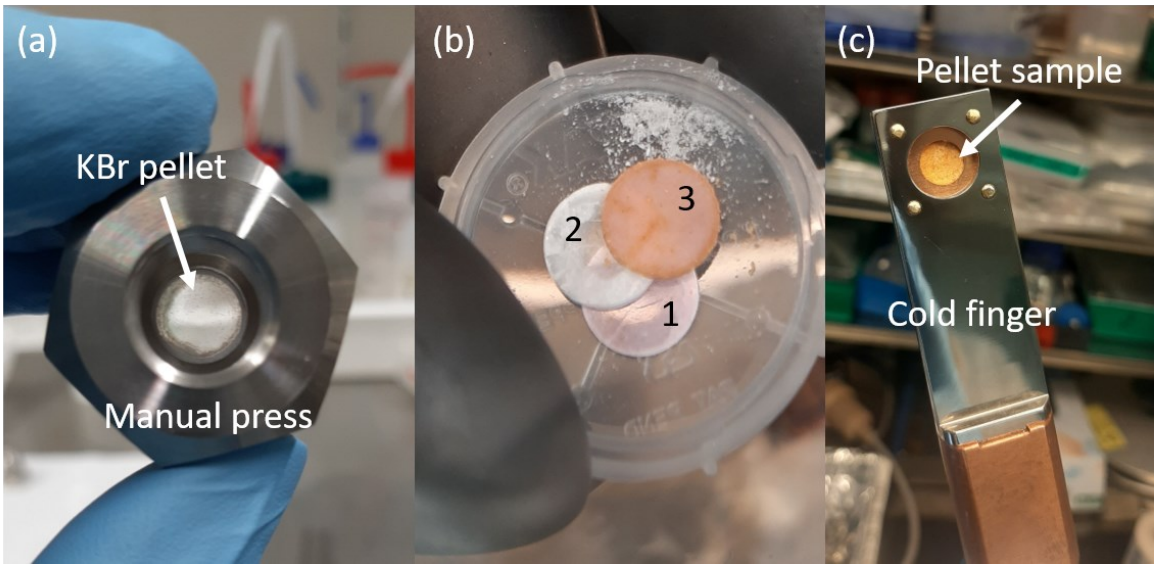

Figure 3.6. (a) Manual press used to produce part of the pellet samples, together with a freshly prepared KBr pellet; (b) pellet samples of (1) Cp*ErCOT diluted in KBr, (2) KBr and (3) Cp*ErCOT:KBr after measurements; (c) cold finger of the cryostat with a pellet of [K(18-crown-6)][Er(COT)$_2$]·2THF:KBr mounted.

For the background removal, a KBr pellet with a total amount of mass of ~100 mg was used. A typical KBr pellet produced in the nut press is shown in Figure 3.6a. A similar principle was employed with the mechanical press, where the pressure was applied on the powder through a polished metallic cylinder

in a metallic guide. Some produced pellets are shown in Figure 3.6b. The samples were transferred onto the cold finger of the cryostat used to measure the FTIR signal (Figure 3.6c) and sealed in the inner compartment of the cryostat at few mbar of overpressure of the glovebox. The thermal contact to the cold finger was ensured by clamping the pellet between two ~1 mm thick copper masks, directly in contact with the cold finger.

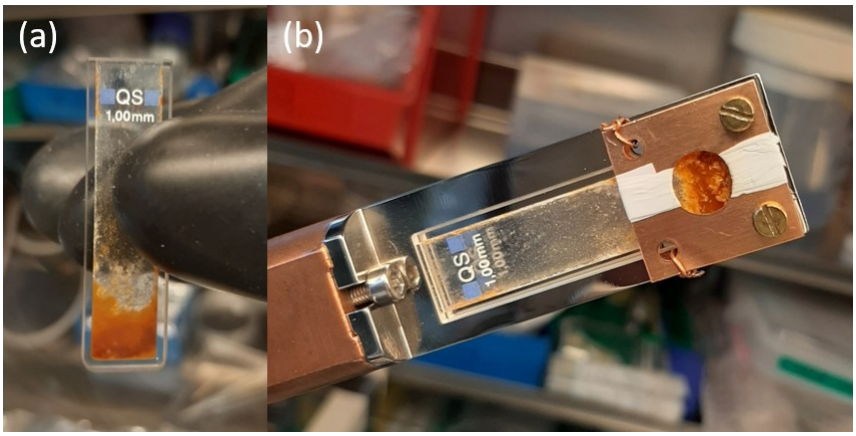

Figure 3.7. (a) NIR-grade quartz cuvette containing $[Li(DME)_3][Er(COT'')_2]$ dispersed in solid eicosane and (b) mounted on the cold finger of the cryostat, clamped with a copper mask.

Table 3.2. Parameters of complexes dispersed in matrices (KBr/eicosane) used to produce samples of specified diameter and thickness for the FTIR spectroscopy, as reported in the present and the following Chapters. An experimental error of 0.05 mm (in brackets) is attributed to the measured thickness.

Sample	Diameter (mm)	Thickness (mm)	Sample mass (mg)	Matrix	Matrix mass (mg)
$[K(18\text{-crown-6})][Er(COT)_2]\cdot 2THF$	10	0.3(5)	12	KBr	67
$[Li(DME)_3][Er(COT'')_2]$	/	0.1	16	Eicosane	82
Cp*ErCOT	13	0.3(5)	11	KBr	89
Cp^{ttt}ErCOT	13	0.3(5)	10	KBr	89
Cp*YCOT	13	0.3(5)	10	KBr	90

Similarly, eicosane, which is an alkane material with the consistency of a wax and a melting point of ~38 °C, can also be used as a matrix for molecular compounds to be measured in the NIR region, where it is transparent to a certain degree. To ensure that the FTIR spectra of the complexes do not change upon changing the matrix material, a sample with a mixture of ~100 mg of eicosane (Sigma Aldrich) added to ~20 mg of $[Li(DME)_3][Er(COT'')_2]$ was prepared. The mixture of the two powdered compounds was transferred into a NIR-grade quartz cuvette with an internal thickness of 1 mm, for a total optical path of 3 mm (Figure 3.7a), and heated up above the melting point of eicosane by a hot plate inside the glovebox.

After the cooling of the cuvette, the mixture solidified again. The resulting sample was clamped to the cold finger of the cryostat with the help of copper mask (rubber tape was used on one side to improve stability and avoid the scratching of the cuvette). For the normalization of the spectra, another sample was prepared following the same procedure by using only eicosane in the same quartz cuvette. The spectra are reported in the next section.

3.2.2 IR characterization

The absorbance signal was obtained from FTIR spectra measured in transmission mode. The Fourier-transformed transmission spectra of the KBr pellet and eicosane in a quartz cuvette were acquired between 3000 and 8700 cm^{-1} at 3 K, as reported by the normalized spectra in Figure 3.8a. The spectra were used to normalize the transmission spectra of the organometallic complexes. In the energy region between 6000 and 7000 cm^{-1}, KBr shows an almost linear decay of the transmission signal. Contrary, eicosane show several features, although no sharp peaks with the typical width of Ln^{3+} intra-4f transitions were detected.

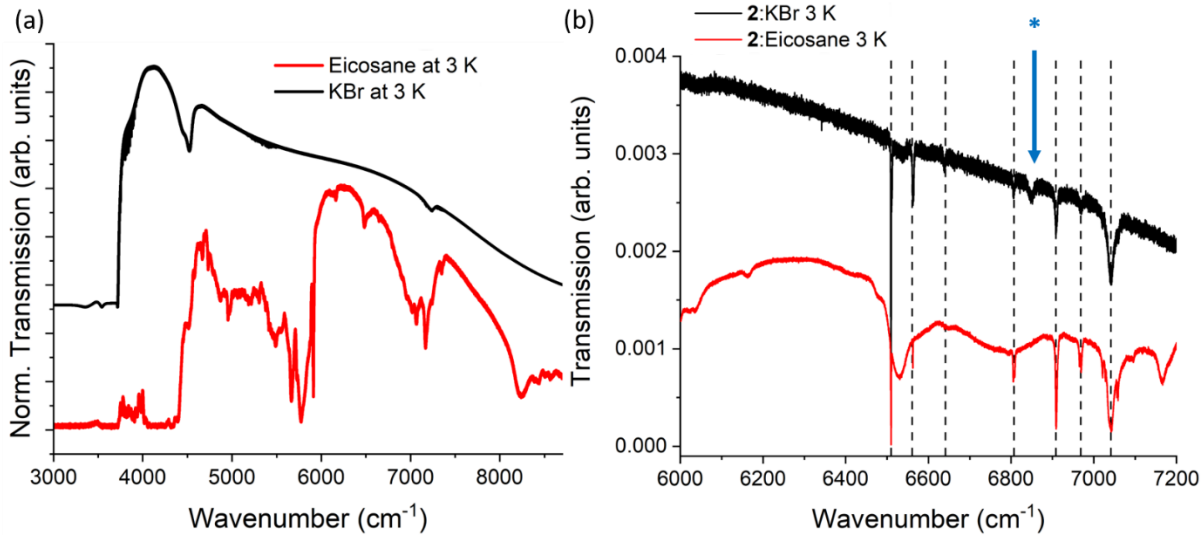

Figure 3.8. (a) Normalized transmission spectra of eicosane and KBr acquired in the NIR region by FTIR spectroscopy at 3 K; (b) transmission spectra at 3 K of $[Li(DME)_3][Er(COT'')_2]$ (**2**) diluted in KBr and eicosane. The dashed lines correspond to the same positions of intra-4f transitions detected in the two sample. The peak labelled as * (blue) for **2**:KBr is detected in the sample **2**:eicosane starting from 10 K.

To investigate the effect of the matrices used to disperse the compounds onto the 4f-4f transitions of the Er^{3+}-based organometallic complexes, compound **2** was diluted both in KBr and eicosane (labelled as **2**:KBr and **2**:eicosane, respectively) according to the procedures explained in the previous section. The transmission spectra of both samples are reported in Figure 3.8b, where dashed lines show the

same 7 transitions from the ground state manifold $^4I_{15/2}$ to the first excited manifold $^4I_{13/2}$ of Er^{3+}, as further addressed in the next Chapter. The only exception is constituted by the peak labelled * (blue arrow) at 6847.8 cm^{-1} that was detected for compound **2**:KBr at 3 K but for compound **2**:eicosane starting from 10 K. This difference suggests that the actual temperature of sample **2**:KBr was higher than 3 K. The position of the IR transitions, reported in Appendix B, proved that the nature of the matrix used have only a minor effect on the optical transitions, if any at all. As introduced previously, the temperature-dependent FTIR spectra of compound **2** reported in the next Chapter are measured on the sample produced with the eicosane matrix.

To obtain the absorbance of the compounds, the transmission spectra were normalized by the spectra of the "background" signal, spectra acquired at 3 K of the optical components along the photon beam path and a pellet of KBr or cuvette of eicosane as a sample, with virtually the same thickness. From the logarithm of the resulting spectra, representing the absorbance, a linear background is subtracted, such that the absorbance spectra are background-normalized (unless stated otherwise). The absorption spectra reported in the next Chapter are relative to the complexes reported in Table 3.2, where the molar mass is indicated. The molar mass is used to extract the cross sections of the 4f-4f transitions according to Equation 2.17, as explained in the next Chapter.

Table 3.2. Molar mass of the organometallic complexes used to extract the absorption cross section of the most intense peaks shown in Chapter 4. The values were taken from the original papers.[32,37–39]

Label	Complex	Molar mass (g/mol)
1	$[K(18\text{-crown-6})][Er(COT)_2]\cdot 2THF$	823.2
2	$[Li(DME)_3][Er(COT'')_2]$	941.6
3	Cp*ErCOT	406.6
4	$Cp^{ttt}ErCOT$	504.8

To prove that the absorption peaks in the energy range corresponding to 5500 and 7000 cm^{-1} are due to the 4f-4f transitions of Er^{3+}, FTIR spectra of compound **3** and the non-magnetic analogue compound **5** were compared. Figure 3.9a shows that at lower wavenumbers both complexes show overlapping and complex multi-peaked spectra. Given that both compounds show the same peaks, they were attributed to the roto-vibrational modes in common by the two complexes. Figure 3.9b shows that at higher wavenumbers, between 6200 and 7000 cm^{-1}, the magnetic compound **3** shows several transition lines, while the non-magnetic compound **5** shows a flat region and a clear absence of any feature. Since Y^{3+} has a closed f shell, the 4f-4f transitions do not occur in compound **5**, proving that the transition lines of Er^{3+} - based complexes in this energy region can be attributed to weakly allowed intra-4f transitions, as discussed in the previous Chapter.

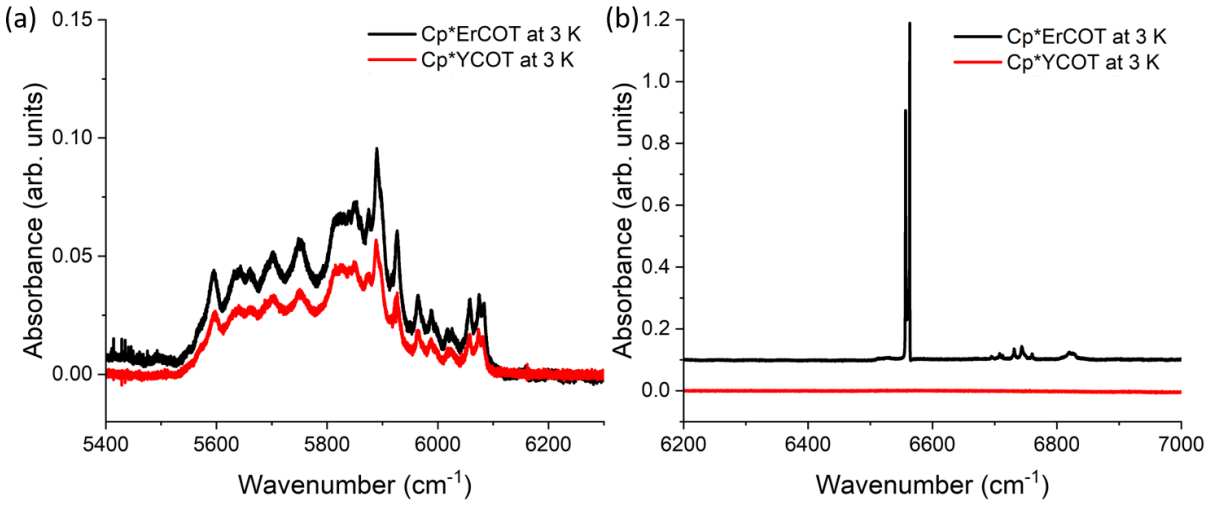

Figure 3.9. FTIR absorption spectra of Cp*ErCOT (**3**) and Cp*YCOT (**5**) SMMs acquired at 3 K showing (a) roto-vibrational modes in common by the two compounds and (b) 4f-4f transition lines for the magnetic compound **3** and a flat background for the non-magnetic compound **5**.The spectra in (b) are offset for better visualization.

To further understand the effect of air/moisture on the decay process of the complexes, two methods were used. The most intuitive one is the direct observation of the color of the complexes before and after exposing them to air. In fact, all the compounds show a clear color change when exposed to air, with complexes **1** and **2** becoming dark orange after few minutes of exposition to air and dark grey/black after several hours. In a similar way, compounds **3** and **4** become pale, tending to white after exposing the samples to air for a few minutes.

The second method involved the measurement at 3 K of a sample containing complex **2** before and after exposing it to air. The results in Figure 3.10 show that the sample kept in vacuum shows sharp absorption peaks in the energy region corresponding to the transitions from Er^{3+} $^4I_{15/2}$ manifold to the first excited manifold $^4I_{13/2}$. After exposing the sample to air for several hours and measuring it again, the spectrum show the absence of sharp absorption peaks but a rather blunt peak with a width spanning on few hundreds of cm^{-1}. The presence of sharp transition lines has been attributed to the integrity of the complexes in the measured compounds. Note that the different signal-to-noise of the two curves is given by different number of spectra used for the averaging procedure.

Several temperature-dependent measurements were repeated in ascending and descending temperature order after it was noticed that thermal treatment of the complexes induced the degradation of the compounds, which showed large broadenings of the peaks previously absent. The spectra shown in Chapter 4 are associated to samples with the best quality/integrity, according to the criteria explained in this Section.

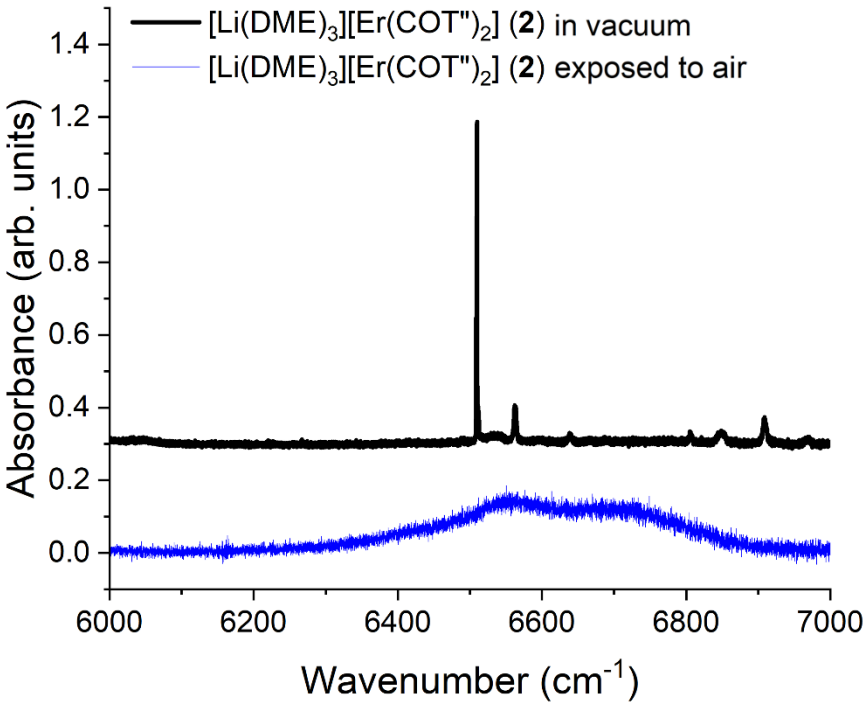

Figure 3.10. Absorption spectra at 3 K of compound **2** in the energy region corresponding to the transitions from Er^{3+} $^4I_{15/2}$ manifold to the first excited manifold $^4I_{13/2}$ before and after exposure to air.

Chapter 4
Results and discussion

4.1 Surface-supported single-molecule magnets

The results presented in this Section are based on a manuscript in preparation with co-authors: Moritz Bernhardt, Martin Heinrich, Diana Vaclavkova, Katie Harriman, Niéli Daffé, Bernard Delley, Maciej Damian Korzyński, Matthias Muntwiler, Christophe Copéret, Muralee Murugesu, Frithjof Nolting and Jan Dreiser.[82] The authors have contributed to the project as specified in the footnote.[1] The XPS and STM data reported in this section are results of the beam time with proposal No. 20211913 at the PEARL beamline, SLS (PSI). The Figures, Tables and the text presented in this Section is partially adapted or fully reported from the manuscript to be published.[82]

4.1.1 X-ray photoemission spectroscopy

Two samples of 0.5 MLs K[Er(COT)$_2$] and ~1 ML Cp*ErCOT were produced on the (100) surface of Ag (see Chapter 3 for details). Normalized XPS spectra in Figure 4.1a show that the main contribution to the C 1s core level of Cp*ErCOT/Ag(100) is centered at a binding energy of 285.0 eV (FWHM 0.7 eV) while a shoulder is present at 285.9 eV (FWHM 0.9 eV). The former peak to the carbon atoms is ascribed to the aromatic rings of COT and Cp* ligands while the latter to the methyl groups of the Cp* ring. The ratio of the two peaks area amounts to 2.7 ± 0.1, which is in very good agreement with the 2.6 ratio of the two carbon species (13 vs 5). The carbon atoms belonging to the aromatic rings show essentially the same energy of the core level, in line with the reported C 1s energies of other π ring-

[1] M. Bernardt, M. D. Korzyński, C. Copéret have prepared the [K(18-c-6)][Er(COT)$_2$]·2THF, Cp*ErCOT, Cp^{ttt}ErCOT and Cp*YCOT complexes. K. Harriman and M. Muralee have prepared the [K(18-c-6)][Er(COT)$_2$]·2THF and [Li(DME)$_3$][Er(COT)$_2$] complexes. M. Heinrich and M. Muntwiler helped to acquire and analyse XPS and STM data. B. Delley provided meaningful insight into the multiX method. D. Vaclavkova, N. Daffé and J. Dreiser have contributed to the data acquisition and analysis of XAS, XPS and STM measurements. F. Nolting and J. Dreiser have contributed with the discussions regarding data analysis and paper preparation. J. Dreiser and V. Romankov have both contributed to the design of the experiments. V. Romankov has contributed with the execution of all the experiments presented in the current Section 4.1, the sample preparation, the data acquisition and analysis, as well as the preparation of the Figures and Tables. V. Romankov is also the first author of the paper in preparation, titled "Influence of self-assembly on the magnetic properties of Er(III) cyclooctatetraenide-based single-molecule magnets deposited on Ag(100)".[82]

like ligands in the bulk and on the surface.[83–85] The rather small FWHM and the absence of asymmetries of both peaks points toward only a minor effect of the screening due to the metallic surface.

On the contrary, the K[Er(COT)$_2$]/Ag(100) has the main peak of the C 1s core level at a binding energy of 283.9 eV (FWHM 0.8 eV) and an extra peak at 286.9 eV (FWHM 1.1 eV). The peak with the largest area is attributed to the carbon atoms of the COT rings while the higher energy peak is attributed to the C atoms bound to oxygen, due to the presence of THF and crown ether in the precursor complex, as described in the Chapter 3.

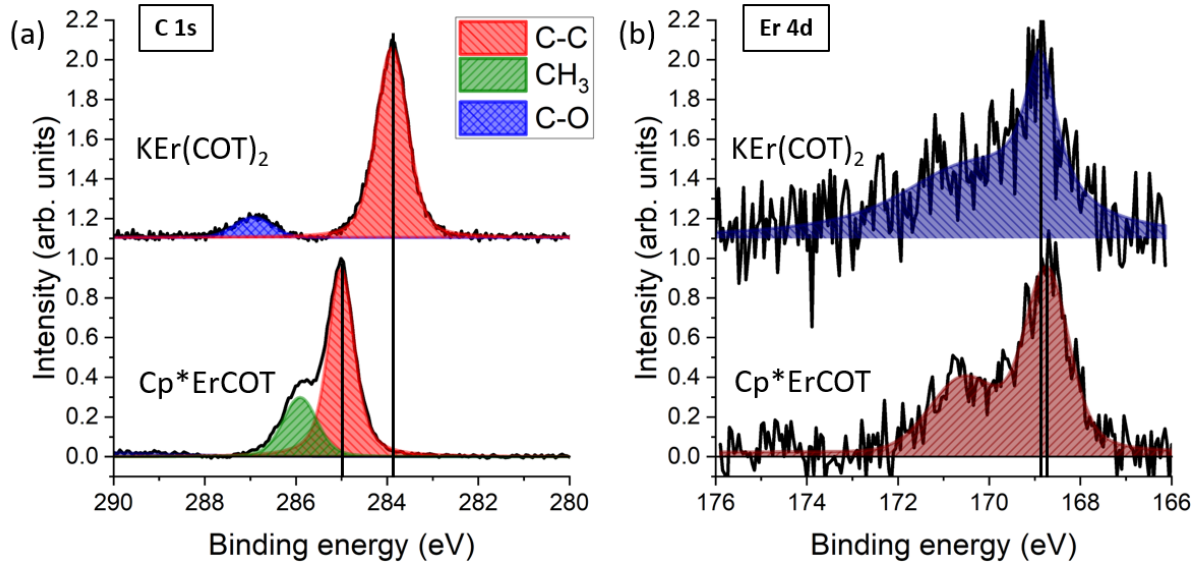

Figure 4.1. (a) C 1s and (b) Er 4d core level spectra of Cp*ErCOT(1 ML)/Ag(100) and K[Er(COT)$_2$](0.5 ML) on Ag(100), normalized to the most intense C/Er peak, indicated by a solid vertical line. Adapted from ref. 84.

Figure 4.1b shows the Er 4d core level, with the main peak of the Cp*ErCOT SMMs centered at 168.7 eV, while the one of K[Er(COT)$_2$] lies at 168.9 eV, characteristic energies for the trivalent Er^{3+} ion.[86] In order to obtain the stoichiometry from the XPS scans, the energy-dependent cross sections and asymmetry parameters were taken from tables reported in the literature.[70] The extracted C:Er atomic ratio for the Cp*ErCOT SMMs is 21:1, while the K[Er(COT)$_2$] shows a C:Er ratio of 16:1 and a K:Er ratio of 0.8:1 and O:Er ratio is 2.5:1. Despite a considerable error due to the weak Er 4d signal these values are in excellent agreement with the atomic ratios expected from the molecular structures, which points to the presence of intact complexes on the surface.

4.1.2 Scanning-tunneling microscopy

The STM images of K[Er(COT)$_2$] (0.5 ML)/Ag(100) and Cp*ErCOT(1 ML)/Ag(100) samples were acquired at 4.5 K. Figure 4.2a shows a 20 × 20 nm^2 image of a complete surface covered by a layer of Cp*ErCOT SMMs, where alternating rows of brighter and darker spots can be identified. The domains formed by the rows extend laterally by a few tens of nanometers and cover densely the surface. The average distance between two rows of bright spots amounts to 1.48 ± 0.04 nm, while the distance between two local height maxima along the same row is 0.84 ± 0.05 nm. The different spots are ascribed to the complexes self-assembled in two different configurations on the surface. By identifying the orientation of the complexes with the direction of the main rotational axis (between the two ligand rings and the Er ion) it is possible to distinguish the configurations as perpendicular (standing-up) and parallel (lying-down) to the surface. The distances between the spots are consistent with the formation of alternating rows of complexes in the two configurations. In some parts of the islands, the ordering of the complexes suggests a herringbone structure in the direction perpendicular to the rows, as shown by the black pattern in Figure 4.2a. This can be explained by the orientation of the axis of lying-down complexes being not perpendicular to the rows, but tilted at an angle, as shown by the overlay in Figure 4.2b. The distance between two standing-up complexes in this tilted direction amounts to d = 1.54 ± 0.04 nm, perfectly matching the distance of 1.55 nm (at 10 K) that the complexes have along the [-101] direction in the bulk crystals, with the same standing-up and lying-down geometry.[38] However, no symmetry plane of the bulk crystal is reproduced in this case, possibly due to the lower-dimensionality boundary exerted by the substrate on the self-assembled SMMs.

The bright spots in Figure 4.2b are ascribed to the upright complexes, with the Cp* ring being on the top side, resembling in size and shape the one reported for Cp*Ru molecules on graphene.[87] While the bright lobes of the lying-down complexes are attributed to the methyl groups, the darker areas are attributed to the poorly conducting COT rings in the direction perpendicular to the π-bonds.[88,89] From the Figures 4.2b and 4.2c, the molecular density is estimated to ~1.7 complexes/nm^2.

Figure 4.2c shows a zoom of the same area reported in the Figure 4.2a but acquired at 2 V and 500 pA. The apparent height of the two rows in this sampling condition becomes comparable and the lying-down complexes are seen as a single bright spot, possibly due to an enhanced conduction through the Er ion. The overlay shown in the Figure suggests that the herringbone structure mentioned previously is originating from the alternating orientation of the complexes in consecutive lying-down rows. The superstructure formed by the complexes can be described by the unit cell reported in Figure 4.2c, with $a_1 \times a_2$ = 0.84 × 2.96 nm^2, with the vectors oriented parallel to the crystallographic [010] and [001] directions of the substrate. The black dotted line shows the lateral

shift of 0.15 ± 0.02 nm that every second-row experiences. It was also noticed (as on top right side of Figure 4.2a) that defect rows are present on the surface in form of three consecutive rows of standing-up complexes, in agreement with the XAS measurements shown further below. A larger area scan reported in Figure 4.2d shows the extent of the defects and the dense coverage of the surface. Figure 4.2e shows that Cp*ErCOT follows the terrace steps of the substrate. The crystallographic directions of the substrate were identified by atomically resolved scans of freshly prepared Ag(100) surface, as shown in Figure 4.2f. (Note that the crystallographic directions of the substrate in images in Figure 4.2 are different since they were acquired at different rotational angles of the piezo motors compared to the substrate).

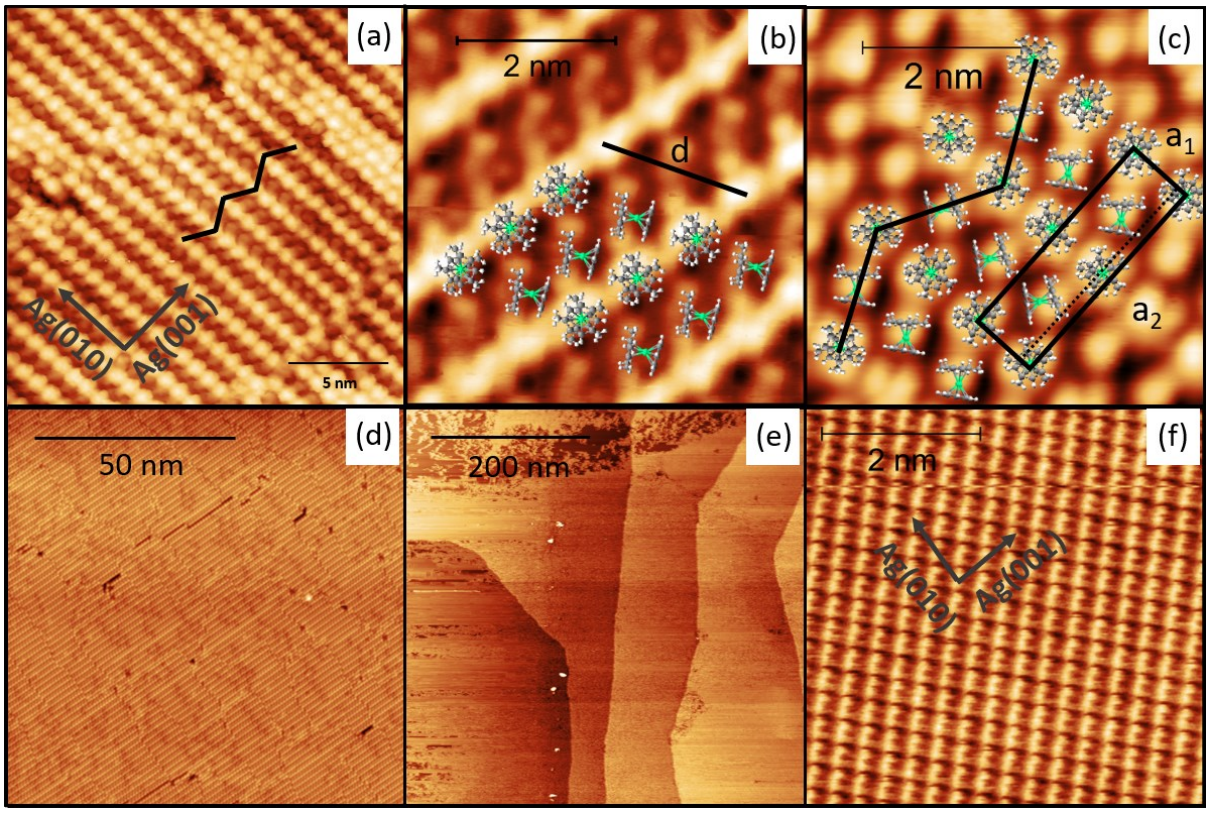

Figure 4.2. Constant-current STM images at 4.5 K of Cp*ErCOT/Ag(100). The imaging conditions are: (a) 200 pA, 0.8 V; (b) 50 pA, 0.25 V; (c) 500 pA, 2 V; (d) 50 pA, 0.25 V; (e) 50 pA, 0.25 V; (f) 80 pA, 1 V. Overlays of the complexes, the herringbone structure, the substrate symmetry directions and the unit cell are shown, as explained in the text. Colors: green is Er, dark grey is C while light grey is H. Adapted from ref. 82.

The STM images of K[Er(COT)$_2$](0.5 ML)/Ag(100) are reported in Figure 4.3. Two different domains of highly ordered complexes, labelled as 1 and 2, can be seen in Figure 4.3a, with the orientation of the rows indicated by black arrows. In both domains, the directions labelled as A_1, A_2 and B_1, B_2 form an angle of 75°. The direction labelled A_1 is rotated clockwise by ~35° with respect to Ag(001), while the one labelled B_1 is rotated clockwise by ~80°. In addition, the directions representing the superstructure

in domain 2 in Figure 4.3a are mirrored with respect the $A_2(B_2)$ vector, so that by rotation symmetry A_1 and B_1 do not overlap when A_2 and B_2 are parallel. This suggest that the complexes align along different directions in different domains. However, the directions A_1, A_2 and B_1, B_2 are not aligned along any of the principal crystallographic directions of the substrate. In both domains, the complexes form highly oriented compact rows, which can be seen better in the zoom of the domain labelled 1, reported in Figure 4.3b.

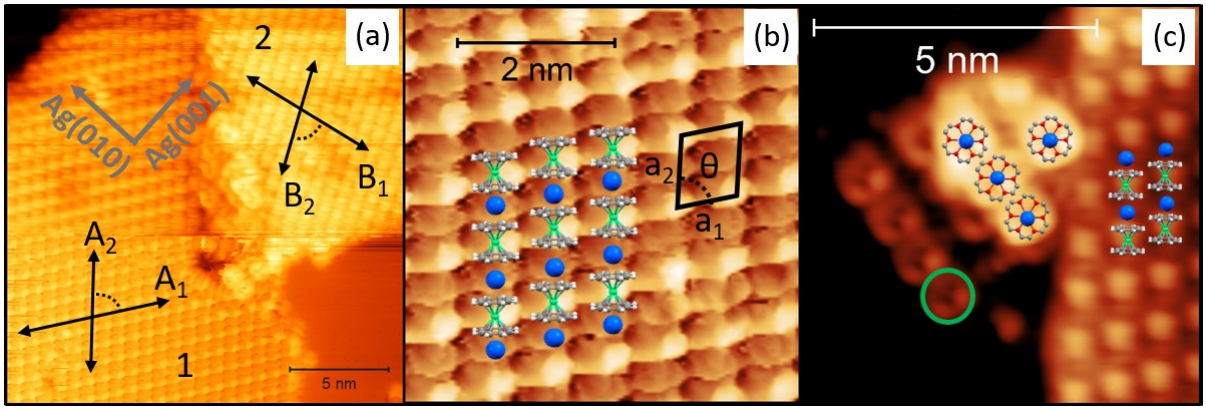

Figure 4.3. Constant-current STM images at 4.5 K of K[Er(COT)$_2$]/Ag(100). The imaging conditions are: (a) 50 pA, -2 V; (b) zoom of the panel (a); (c) 50 pA, -2 V. Overlays of the complexes, the domain orientation and the unit cell are shown, as explained in the text. Colors: green is Er, dark grey is C, blue is K and red is O. Adapted from ref. 82.

A repeating pattern of ovals with an approximate size of 0.44 nm × 0.74 nm exhibiting a rhombic assembly is unveiled in Figure 4.2b, with a brighter feature on every second oval along the direction A_2 of the domain (B_2 on domain 2). The size of such ovals is consistent with the one of the $[Er(COT)_2]^-$ anions lying-down on the substrate (~0.4 x 0.6 nm),[38] with the molecular axis parallel to the surface plane. We assume that the K^+ ions are coordinated between the anions to achieve charge balance, so that the alternating brighter and darker spots are due to the alternation of Er^{3+} and K^+ ions, separated by perpendicularly standing COT^{2-} rings. The overlay in Figure 4.3b shows this stacking of Er – COT – K – COT, which forms rows of densely packed K[Er(COT)$_2$] complexes, aligned along the same direction. A molecular density of 1.6 complexes/nm^2 is estimated from the images.

The unit cell of both domains (1 and 2) forms a rhombic shape with a_1 = 0.74 ± 0.05 nm, a_2 = 0.88 ± 0.04 nm and θ = 75°, reported in the Figure 4.3b. The comparison of these images to the one of bare Ag (as shown in Figure 4.2f) reveals that the complexes do not follow the fourfold symmetry direction of the substrate. However, a similarity in the packing structure in the different domains suggests that the surface could affect the self-assembly. Small agglomerates of round-shaped molecules are visible in Figure 4.3c with a diameter of 0.90 ± 0.05 nm (highlighted by a green circle) which is consistent with the size of (18-c-6) crown ether, part of the precursor complex.

4.1.3 Linearly polarized X-ray absorption spectroscopy

Linearly polarized experimental and simulated XAS and XLD spectra recorded for coverages of 0.5 MLs and 4 ML of Cp*ErCOT/Ag(100) are reported in Figure 4.4. The measurements were performed at the Er $M_{4,5}$–edges at 3 K and the samples were oriented with the substrate's normal parallel and at a grazing angle of 60° with respect to the X-ray beam. The applied magnetic field was always collinear with the X-ray beam. The spectra in this and the following Section are compared to simulation implemented by the multiX method, explained in Section 2.1.5. To adjust the multiX fitting parameters to the experimental spectra, the Coulomb interaction is scaled to have 85% of the computed values by the code, while the spin-orbit is scaled at 95%. A core-hole broadening is set from 0.45 to 1.45 eV in the span between 1398-1440 eV to simulate the peak width in the two M-edges. The ligand field is parametrized according to the reference system used to simulate the polarization direction, the incoming photon beam and the direction of the magnetic field. As explained in Chapter 2, the ligand field is imposed by the D_{8h} symmetry of the point charges for both complexes, taken with the main rotational axis parallel to the *z* direction of the reference system and based on the structure of COT ligand, as reported for $[K(18\text{-c-}6)][Er(COT)_2]\cdot 2THF$.[32] The nominal positions of the charges in the "standing-up" configuration are reported in Table 2.1, Section 2.1.5. The ligand field is scaled by a multiplication factor of 1.182. For each of the simulation set of spectra, the magnitude of the charges representing carbon atoms is manually changed in the range between 1 and 0.1 *e*, with *e* the (positive) elemental charge. By comparing the computed ground state with reference values reported by literature,[33,42] the best agreement was found for low charge values and a positive sign of the charges. This can be understood since the main electron density interacting with the Er 4f orbitals are the π clouds of the C atoms that form more or less two rings parallel to the COT ring plane but offset on both sides of the atomic coordinates. However, in the calculations the atomic coordinates are considered, rather than the position of the π cloud. This affects the exact value attributed to the charge in order to reproduce the real ligand field experienced by the lanthanide. As explained further below, in most cases the charge of the carbon atoms was fixed to 0.25 *e*, with the exclusion of the model for the $K[Er(COT)_2]$(0.5 ML)/Ag(100) sample, where the charge of atoms was set to 0.1 *e* for all the simulations of that sample, due to a better fitting of the spectra. The erbium was always assumed to be in the trivalent state. Control spectra showed different shapes of the $M_{4,5}$ edges for Er in other valence states, similar to the reported literature.[90]

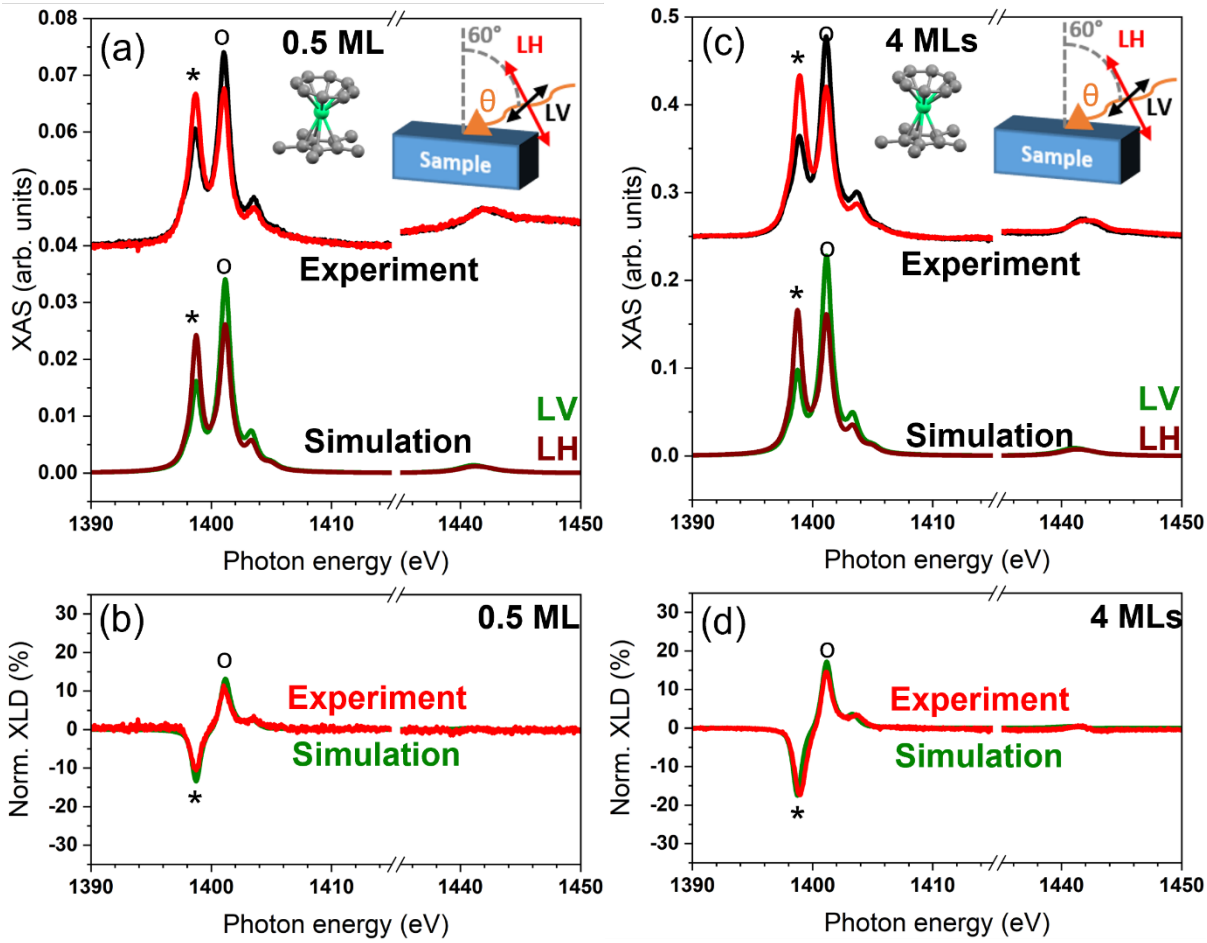

Figure 4.4. Linearly polarized XAS of the Er $M_{4,5}$-edge measured at 3 K and multiX simulated spectra of (a) 0.5 ML and (c) 4MLs Cp*ErCOT/Ag(100), while (b) and (d) show the experimental and simulated XLD of the two coverages, respectively. The insets show the complex and the experimental geometry of the grazing-angle incidence, along with the polarizations LH and LV and the incoming direction of photons. * and ° identify the main spectral features, as described in the text. Adapted from ref. 82.

Figure 4.4a shows that the absorption intensity for the two peaks identified as * (1398.8 eV) and ° (1401.1 eV) in the out-of-plane direction of the substrate (LH, red curve) is similar, while the in-plane polarized absorption (LV, black curve) is more intense in the ° peak. The performed simulations show that it is possible to tune the intensity of the * and ° peaks by using a model of the Cp*ErCOT complexes mixed in two configurations, standing-up and lying-down (see also Section 2.1.5). To reproduce the results, the spectra are simulated by assuming an equal amount of complexes in these two configurations and, in the case of the lying-down configuration, the main molecular axis is taken parallel to the substrate plane with uniform disorder over all azimuthal angles. The latter is based on the results of the STM analysis, where domains with different orientations were found. Manual adjustment of the point-charge values of the C atoms placed in a D_{8h} symmetry, representing the model of the complex, yielding the best agreement between the simulations and the experimental XLD/XMCD spectra when fixing the value to +0.25 *e*, used for all the Cp*ErCOT spectra.

Figure 4.4b shows the comparison of the experimental and simulated XLD, with the intensities reported in Table 4.1 (the XLD is expressed in percentage of the ° peak intensity, the error is given by different background subtraction methods). The good agreement of the XLD shape suggests that the negative sign of * and the positive sign of ° are characteristic of a configuration of the complex standing-up and lying-down on the surface, while the well reproduced intensities of the peaks suggest that the ratio is very close to be 50:50.

The larger coverage sample in Figure 4.4c shows that the shape of the XAS is similar to the sub-monolayer case, while the intensities of the * and ° peaks change. To simulate this variation, a model with 55% of the complexes with their axes pointing out-of-plane was used, which shows a very good agreement with the experimental data. In particular, the simulated XLD reported in Figure 4.4d and the peak intensities in Table 4.1 show an exceptional agreement with the experimental one.

Table 4.1. XLD intensities of * (~1398.5 eV) and ° (~1401 eV) peaks of experimental and simulated spectra (multiX) of Cp*ErCOT/Ag(100) and K[Er(COT)$_2$]/Ag(100), as reported in Figures 4.4 and 4.5. Adapted from ref. 82.

Cp*ErCOT	XLD * (%)		XLD ° (%)	
	Experiment	multiX	Experiment	multiX
0.5 ML	-11 ± 2	-13.4	11 ± 2	13.1
4 MLs	-17 ± 3.5	-17.5	15 ± 3	17.2
K[Er(COT)$_2$]				
0.5 ML	21 ± 4	25.5	-13 ± 3	-25.1
2 MLs	30 ± 6	25.8	-21 ± 4	-25.2

The K[Er(COT)$_2$](0.5 ML)/Ag(100) complex shows a similar absorption intensity for both * (1398.3 eV) and ° (1400.6 eV) peaks in the substrate plane (black curve), as reported in Figure 4.5a. In the out-of-plane direction there is a strong absorption asymmetry (red curve), with the main contribution coming from the ° peak. Based on the multiX simulations, this result is reproduced when all the complexes are assumed with the main axis parallel to the substrate plane, in the lying-down configuration. This is shown by the XAS and XLD reported in Figure 4.5a and 4.5b. To reproduce the XLD and the XMCD data (see next section) of the sub-monolayer sample, the fit was performed by fixing the value of the charges of the carbon atoms to 0.1 *e*, instead of 0.25 *e* (only in the case of this sample). The change of this parameter rather than assuming part of the compound in a different configuration has proved to reproduce better the experimental results, although experimentally standing-up complexes were detected on the surface (see previous section). In particular, the positive * and negative ° XLD peaks

are attributed to the configuration of the complexes (almost) fully lying-down, as opposed to the results of Cp*ErCOT/Ag(100).

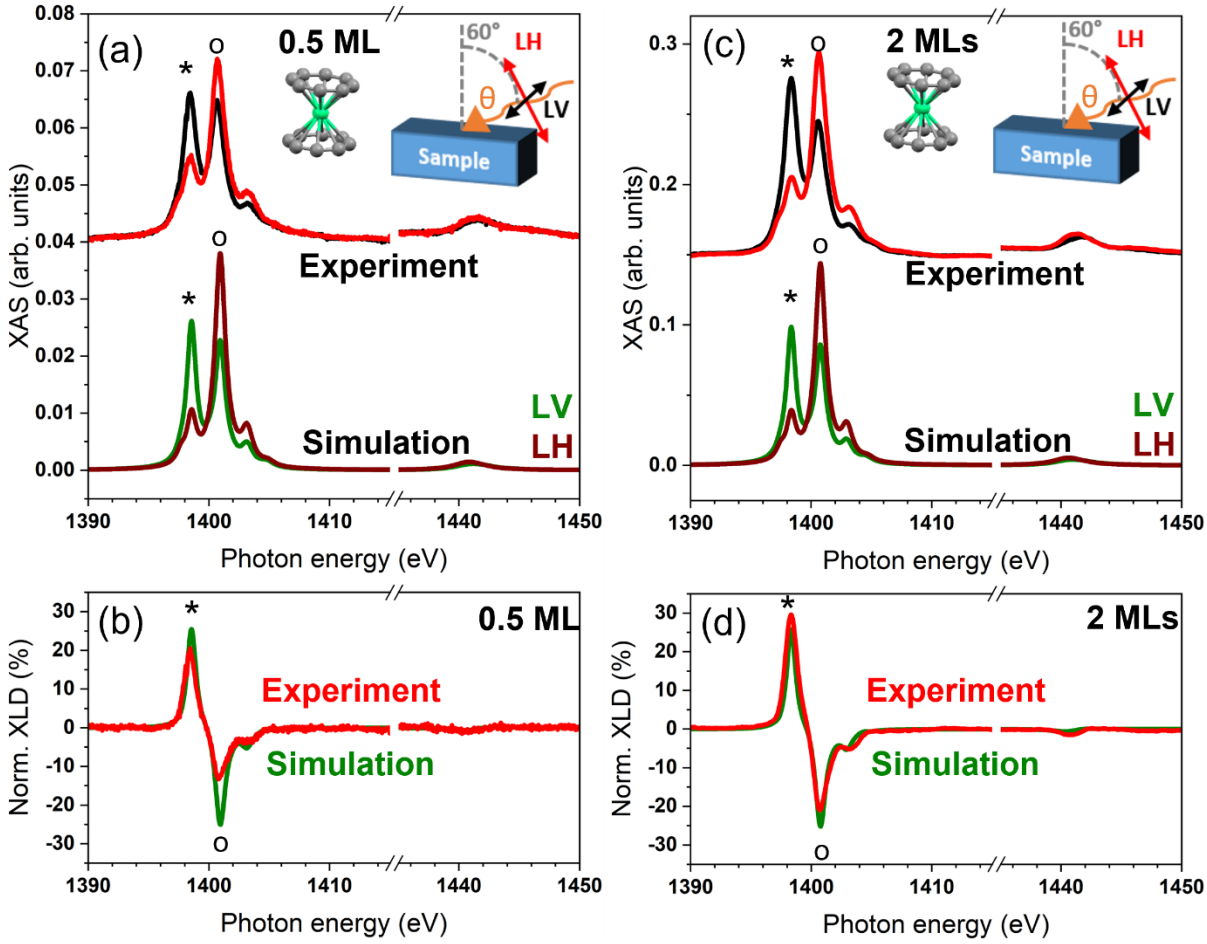

Figure 4.5. Linearly polarized XAS of the Er $M_{4,5}$-edge measured at 3 K and simulated (multiX) spectra of (a) 0.5 ML and (c) 2MLs $K[Er(COT)_2]$/Ag(100), while (b) and (d) show the experimental and simulated XLD of the two coverages, respectively. The insets show the $[Er(COT)_2]^-$ anion and the experimental geometry of the grazing-angle incidence, along with the polarizations LH and LV and the incoming direction of photons. * and ° identify the main spectral features, described in the text. Adapted from ref. 82.

The XAS and XLD spectra of $K[Er(COT)_2]$(2 MLs)/Ag(100) sample show the same trend of the sub-monolayer, with the intensities reported in Table 3.1. In this case, the simulation reproduces better the experimental result when fixing the charge of the carbon atoms to 0.25 *e*.

4.1.4 Circularly polarized X-ray absorption spectroscopy

The strong magnetic anisotropy of the individual complexes can also be used to retrieve information about the surface ordering by directly comparing XMCD intensities in normal and grazing incidence. The results are further supported by the multiX simulations, using the same model explained in the previous section.

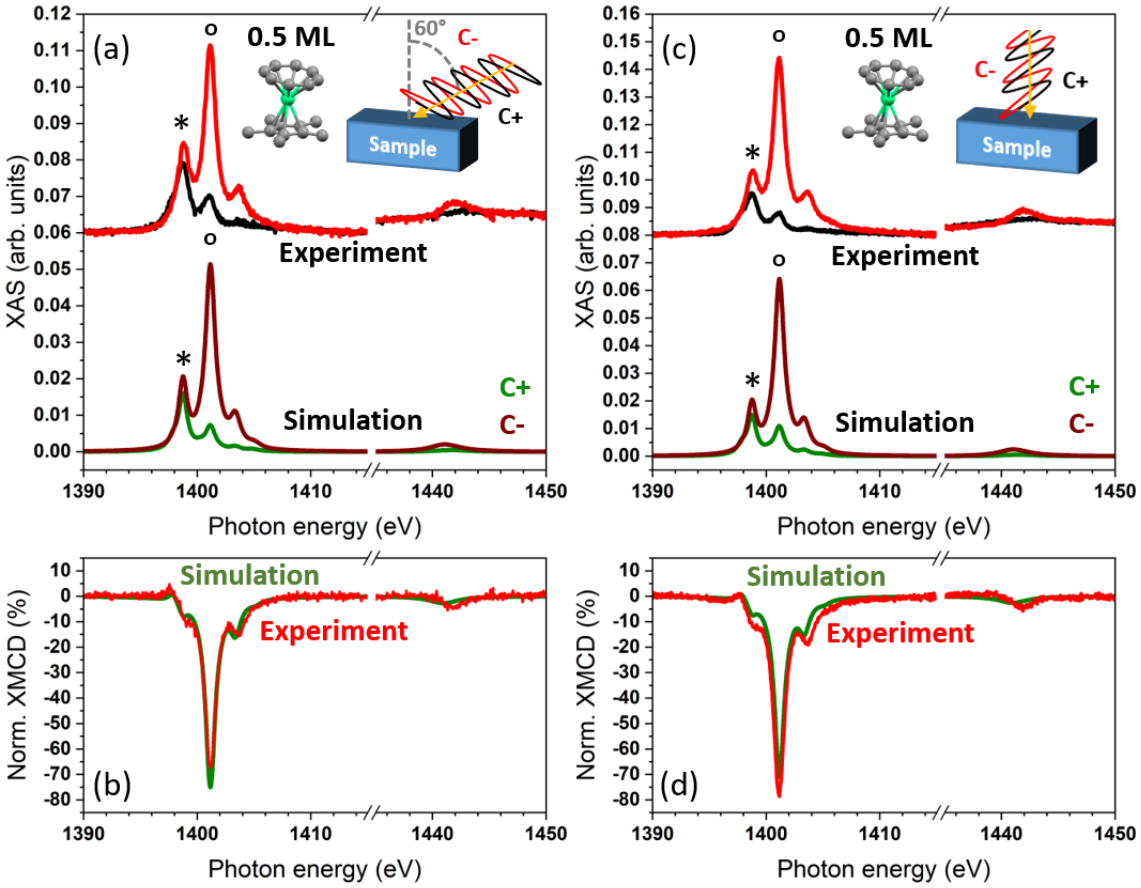

Figure 4.6. Circularly polarized XAS at the Er $M_{4,5}$-edge measured at 3 K and simulated (multiX) spectra of Cp*ErCOT (0.5 ML)/Ag(100). The insets show the experimental (a) grazing and (c) normal photon incidence. A magnetic field of 6.8 T was applied along the beam direction. (b,d) show the experimental and simulated XMCD spectra. Adapted from ref. 82.

Figure 4.6 shows circularly polarized XAS and XMCD spectra recorded on Cp*ErCOT (0.5 MLs)/Ag(100) in the two experimental configurations (see inset), revealing the typical shape of the trivalent Er $M_{4,5}$-edges.[90,91] By performing the simulations using the previously explained model with the 50:50 standing-up vs lying-down ratio for the self-assembled complexes and the charges of the carbon atoms fixed at 0.25 *e*, the obtained XAS reproduces well the experimental results in the Figure. The XMCD spectra in Figure 4.6b and 4.6d are also well reproduced, with the intensities of the strongest (negative) peak at 1401.2 eV reported in Table 4.2 (the XMCD is expressed in percentage of the ° peak

intensity, the error is given by different background subtraction methods). When the coverage of the surface is increased up to 4 MLs, the shape of the XAS and XMCD spectra reported in Figure 4.7 remains unaltered, although the intensities change. The best fit of the spectra is obtained with the 55:45 standing-up vs lying-down arrangement described in the XLD section, with the experimental and simulated XMCD intensities reported in Table 4.2.

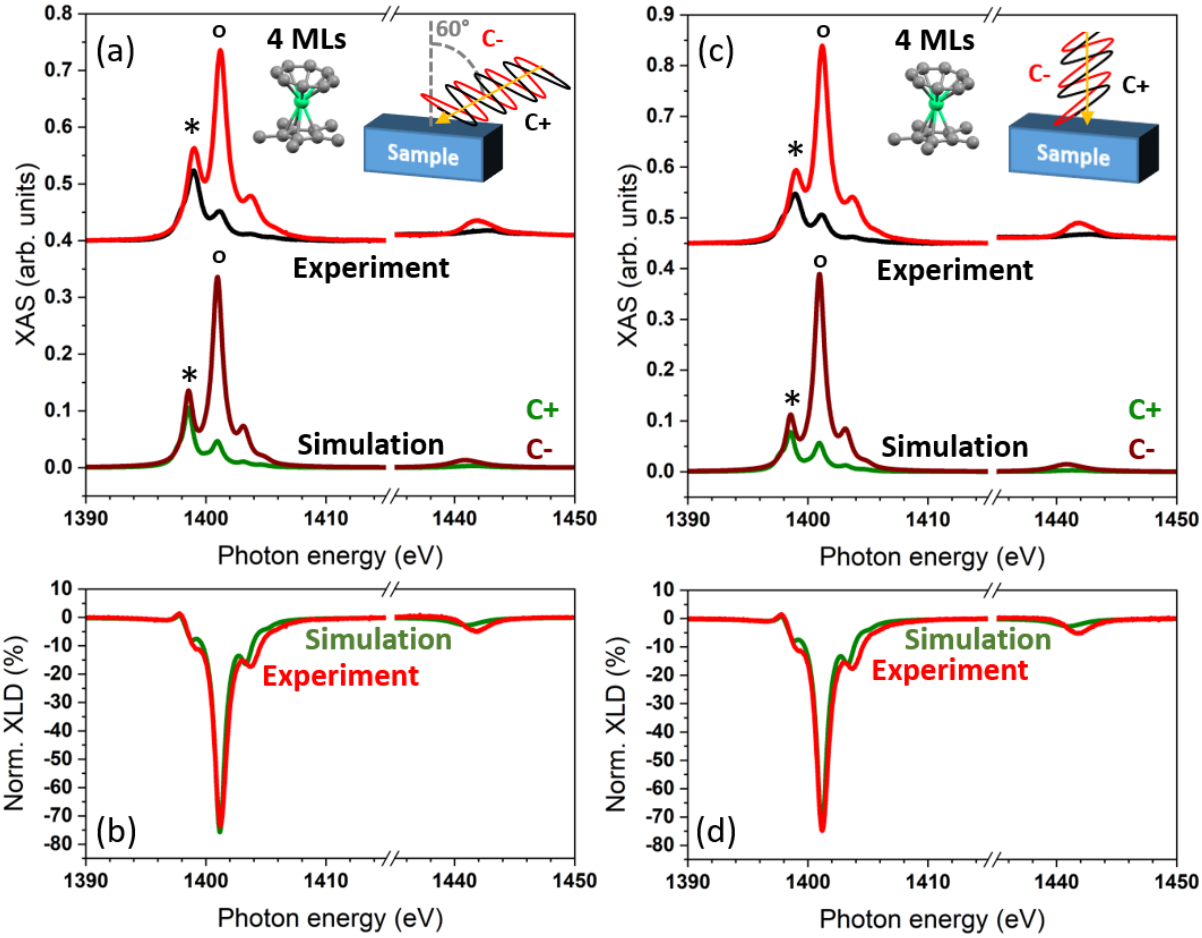

Figure 4.7. Circularly polarized XAS at the Er $M_{4,5}$-edge measured at 3 K and simulated (multiX) spectra of Cp*ErCOT (4 MLs)/Ag(100). The insets show the experimental (a) grazing and (c) normal photon incidence. A magnetic field of 6.8 T was applied along the beam direction. (b, d) show the experimental and simulated XMCD spectra. Adapted from ref. 82.

Circularly polarized spectra recorded on 0.5 MLs K[Er$(COT)_2$]/Ag(100) shown in Figure 4.8 display a strong difference between grazing and normal incidence of the X-rays on the sample. While the ° peak of the C- polarization has the highest intensity in both experimental configurations, in normal incidence the intensity decreases, if compared to the C+ polarization. The XMCD spectra have a similar shape in both configurations although the intensities are different, as reported in Table 4.2. The results are compared to simulations based on the model with all the complexes self-assembled in the lying-

down configuration, isotropically oriented over the azimuthal angle of the surface. As described in the previous section, the best fit is achieved by fixing the charges of the carbon atoms to 0.1 *e*.

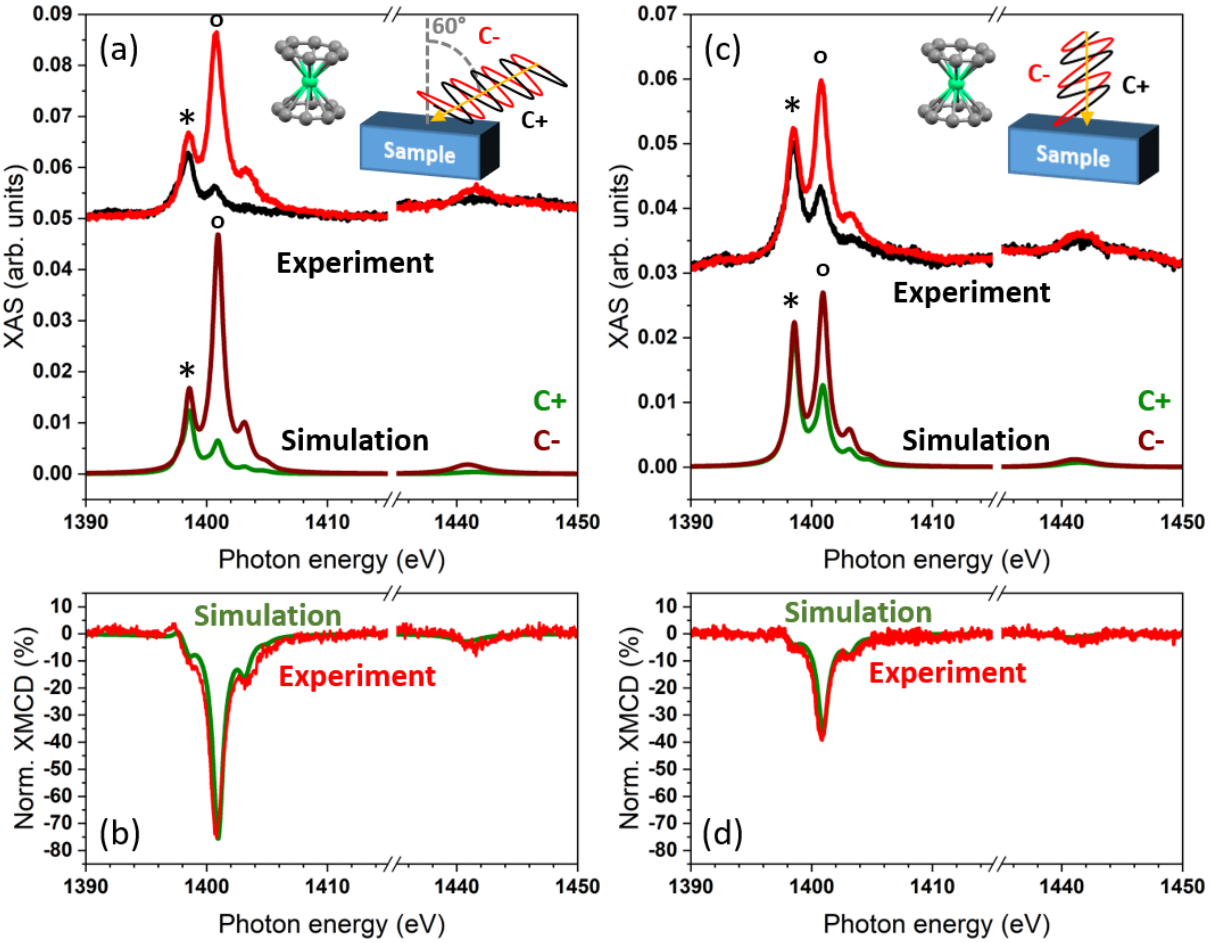

Figure 4.8. Circularly polarized XAS of the Er $M_{4,5}$-edge measured at 3 K and simulated (multiX) spectra of K[Er(COT)$_2$](0.5 ML)/Ag(100). The insets show the experimental (a) grazing and (c) normal photon incidence. A magnetic field of 6.8 T was applied along the beam direction. (b, d) show the experimental and simulated XMCD spectra. Adapted from ref. 82.

Increasing the coverage to 2 MLs affects the shape of the XAS in normal incidence, shown in Figure 4.9, where the intensity of * peak becomes larger than the ° peak, as opposed to the sub-ML sample. This is also reflected in the drastically smaller XMCD value in normal incidence, as shown in Table 3.2. The reduction of the intensities of the ° peak and the XMCD maximum in normal incidence is reproduced by the simulations when the charge of the carbon atoms is fixed to the value of 0.1 *e*, while keeping all other parameters unchanged.

The fact that a less positive charge of the carbon atoms reproduces better the experimental spectra in the sub-ML case points to the fact that the effective charge of the COT rings, as perceived by the central erbium ion, is more negative, as addressed in the discussion section.

Table 4.2. Experimental and simulated relative XMCD intensities at ~1401 eV of Cp*ErCOT/Ag(100) and K[Er(COT)$_2$]/(100) spectra reported in Figure 4.6, 4.7, 4.8 and 4.9. Adapted from [82].

Cp*ErCOT	XMCD normal (%)		XMCD grazing (%)	
	Experiment	multiX	Experiment	multiX
0.5 ML	87 ± 9	71.0	65 ± 7	75.0
4 MLs	74 ± 7	74.6	75 ± 8	75.6
K[Er(COT)$_2$]				
0.5 ML	39 ± 4	36.1	75 ± 8	75.6
2 MLs	16 ± 2	16.4	73 ± 7	68.0

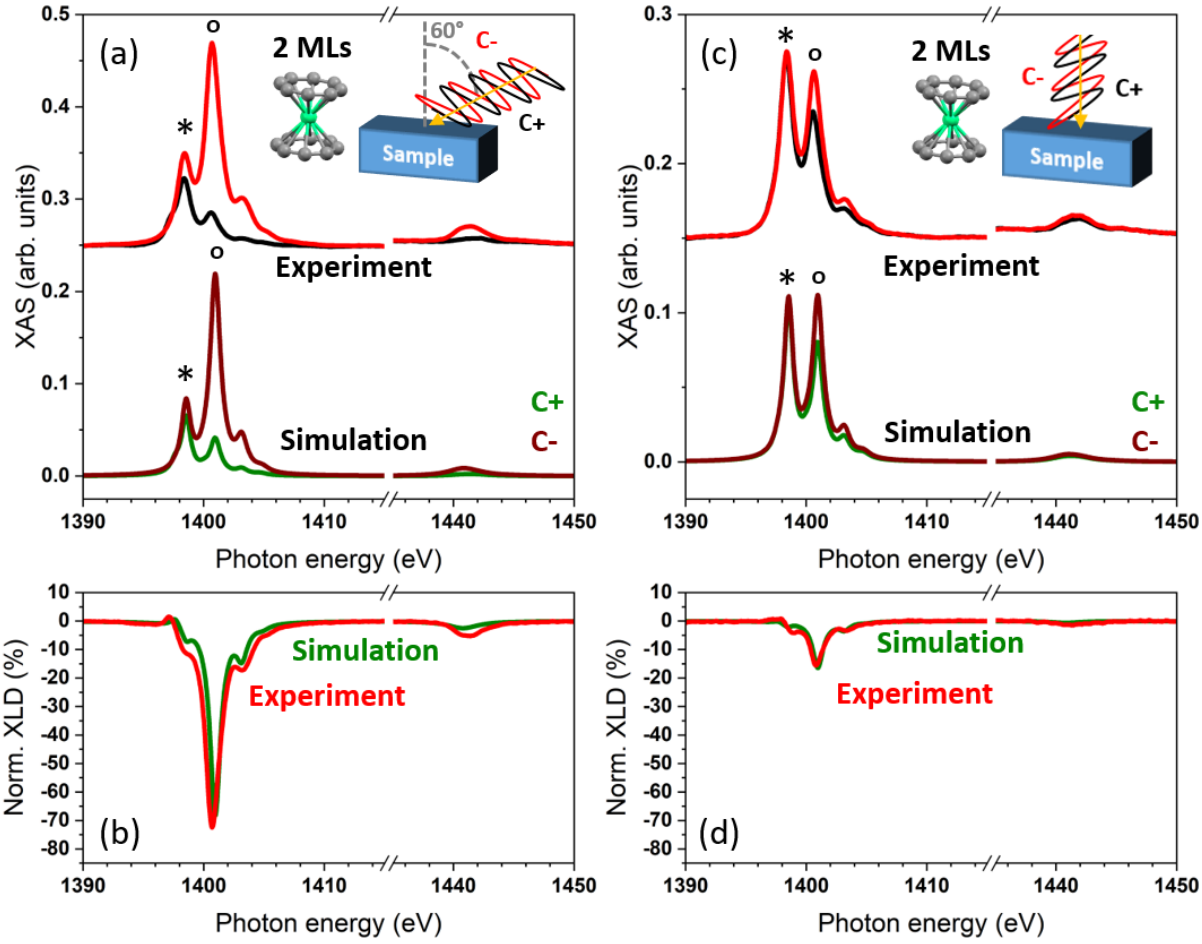

Figure 4.9. Circularly polarized XAS at the Er $M_{4,5}$-edge measured at 3 K and simulated (multiX) spectra of K[Er(COT)$_2$](2 MLs)/Ag(100). The insets show the experimental (a) grazing and (c) normal photon incidence. A magnetic field of 6.8 T was applied along the beam direction. (b, d) show the experimental and simulated XMCD spectra. Adapted from ref. 82.

Sum rule analysis[61,62] of the XMCD spectra was performed to extracted the values of the magnetic moments per Er atom of both organometallic complexes on Ag(100). The results are reported in

Table 4.3 and Table 4.4 for Cp*ErCOT/Ag(100) and K[Er(COT)$_2$]/Ag(100), respectively. In order to determine the <S_Z> values from <S_{Zeff}> we assumed that the value of the magnetic dipole moment <*T*z> scales proportionally to the variation of <S_{Zeff}>. In particular, when the molecular easy-axis is parallel to the magnetic field and the incoming photons the magnitude has its maximum value, corresponding to that of the free Er^{3+} ion.[92] From the expectation values, the magnetic moment m_S, the orbital moment m_L and total magnetic moment m_B are obtained in normal and grazing incidence (as explained in Section 2.1.4). For the Cp*ErCOT (0.5 ML)/Ag(100), the total magnetic moment in normal incidence is about half of the expected value for the pristine precursor, justified by the model used, where only half of the compound have the magnetic easy-axis aligned with the field. The values in normal incidence are well reproduced by the simulations, but the experimental moments in grazing incidence are smaller than the values obtained by the multiX method. In principle, the magnetic moment in grazing incidence is expected to be smaller than in normal incidence because it is an angle-dependent projection along the beam direction. However, the discrepancies between the experimental and simulated values can be ascribed to several effects, including an anisotropic ordering of the complex in the substrate plane, as well as defects in form of standing-up complex, as seen in the STM images. Since changing the point charges of the carbon atoms or the standing-up vs lying-down ratio of the compound worsen the agreement of the simulations with the experimental spectra, we assume other parameters are relevant. Similar conclusions can be drawn for the 4 MLs sample, where the experimental value of the magnetic moment in grazing incidence increases. In this case, the model in which 55% of the complexes are standing-up reproduces the data, within the estimated uncertainty.

Table 4.3. Orbital, spin and total magnetic moment values extracted from the sum rule analysis of experimental and simulated spectra of Cp*ErCOT/Ag(100) reported in Figures 4.6 and 4.7. Adapted from ref. 82.

0.5 ML Cp*ErCOT	Normal (μ_B)		Grazing (μ_B)	
	Experiment	multiX	Experiment	multiX
m_L	3.2 ± 0.8	3.3	2.4 ± 0.6	3.2
m_S	0.9 ± 0.2	0.8	0.4 ± 0.1	0.8
m_B	5.0 ± 1.0	4.9	3.3 ± 0.7	4.7
4 MLs Cp*ErCOT	Normal (μ_B)		Grazing (μ_B)	
	Experiment	multiX	Experiment	multiX
m_L	3.3 ± 0.8	3.5	2.9 ± 0.7	3.2
m_S	0.8 ± 0.2	0.9	0.7 ± 0.1	0.8
m_B	4.9 ± 0.9	5.3	4.3 ± 0.9	4.7

For the K[Er(COT)$_2$](0.5 ML)/Ag(100) the total magnetic moment of 4.5 ± 0.8 μ_B in grazing against the 1.9 ± 0.8 μ_B in normal incidence fits the anisotropy of the net magnetization suggested by the (mostly) in-plane ordering of the complexes. The extracted m_L, m_S and m_B values reported in Table 4.4 are in good agreement with the values given by multiX. This suggests that the model based on the D_{8h} symmetry with the charge of the carbon atoms fixed at 0.1 *e* for the sub-ML and 0.25 e for the multilayer fits well with the experiments, which justifies the choice of the fitting parameters explained in the previous section.

Table 4.4. Orbital, spin and total magnetic moment values extracted from the sum rule analysis of experimental and simulated spectra of K[Er(COT)$_2$]/Ag(100) reported in Figures 4.8 and 4.9. Adapted from ref. 82.

0.5 ML K[Er(COT)$_2$]	Normal (μ_B)		Grazing (μ_B)	
	Experiment	multiX	Experiment	multiX
m_L	1.2 ± 0.5	1.2	3.1 ± 0.7	3.4
m_S	0.4 ± 0.3	0.3	0.7 ± 0.1	0.8
m_B	1.9 ± 0.8	1.8	4.5 ± 0.8	5.0
2ML K[Er(COT)$_2$]	Normal (μ_B)		Grazing (μ_B)	
	Experiment	multiX	Experiment	multiX
m_L	0.5 ± 0.2	0.5	3.4 ± 0.5	3.0
m_S	0.08 ± 0.03	0.1	0.7 ± 0.1	0.7
m_B	0.7 ± 0.3	0.8	4.9 ± 0.6	4.4

4.1.5 Field-dependent magnetic circular dichroism

The magnetic hysteresis loops were measured as the variation of the XMCD intensity while sweeping the external magnetic field at 3 K and the values are rescaled according to the magnetic moments extracted from sum rules analysis of the previous section. Hysteresis loops were recorded as the intensity difference between the absorption at the energy of maximum XMCD (~1401 eV) and the pre-edge showing no XMCD, while sweeping the magnetic field between ±6.8 T at 2 T min^{-1} rate. The curves are rescaled to the total magnetic moments extracted by the sum rule analysis and displayed between ±4 T, to better visualize the openings. The results are shown between ± 4 T, to better visualize the loop openings. An average photon flux used to measure the *M*(*H*) curves of the Cp*ErCOT samples amounts to 2.0×10^{-2} photons nm^{-2} s^{-1}, while the maximum flux used for K[Er(COT)$_2$] is 5.0×10^{-2} photons nm^{-2} s^{-1}.

Figure 4.10a shows the magnetic hysteresis loops of Cp*ErCOT (0.5 ML)/Ag(100), where a small hysteresis opening is visible for both normal and grazing angles. Upon increasing the coverage to 4 MLs, the hysteresis loops display the same behavior, with the saturation values at 6.8 T reported in

Table 4.3. Since the bulk Cp*ErCOT shows a substantial butterfly-like hysteresis opening at 3 K,[93] the reduction of the hysteresis opening of the surface adsorbed Cp*ErCOT can be attributed to the interaction with the substrate, addressed further.

Figure 4.10b shows that K[Er(COT)$_2$] (0.5 ML)/Ag(100) exhibits a large butterfly-like hysteresis opening between ±3.5 T in grazing incidence, while the loop is essentially closed in normal incidence. This is in agreement with the orientation of the net easy-axis of the magnetization of the sample mostly parallel to the substrate plane. For the 2 MLs sample, the hysteresis shows a very similar opening in grazing, but with larger openings in high field regions when increasing the field toward ±4 T. For both coverages, the coercive field was estimated at 0.15 ± 0.07 T, while the remnant magnetization as 0.84 ± 0.06 μ_B. The fact that the hysteresis loop of the 2 MLs sample shows a larger loop opening indicates that the multilayer sample has greater magnetic stability.

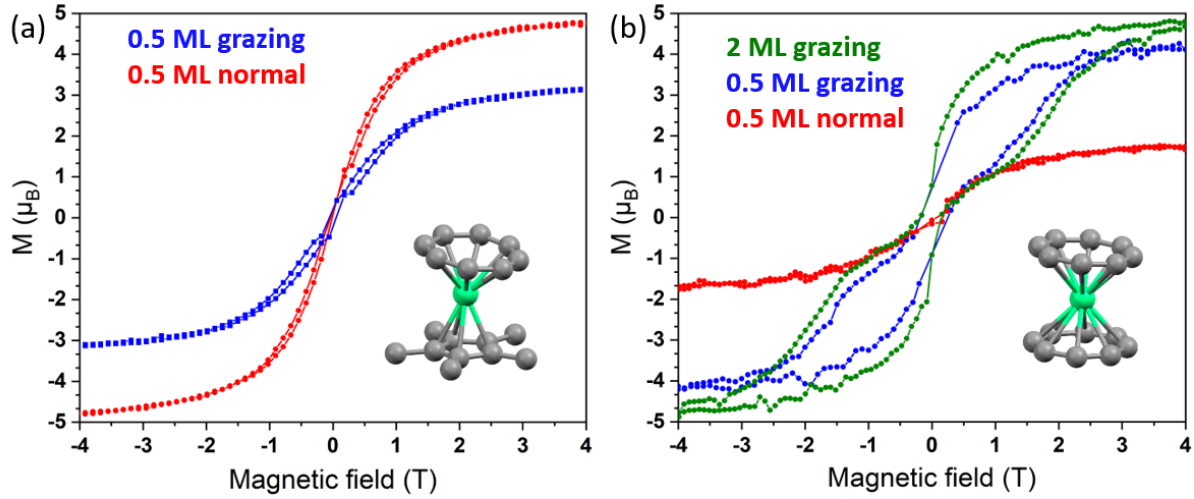

Figure 4.10. XMCD-detected magnetic hysteresis loops recorded at 3 K of (a) K[Er(COT)$_2$] and (b) Cp*ErCOT adsorbed on Ag(100), at a field sweep rate of 2 T min^{-1}. Normal and grazing (60°) indicate the photon incidence on the sample. Magnetic moments values are extracted by sum rule analysis. Lines connecting experimental points are guides to the eyes. Adapted from ref. 82.

4.1.6 Discussion: monolayers of ErCOT-based SMMs

Cp*ErCOT and K[Er(COT)$_2$] in the sub-ML to ML range show a completely different self-assembled ordering on Ag(100). To understand the orientation of the complexes the main rotational axis passing through the centers of the ligands can be used. In particular, the Cp*ErCOT forms domains of alternating rows of standing-up and lying-down complexes, as shown by STM and XAS/XLD/XMCD measurements. A mixed standing-up and lying-down ordering of π-conjugated SMMs was first reported for metallocenes on metal substrates, where such a configuration is dictated by the T-shaped

Van der Waals interaction between the Cp ligands of neighboring molecules.[41,88] The presence of lying-down nickelocene was shown to be necessary to minimize the adsorption energy of the organometallic compound on metals,[41] and it is likely the same reason driving the ordering of Cp*ErCOT. The main difference compared to the self-assembly of metallocenes is that the lying-down Cp*ErCOT complexes connect "diagonally" the standing-up complexes of neighboring rows rather than perpendicularly, reproducing the ordering formed along the [-101] direction in the Cp*ErCOT crystal. Also, the orientation of lying-down rows changes between consecutive rows, forming a herringbone-like pattern, shown in Figure 4.2a and 4.2c. The herringbone structure is found also in the compact configuration of metallocenes, caused by the lateral shift of 0.15 nm by standing-up complexes belonging to every second row, which is also shown by Cp*ErCOT.[88] This likely happens so that the complexes can accommodate in the energetically favorable adsorption sites on the surface, while still being influenced by the intermolecular interaction. On the other hand, heteroleptic sandwich organometallic compounds can depart from this ordering, as recently reported for CpTiCOT/Au(111).[85] In the latter case, the compound forms a complex unit cell of mixed standing-up and lying-down configuration in a 1:3 ratio, due to stronger inter-molecular interactions. In the present case, STM and XLD measurements suggest that the ratio of Cp*ErCOT in the two configurations is close to 1:1, especially in the sub-ML case. Deviations can be attributed to the alignment of the axis of lying-down complexes tilted out-of-plane by few degrees, due to the different size of the COT and Cp* ring, as illustrated in Figure 4.11a. Defect rows of the compound are disclosed by STM images in Figure 4.2a and 4.2d, which can also contribute to deviations from the 1:1 ratio of the configuration of the complexes. On the other hand, the model used by the multiX code to simulate the XAS is very simple and based on the highly symmetric D_{8h} symmetry of the point charges for both compounds, but is able to reproduce the experimental XLD and XMCD trends with great fidelity. Most importantly, it points out that the difference in the XLD shape of the two complexes is given by their different self-assembly. In fact, the $K[Er(COT)_2]$ SMMs form domains constituted by highly oriented rows with the complexes in the lying-down adsorption conformation, with the main axes aligned in rows. Such a conformation suggests that the $[Er(COT)_2]^-$ anions are conjugated through the intercalation of K^+ ions, in a similar manner to the structure reported for the $K(THF)_4[Er_2COT_4]$ tetralayer.[34] As a matter of fact, the measured distance between two $K[Er(COT)_2]$ complexes extracted from STM images amounts to 0.88 ± 0.04 nm (a_2 in Figure 4.3b), exactly the Er-Er distance in the $K(THF)_4[Er_2COT_4]$ complex. In different words, the STM images suggest that $K[Er(COT)_2]$ forms rows of alternating Er^{3+} and K^+ ions spaced by standing COT^{2-} rings. A similar linear wire-like configuration of COT-based single-chain magnets on surfaces was reported for EuCOT/Graphene/Ir, with the COT^{2-} anionic rings perpendicular to the surface, arranged with Eu^{2+} ions in an alternating fashion.[89,94] For π-

conjugated systems, the expected preferential ordering would be with the rings parallel to the surface plane or driven by the T-shaped interaction discussed previously. However, given the ionic nature of $K[Er(COT)_2]$, it is not surprising that the charge balance via intercalation of a potassium ion between two anions is the main mechanism driving the self-assembly. The positioning of the K^+ in the first layer is likely being influenced by its charged nature or its smaller size compared to the anion, so that the cations adsorb closer to the surface, instead of being between the centers of two COT rings, as in the tetralayer.[34] In particular, we assume that the K^+ ions tend to adsorb closer to the substrate because of the charge compensation of the metal surface. While they are still positioned between the lying-down $[Er(COT)_2]^-$ anions, the K^+ ions adsorb at a closer distance to the surface in the first layer than in the top layers of a multilayer sample, where the K^+ finds stability between the two COT rings, possibly aligning with their rotational axis. In the sub-ML sample, the charge segregation forms a static electric dipole, with a layer of positive ions closer to the surface and layer of $[Er(COT)_2]^-$ anions. The charge separation in the sub-monolayer case forms an effective electric dipole that acts as a built-in potential on the surface, affecting the kinetic energy of the photoemitted electrons. This results in the shift of the positions of the measured XPS core levels towards lower binding energies (the shift depends on the polarity of the effective potential). The deposited thickness-dependent test samples (see Section 3.1.2) show a consistent shift of all core levels toward higher binding energies, similarly to the reported cases of other dipolar compounds.[95,96] The behavior reported in literature is thickness dependent. Indeed, the samples with larger coverages tend to recover the position of the core levels, which are more aligned with the data reported for C 1s,[83–85] K 2p[97,98] and Er 4d.[86,99] In particular, the binding energy of the C 1s peak of the test sample with the largest coverage (8 MLs) coincides with the carbon peak of the π rings of the Cp*ErCOT(1 ML)/Ag(100) sample. By increasing the thickness of the $K[Er(COT)_2]$ sample, the influence of the interface becomes less important on the potassium cations in the outer layers, so that the K^+ are more stably coordinated at the center of the COT rings, along the axis of the complexes. A model of this behavior is reported in Figure 4.11b. Such effect would explain the rather low C 1s binding energy of 283.9 eV of the sub-ML $K[Er(COT)_2]$ and the core level shifts reported in the Section 3.1.2, although we do not exclude the contribution of screening. Moreover, this behavior is also suggested by the XAS spectra of the sub-ML sample, since lower (higher) positive (negative) charges of the carbon atoms were used to simulate the ligand field of the sub-monolayer $K[Er(COT)_2]$ sample. A better fit of the spectra while using a charge of 0.1 e is a hint that in this sample the ligands have an effectively higher negative charge, which points again toward the interpretation of the charge separation explained previously. Nevertheless, we do not exclude that the surface-induced screening effect or the charge accumulation of the thicker test samples can contribute to the shifts of the peak positions as well.

On the other side, small shifts of core levels to lower binding energies for sub monolayer samples can also be attributed to screening of the core-hole performed by the image state electrons of metallic substrates. However, on metal surfaces such shift is usually not greater than ~0.6 eV,[100] leading to a broadening of the peak, with rather a tail toward the lower binding energy side. In case of fullerenes on Cu(111), the complex-substrate interaction promoted shifts up to ~0.7 eV for the C 1s peak in attributed to charger transfer[101], while on Au(100) the reported shift was -0.8 eV[102], similarly to other cases[100,103,104]. However, there is no clear indication of such phenomenon for K[Er(COT)$_2$]/Ag(100), since all the edges shift to higher binding energies with increasing coverage.

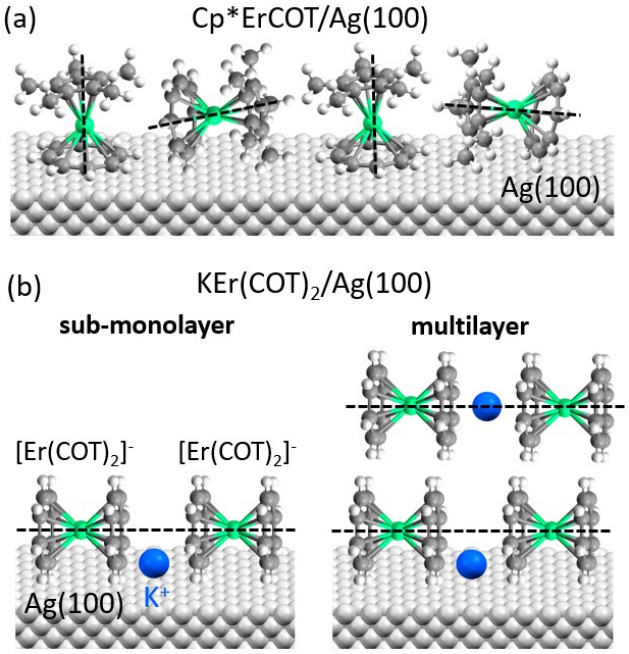

Figure 4.11. Model of self-assembled (a) Cp*ErCOT/Ag(100) and (b) K[Er(COT)$_2$]/Ag(100). The dashed lines represent the molecular axes of the complexes. Colors: green is Er, dark grey is C, light grey is Ag, blue is K, white is H. Adapted from ref. 82.

We also presume that Cp*ErCOT experiences a stronger interaction with the surface compared to K[Er(COT)$_2$] for two reasons: 1) the templating effect that the Ag(100) surface induces on the molecular self-assembly, which aligns along highly symmetric [010] and [001] directions of the substrate; and 2) the small opening of the hysteresis loops that the complexes show as compared to the bulk opening (see further below). While bulk Cp*ErCOT shows a wide hysteresis opening for the undiluted sample at 3 K, shown in Figure 4.12a,[38] our measurements show that the surface-supported complex displays a larger magnetization relaxation rate, considering the faster sweeping rate of the magnetic field used here. Also, on the Ag surface the small hysteresis opening is similar in the in-plane and out of plane directions, showing an overall weak net anisotropy, due to the mixed ordering of the

complexes. The stronger interaction of Cp*ErCOT with the substrate can be justified by the interaction of the π orbitals of the standing-up complex directly with the metal, which enhances the magnetization relaxation, in a similar way to previously reported cases.[19–24] The X-ray induced demagnetization has been estimated to be a small contribution to the closing of the M(H) curves, given the low photon flux, which was compared to the cases reported in literature.[26,105]

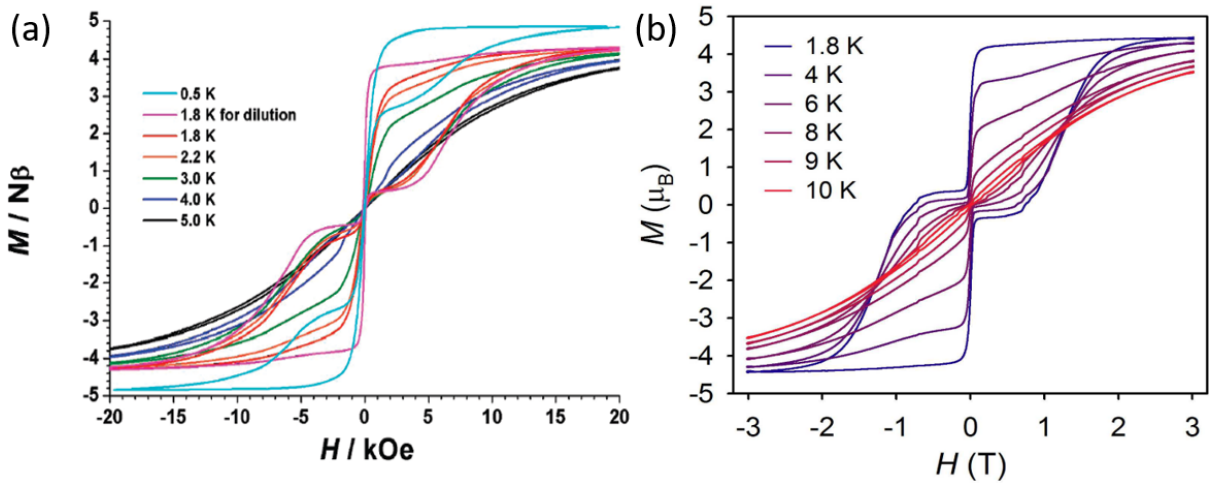

Figure 4.12. Magnetic hysteresis opening of bulk (a) Cp*ErCOT and (b) [K(18-c-6)][Er(COT)$_2$]·2THF as a function of temperature. The graphs are adapted from the original papers.[32,38]

Contrarily, the K[Er(COT)$_2$] SMMs show very strong net anisotropy due to the orientation of the complex with the net easy axis parallel to the substrate plane. The hysteresis opening is showing clearly a slow relaxation of the magnetization at the experimental conditions used, similar to the butterfly opening reported for the precursor [K(18-c-6)][Er(COT)$_2$]·2THF shown in Figure 4.12b.[32] Since the ramping speed of the measurements performed is different from the reported bulk compounds, a direct comparison of the loops is challenging. However, if compared to the hysteresis loop of the similar complex [K(18-c-6)][Er(COT)$_2$], reported in Figure 4.13a, [33] the hysteresis loop of K[Er(COT)$_2$] shows more similarities, as shown in Figure 4.13b. We presume that the THF act generally as a spacer between molecules, reducing the eventual Er-Er interaction, and it affects slightly the positions of the COT^{2-} ligands, as discussed in the original papers.[32,33] The small change in the ligand field can change the relaxation of the magnetization pathways in these complexes, as discussed in Chapter 1. In the case of K[Er(COT)$_2$], we presume that the relaxation type is similar to the bulk [K(18-c-6)][Er(COT)$_2$], attributed to the temperature-assisted quantum tunneling of magnetization process, mainly due to the similarities in the low field region of the curves.[33] We do not exclude that other mechanisms can also affect the hysteresis shape, like the X-ray induced demagnetization at low magnetic fields.

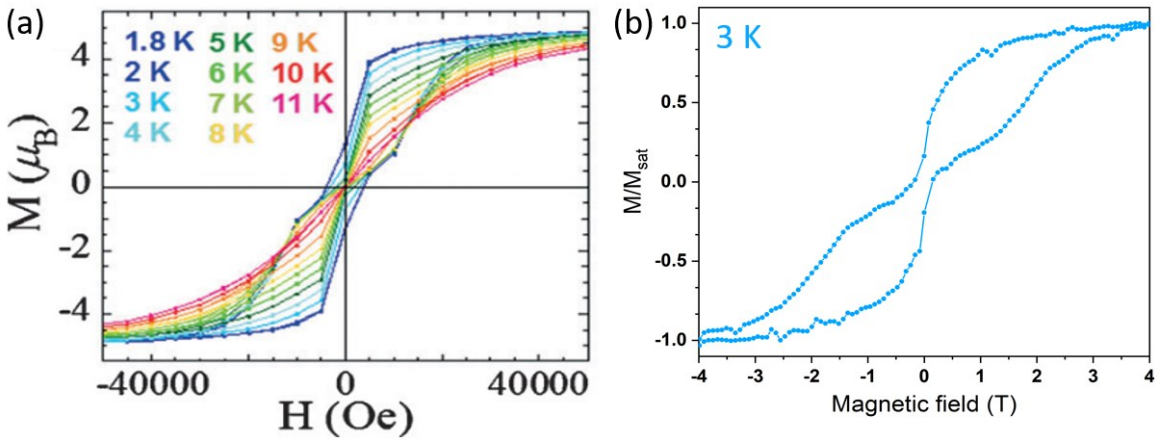

Figure 4.13. Magnetic hysteresis opening of (a) bulk [K(18-c-6)][Er(COT)$_2$] as a function of temperature and (b) 2 MLs K[Er(COT)$_2$]/Ag(100) at 3 K from Figure 4.10. The graph in (a) is adapted from the original paper.[33]

Although Cp*ErCOT and K[Er(COT)$_2$] show different hysteretic behavior, they both show slow relaxation of magnetization in the bulk. In the present study, the reason of the different hysteresis openings of the two complexes seems to be given by the orientation of the π orbitals with respect to the substrate, implying that the orientation of the self-assembly on the surface has an enormous impact on the magnetic properties. The direct interaction of the π orbitals of standing-up Cp*ErCOT SMMs with the substrate likely induces a faster magnetization relaxation rate, which explains why only a small opening of the hysteresis is detected. On the other hand, the ionic character of the K[Er(COT)$_2$] SMMs influences the ordering of the self-assembly such that the π orbitals are parallel to the surface plane, weakly interacting with the substrate, which preserves better the slow relaxation of magnetization.

4.2 Optical properties of single-molecule magnets

The results presented in this Section are based on a manuscript in preparation with co-authors: Moritz Bernhardt, Katie Harriman, Maciej Damian Korzyński, Harry Ramanantoanina, Guy Matmon, Christophe Copéret, Muralee Murugesu, Frithjof Nolting and Jan Dreiser.[106] The authors have contributed to the project as specified in the footnote.[2] The Figures, Tables and the text in this Section is partially adapted or fully reported from the manuscript to be published.[82]

4.2.1 Intra-4f transitions of Er(III)-based SMMs

Temperature-dependent Fourier-transform infrared (FTIR) spectroscopy is used to study four Er^{3+}-based SMMs, introduced in Chapter 1, to determine the main intra-4f transitions between the ground state manifold $^4I_{15/2}$ and the first excited manifold $^4I_{13/2}$ of the Er^{3+} ion. The absorbance of [K(18-crown-6)][Er(COT)$_2$]·2THF (also labelled as **1**),[32] [Li(DME)$_3$][Er(COT'')$_2$] (**2**),[37] Cp*ErCOT (**3**)[38] and Cp^{ttt}ErCOT (**4**)[39] at 3 K, normalized with the most intense transition to 1, is shown in Figure 4.14 (the labels in bold are used to avoid redundancy).

In this energy range, the homoleptic compound **1** displays one sharp peak around 6511.5 cm^{-1}, while compound **2** shows several peaks, with the strongest being around 6509.6 cm^{-1}. Similarly, the two heteroleptic compounds **3** and **4** show multiple transitions, with the strongest being at around 6560.4 cm^{-1} and 6556.7 cm^{-1}, respectively. As explained further below, many peaks of compounds **1**, **2** and **3** are broadened or split in two main contributions, with an example visible in Figure 4.14, where the strongest transition peak of Cp*ErCOT splits in two. By integrating the areas of the single/double peaks of the strongest transitions of the 4 complexes, the absorption cross sections can be estimated by using the relations introduced in Section 2.1.6 and the sample parameters described in Chapter 3. The results are reported in Table 4.5, where the uncertainty is estimated statistically from repeated measurements for each compound.

[2] M. Bernardt, M. D. Korzyński, C. Copéret have prepared the [K(18-c-6)][Er(COT)$_2$]·2THF, Cp*ErCOT, Cp^{ttt}ErCOT and Cp*YCOT complexes. K. Harriman and M. Muralee have prepared the [K(18-c-6)][Er(COT)$_2$]·2THF and [Li(DME)$_3$][Er(COT)$_2$] complexes. H. Ramanantoanina have performed LF-DFT simulations (not shown in the thesis). F. Nolting and J. Dreiser have contributed with the discussions regarding data analysis and paper preparation. J. Dreiser and V. Romankov have both contributed to the design of the experiments. V. Romankov has contributed with the execution of all the experiments presented in the current Section 4.2, the sample preparation, the data acquisition and analysis, as well as the preparation of the Figures and Tables. V. Romankov is also the first author of the paper in preparation, titled "Optical access to rotamer-split 4f levels of Er(III) cyclooctatetraenide-based single-molecule magnets".[106]

Table 4.5. Absorption cross sections of the strongest transitions (average in case of peak splitting) from the ground state manifold $^4I_{15/2}$ to the $^4I_{13/2}$ manifold of the studied Er(III) SMMs, extracted from FTIR spectra in Figure 4.14. Adapted from ref. 106.

Label	Compound	Average transition wavenumber (3 K)	Absorption cross section
1	$[K(18\text{-c-}6)][Er(COT)_2]\cdot 2THF$	6511.5 cm^{-1}	$2.6 \pm 1.2 \times 10^{-19}$ cm^2/complex
2	$[Li(DME)_3][Er(COT'')_2]$	6509.6 cm^{-1}	$2.0 \pm 0.9 \times 10^{-19}$ cm^2/complex
3	Cp*ErCOT	6560.4 cm^{-1}	$4.7 \pm 2.2 \times 10^{-19}$ cm^2/complex
4	Cp^{ttt}ErCOT	6556.7 cm^{-1}	$7.0 \pm 3.2 \times 10^{-19}$ cm^2/complex

While the two compounds based on the aromatic rings of 8 carbons (**1** and **2**) show different number of transition peaks in the energy range of the first Er^{3+} excited multiplet, the spectra of compounds **3** and **4** show multiple similarities. By looking closer at the strongest transition peaks of the latter two compounds at 3 K, reported in Figure 4.15a, the position of the single and sharp peak of compound **4** overlaps with the position of the lower-energy-lying peak of the main transition of compound **3**. In addition, the 6 less intense peaks on the higher energy side (6675 – 6850 cm^{-1}), reported in Figure 4.15b, can be divided into the first sharp 5 peak and the last broad 6th peak for both complexes. The position and the structure of those peaks, attributed to the intra 4f level transitions, reflect the similarities in the energy level scheme of the two compounds. However, the two complexes show also some major differences in this energy range. In particular, compound **3** shows a splitting of the most intense transition in two main contributions, distant 6.6 cm^{-1} apart, and additional features in between, as reported in Figure 4.15a. An asymmetric broadening of all remaining 6 peaks and a clear splitting of peak "2" into two features is also detected in Figure 4.15b. Moreover, compound **4** shows increasingly more intense peaks labelled in the Figure from "1" to "5", whereas compound **3** have no sequential ordering of the intensities for those peaks. As explained further below, the splitting and/or broadening of the transitions in two main contributions in compound **3** is attributed to the different conformers of this complex present in the crystal lattice. Figure 4.15 shows also an asymmetric shape of the strongest transition lines of compounds **3** and **4**, as well as compound **1** (partially visible in Figure 4.16a), which is associated to the Fano resonance, possibly due to the coupling of the electron transitions between discrete states with the phonon band of the complexes, known to produce similar effects.[107]

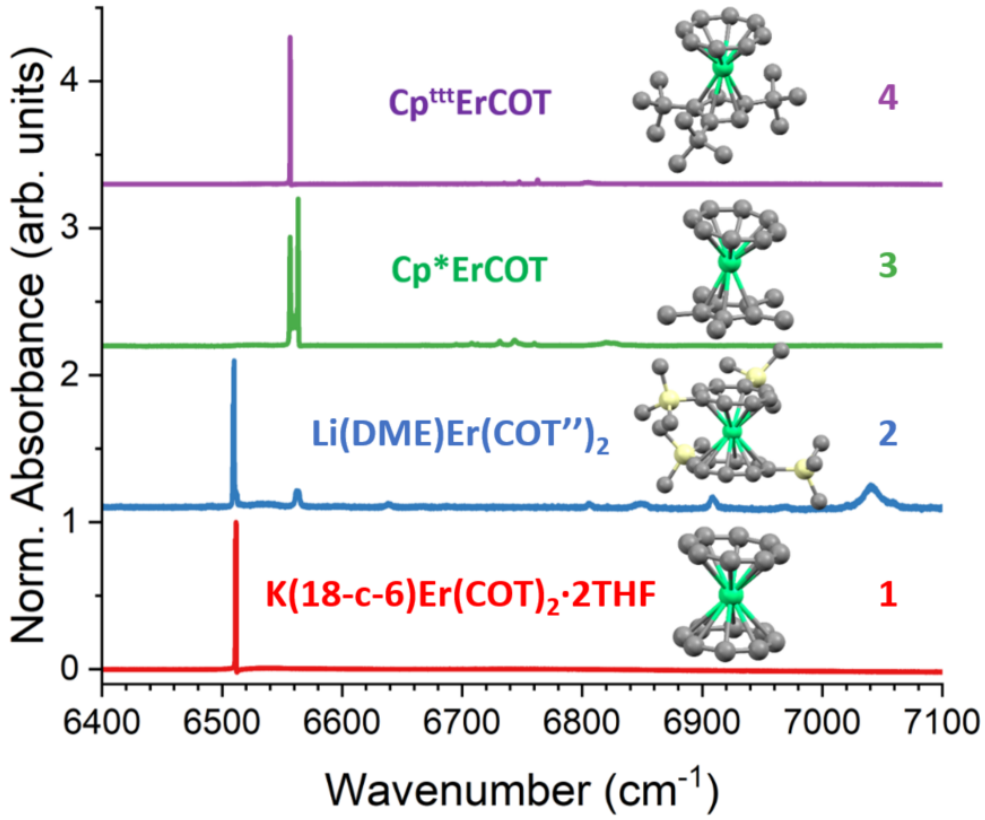

Figure 4.14. FTIR absorbance spectra at 3 K in the Er^{3+} $^4I_{15/2}$ to $^4I_{13/2}$ energy transition region of the four ErCOT-based SMMs. The spectra are normalized and vertically offset for clarity. The $[K(18\text{-c-}6)]^+$ and $[Li(DME)_3]^+$ counter-ions are omitted. Adapted from ref. 106.

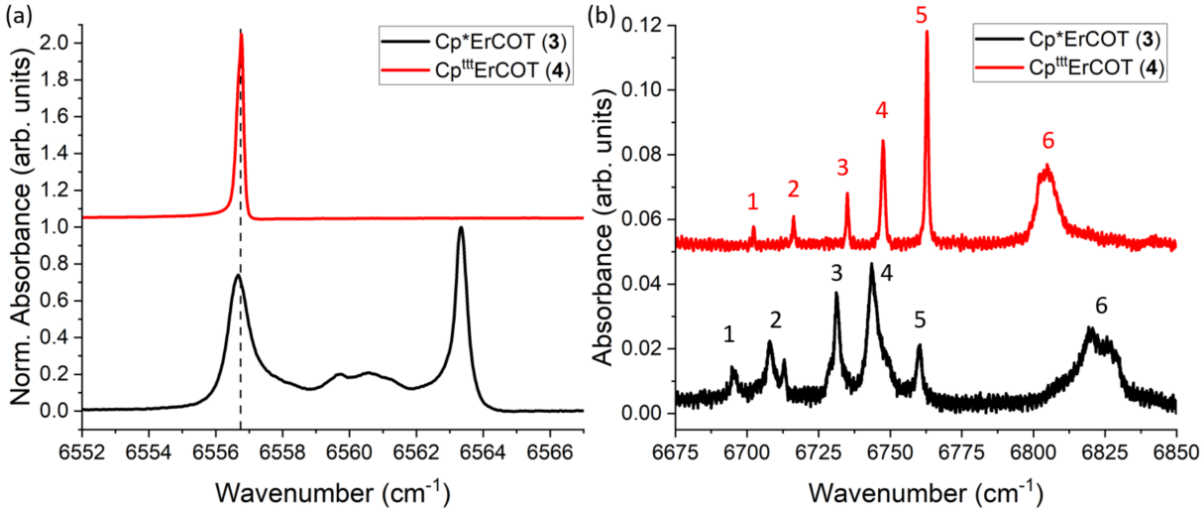

Figure 4.15. (a) Zoom on the most intense intra-4f spectral peaks at 3 K in the Er^{3+} $^4I_{15/2}$ to $^4I_{13/2}$ energy transition region of Cp*ErCOT and Cp^{ttt}ErCOT, normalized with the strongest peak to unity. (b) Zoom on the remaining less intense intra-4f absorption peaks of the compounds, normalized to the background baseline. All the spectra are vertically offset for clarity and the peaks in (b) are labelled for easier reference in the text. Adapted from ref. 39 and ref. 106.

The evolution of the 4f-4f transition peaks in the temperature range between 3 K and 300 K is shown in Figure 4.16, with the focus on the less intense peaks. These spectra are normalized to the background baseline, as explained in the previous Chapter 3. In particular, Figure 4.16a shows that for compound **1** additional peaks appear when the temperature is increased to about 100 K and above, both on the right and left side of the strongest energy transition. With increasing temperature, the new peaks increase in intensity and width, while the intensity of the main transition decreases, as reported by the temperature-dependent energy level positions in Table C1 in Appendix C. The five new transition peaks, present at room temperature and excluding the strongest peak around 6511.5 cm^{-1}, are associated with the transitions from the thermally-populated higher energy doublets of the ground state manifold to the excited state manifold $^4I_{13/2}$, as discussed further below.

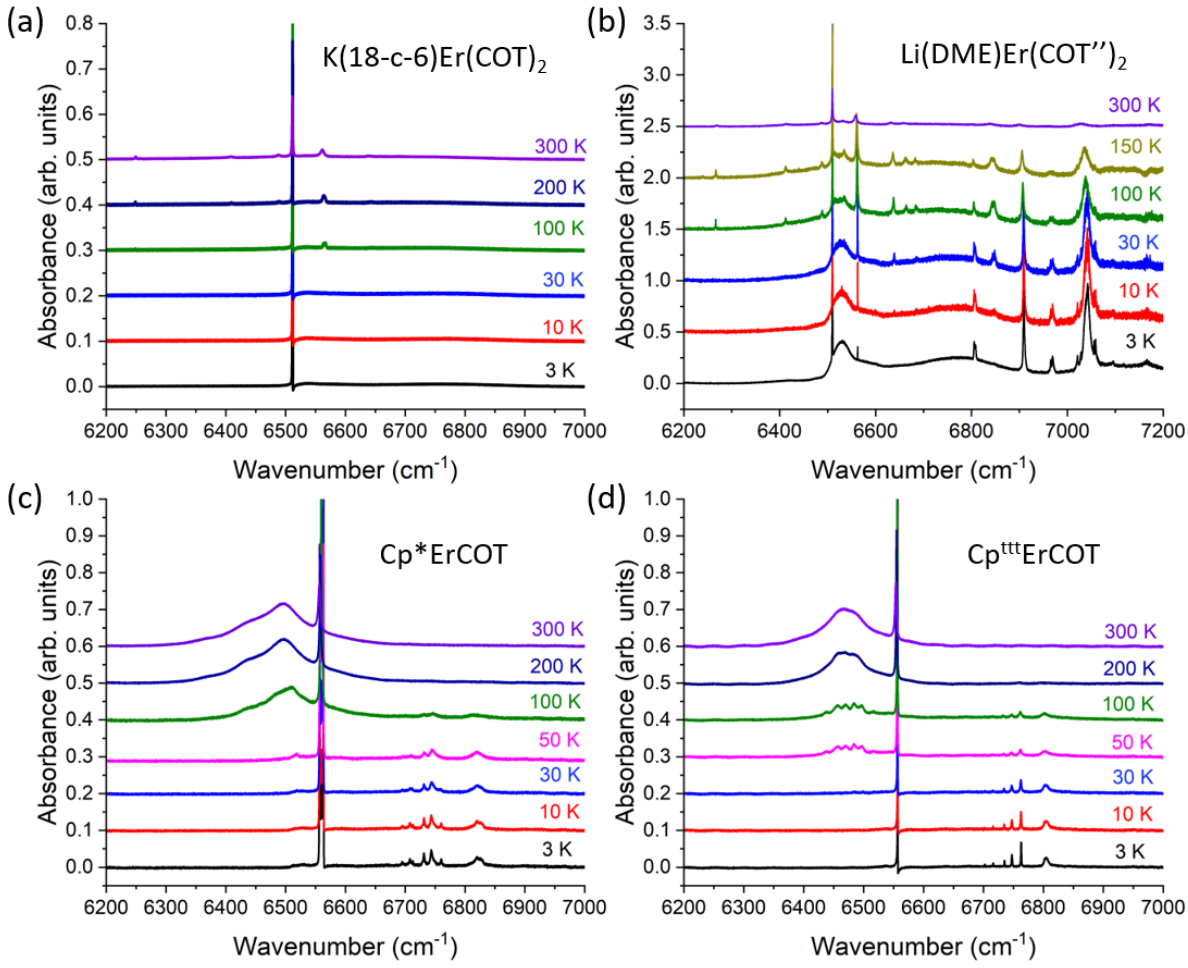

Figure 4.16. Temperature-dependent absorbance spectra in the energy region of Er^{3+} transitions from $^4I_{15/2}$ to $^4I_{13/2}$ states of (a) [K(18-c-6)][Er(COT)$_2$] in KBr, (b) [Li(DME)$_3$][Er(COT'')$_2$] in eicosane, (c) Cp*ErCOT and (d) Cp^{ttt}ErCOT in KBr. The spectra are vertically offset for clarity. Adapted from ref. 106.

For the COT"-based compound **2**, the absorption spectra in Figure 4.16b show seven transition peaks at 3 K, reported in Table C2 in Appendix C, with the most intense transition at the lower wavenumber (lower energy) and the other transitions at higher wavenumber (energy) side. By increasing the temperature, the seven peaks manifest an increase in width and decrease in intensity, while new peaks appear, including some on the lower energy side with respect to the strongest transition. The intensity and width of these new peaks show a complex behavior, generally both increasing with increasing temperature until 150 K. At room temperature, the intensity of all peaks is drastically reduced, with the largest width for the whole temperature series (see Table C2). This effect is associated to the temperature-dependent change of the background baseline, which was detected to change the measured absorbance of the sample. An explanation of this can be found in the thermal treatment of the sample, as the eicosane matrix used to dilute compound **2** changes phase from solid to liquid at ~315 K (see also Chapter 3 for sample preparation). Since the measurements at 300 K were performed after heating the sample from low to room temperature, it is possible that it affected the phase of the matrix or the homogeneity of the sample liquefying it at ~315 K and solidifying it again at 300 K. In addition, we do assume that a partial degradation of the complexes can contribute to the non-linear shape of the background baseline, as explained in Section 3.2.2.

The spectra of sample **3** and **4**, reported respectively in Figures 4.16c and 4.16d, show similarities in the number and positioning of the temperature-dependent energy levels, as explained previously in the case of the base temperature. Both complexes show the presence of seven transition lines at temperatures up to 30 – 50 K, six of which are at the higher energy side of the spectra. At higher temperatures, these peaks decrease in intensity and increase in width, while several new peaks appear on the lower energy side of the spectra, gradually increasing in intensity and width. The energy position, FWHM, intensity and area of those peaks is reported in Appendices C3 and C4.

From the intra-4f transitions reported in Figure 4.16 it is possible to construct partial tentative energy level schemes of the ground state and first excited state manifolds of the compounds. While the temperature evolution and the complex structure of the multi-peaked transition lines of compound **2** complicates extremely the interpretation of the crystal field levels, the other three compounds make the interpretation more straightforward. Compound **1** manifests only one transition line at low temperature, which can be identified with the transition from the ground state doublet $m_J = \pm 15/2$ of Er $^4I_{15/2}$ manifold to the $m_J = \pm 13/2$ doublet of Er $^4I_{13/2}$ manifold, according to the dipole selection rules $\Delta J = \pm 1$ and $\Delta m_J = 0, \pm 1$.[45] The presence of only one transition at this temperature, together with the appearance of only 5 new peaks at higher temperatures, is an indication of low admixing of the states at lower energies in the ground state manifold. By looking at the temperature evolution of the areas of the peaks (reported in Figure D1, Appendix D) it is possible to identify three types of behaviors,

associated with transitions coming from three different doublets of the $^4I_{15/2}$ state. If the doublets are treated as an ideal case of pure m_J states with no admixing, such that every state is identified by only one value of m_J within each manifold, the dipole selection rules allow few transitions to occur, assuming the transitions are still weakly allowed (and none of the oscillator strengths are null). In particular, for the m_J = ±15/2 ground state only the transition to m_J = ±15/2 (of the J = 13/2 manifold) is allowed. Under the same logic, two transitions coming from the same state are possible only if the initial state is m_J = ±1/2, since the selection rule Δm_J = 0, ±1 allows transitions only to states with m_J = ±1/2 and ±3/2. For three transitions, the situation becomes more complicated. In the present case, the binding constraints of the experimental energy levels and the fact that the starting energy level is the same, suggest that the triplet of observed transitions could be starting from the m_J = ±3/2 state to m_J = ±1/2, ±3/2, ±5/2 states. A tentative energy level scheme for this compound is shown in Figure 4.17a relative to the ground state and first excited state manifolds. Figure 4.17b identifies this transitions on the FTIR spectrum at 300 K. Although this attribution is not unique, the energy difference of the transitions relative to peaks P2 and P3 is the same as that of P5 and P6, assuming the ground state doublets are positioned at 262 cm^{-1} and 107 cm^{-1}, respectively.

The extracted energy levels are reported in Table 4.6, where they are compared to the published ab initio calculations performed by the MOLCAS package and the Single-Aniso routine.[33] Note that without the knowledge of all transitions the order of the levels is approximate.

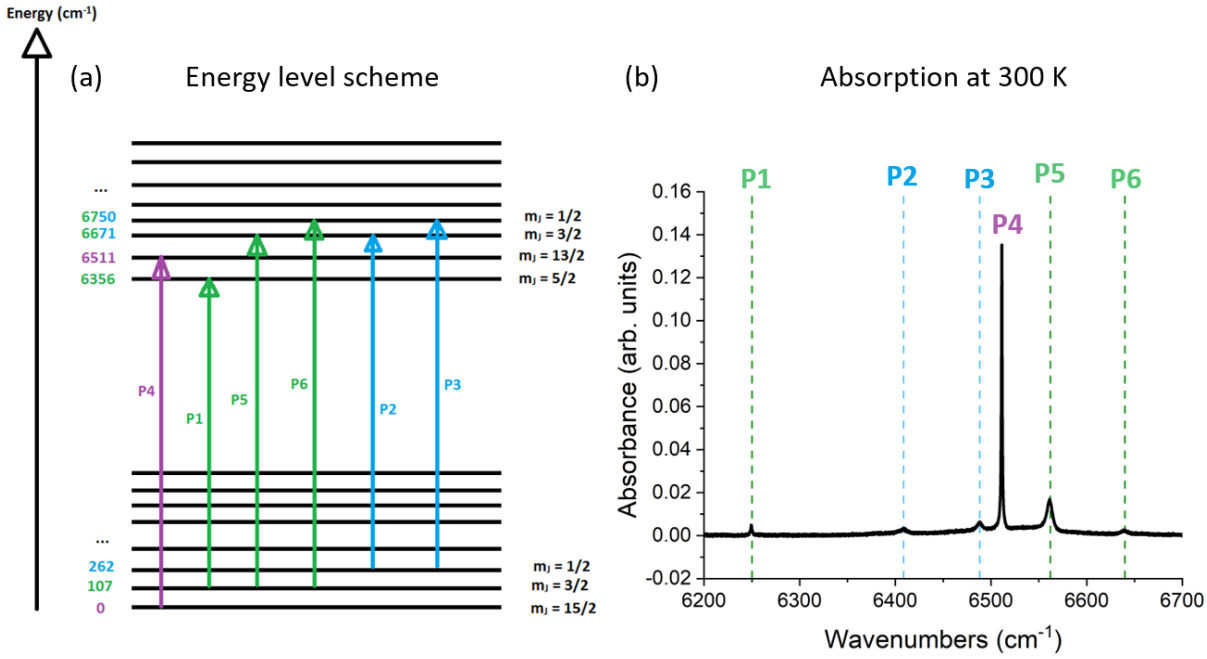

Figure 4.17. (a) Partial tentative energy level scheme of the infrared transitions of Er(III) from the $^4I_{15/2}$ manifold to the $^4I_{13/2}$ manifold of [K(18-crown-6)][Er(COT)$_2$]·2THF (compound **1**) and (b) relative FTIR absorption spectrum at room temperature. The 3 different color lines identify transition starting from 3 different states of the J = 15/2 manifold.

Table 4.6. Energy level positions of the 8 doublets of the ground state manifold $^4I_{15/2}$ and 7 doublets of the first excited manifold $^4I_{13/2}$ of [K(18-crown-6)][Er(COT)$_2$]·2THF (**1**) extracted from the FTIR spectra in Figure 4.16 and represented in Figure 4.17, compared to the published ab initio calculations.[33] The data refers to one of the conformers.

Doublet	Energy (cm^{-1})	
	Experimental	Simulated
1	0	0
2	107 ± 1	171.9
3	262 ± 2	187.7
4	/	267.6
5	/	389.4
6	/	392.0
7	/	491.3
8	/	515.1
9	6356 ± 1	6600.4
10	6511.2 ± 0.2	6810.9
11	6671 ± 1	6813.0
12	6750 ± 2	6861.1
13	/	6936.6
14	/	6949.4
15	/	6994.5

For compounds **3** and **4** the energy level scheme of the first excited manifold $^4I_{13/2}$ can be extracted directly from the spectra at 3 K, corresponding to the transition energies. The values are reported in Table 4.7. Indeed, the 7 transitions can be identified with the 7 dipole-allowed transitions from the $^4I_{15/2}$ manifold to the $^4I_{13/2}$ manifold in case the population is temperature-locked in the ground state doublet, with the admixing of all 16 allowed m_J states. The assumption of the population being in the lowest energy doublet at 3 K is based on the simulated and experimental positioning of the higher energy doublets in the manifold, starting at ~100 cm^{-1}, which is well above the thermal energy contribution of ~2 cm^{-1}.[42–44] In addition, the simulations[44] suggest that the ground state doublet has a main m_J = 15/2 component and minor contributions from the other m_J doublets. The difference in intensity of the different peaks of the two compounds is possibly given by the different weights of the m_J contributions other than the main m_J = 15/2 component.

The exact positions of the other energy levels is hard to estimate because the peaks of compound **3** at temperatures close to 300 K are too broad to extract quantitative conclusions. However, the reported simulations[44] can be used as a starting point to estimate the thermal evolution of the population across the crystal field levels. Relying on the knowledge of the levels in the higher excited manifold, reported in Table 4.7, it is possible to simulate the population of the levels by using the Boltzmann probability. The normalized probability distribution is calculated using the support of the program Matlab,[108] with the input file reported in Appendix E.

Table 4.7. Energy level positions of the 8 doublets of the ground state manifold $^4I_{15/2}$ and 7 doublets of the first excited manifold $^4I_{13/2}$ of Cp*ErCOT (3) and Cp^{ttt}ErCOT extracted from the FTIR spectra in Figure 4.14. The levels indicated with * are taken from reported simulations.[39,44]

Cp*ErCOT (**3**)				Cp^{ttt}ErCOT (**4**)		
Doublet	Energy (cm^{-1})			Doublet	Energy (cm^{-1})	
	Experimental	Simulated[39]			Experimental	Simulated[44]
1	0	0		1	0	0
2*	/	156		2	/	116.4
3*	/	191		3	/	131.7
4*	/	328		4	/	146.4
5*	/	350		5	/	154.6
6*	/	455		6	/	170.5
7*	/	550		7	/	203.7
8*	/	631		8	/	249.9
9	6556.7 ± 0.2	/		9	6556.7 ± 0.2	/
10	6696 ± 1	/		10	6702.3 ± 0.3	/
11	6708 ± 2	/		11	6716.2 ± 0.4	/
12	6731.4 ± 1	/		12	6735.0 ± 0.4	/
13	6744 ± 3	/		13	6747.5 ± 0.7	/
14	6760 ± 2	/		14	6762.8 ± 0.5	/
15	6822 ± 9	/		15	6805 ± 4	/

In the absence of information concerning the oscillator strengths for the transitions from higher energy states of the $^4I_{15/2}$ manifold to the $^4I_{13/2}$ manifolds, it is hard to make meaningful estimations or assumptions on the peak intensities. In the case that these transitions would have the same relative intensities (as peak areas, reported in Table C3, Appendix C) as the transitions from the ground state doublet, it is possible to estimate the effect of the thermal population on the intensities of the transitions, from 3 to 300 K. By using the Boltzmann statistic mentioned previously, temperature dependent plots of the absorbance as a function of energy can be simulated, with the room temperature spectrum reported in Figure 4.18a (other temperatures are reported in Appendix D). The spectrum at room temperature is the most representative since multiple levels of the ground state manifold are thermally populated. Figure 4.18b reports the corresponding experimental FTIR spectrum at 300 K. The comparison of the two spectra in Figure 4.18 shows that at room temperature, the number of simulated peaks and their intensity overestimates the number/intensity of peaks observed experimentally, due to the aforementioned assumptions. In particular, the simulations assume a strong transition to the (component of) m_J = 13/2 doublet of $^4I_{13/2}$ state for all ground state doublets, which translates as an intense peaks in Figure 4.18a (the leftmost of each color series). This phenomenon is not observed experimentally and it suggests that oscillator strengths for transitions to

this doublet are smaller. A different admixing of the levels can also quench specific transitions or influence the measured intensity, which is likely the case here.

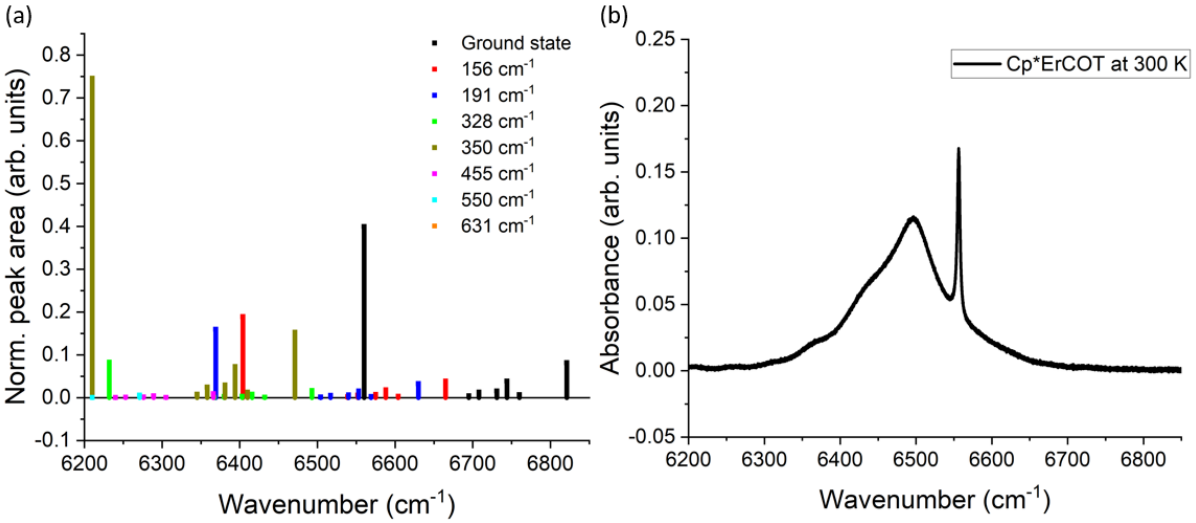

Figure 4.18. (a) Normalized peak areas representing the simulated absorbance at 300 K of Er(III) from the $^4I_{15/2}$ manifold to the $^4I_{13/2}$ manifold of Cp*ErCOT (compound 3) and (b) corresponding experimental FTIR absorption spectrum at room temperature. The different colored bars represent transitions coming from the different ground state doublets.

Although the knowledge of the ground state levels of compound **4** remain elusive as well, the reported simulations can be used for their estimation. By comparing the levels of the two compounds in Table 4.7, the striking similarity of the experimental 4f-4f transitions of the two compounds, which also represent the doublets 9 – 15, can be associated with the similarities in the ligand field splitting of the levels for two compounds, already shown for the static and dynamic magnetic properties in the bulk.[39] However, this is in contrast with the reported simulations of the ground state doublets 2 – 8, suggesting that the splitting between the doublets should rather be similar in both compounds, compared to the large difference shown by the simulations.

A closer look at the temperature evolution of the strongest peaks of compounds **3** and **4**, reported respectively in Figures 4.19a and 4.19b, reveals the presence of a fine structure for the former compound and a single peak for the latter. Figure 4.19a shows that the split peak of compound **3** at 3 K evolves by merging the features into a single central peak as the temperature is increased. The two most intense peaks have a FWHM of 0.8 cm^{-1} and 0.4 cm^{-1} at the lower and higher wavenumber sides, are split by 6.6 cm^{-1} and the area ratio amounts to 43:57, respectively (~5 % error). While the intensities of the side peaks decrease, their positions shift towards each other, merging together with the features between them into a single peak, at a temperature of ~150 K. As discussed further below, the splitting is attributed to the presence of two rotamers (conformers) of the complexes, with the

configurations (top-view) reported in Figure 4.19a. Moreover, the center of the multi-featured peak shifts linearly toward lower wavenumbers with increasing temperature, as shown in Figure 4.19c, together with a gradual decrease of the peak area from about 50 K to 300 K.

The spectra of compound **4** in Figure 4.19b show that the single transition line, with an exceptionally narrow FWHM of 0.2 cm^{-1} at 3 K, increases in width and shifts toward lower wavenumbers at higher temperatures, for a total shift of 3.2 cm^{-1} at room temperature. As reported in Figure 4.19d, the shift has a linear trend, while the area has a nonlinear decay, associated again with the thermal population of higher energy levels.

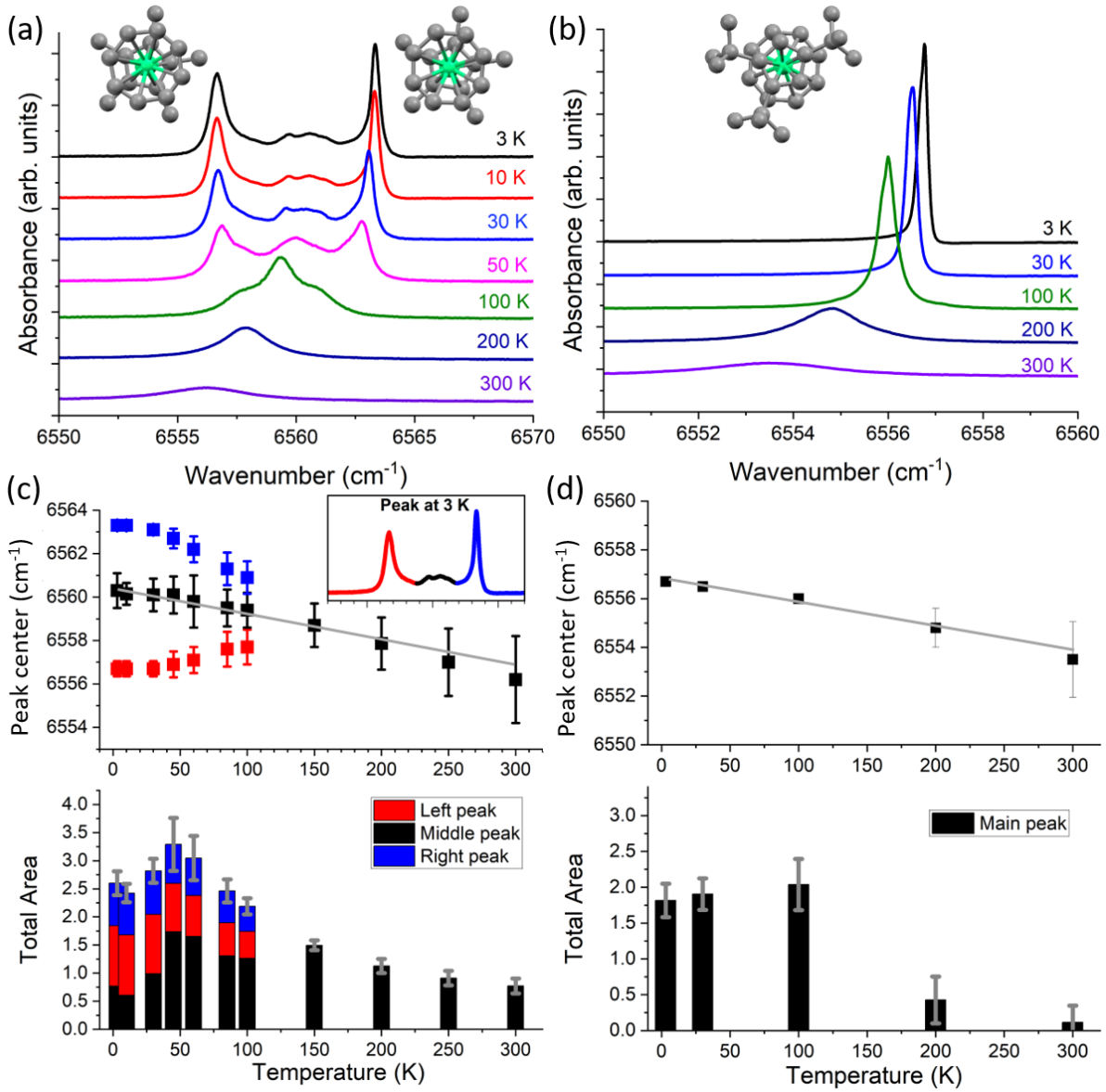

Figure 4.19. Zoom on the most intense absorption peak in the energy region of Er^{3+} transitions from $^4I_{15/2}$ to $^4I_{13/2}$ as a function of temperature of (a) Cp*ErCOT (**3**) and (b) Cp^{ttt}ErCOT (**4**), together with (c-d) the shift of the peak position and the temperature evolution of the total area of the peaks of the two compounds, respectively. The insets indicate the presence of conformers, associated to the splitting of the IR peaks. Adapted from ref. 106.

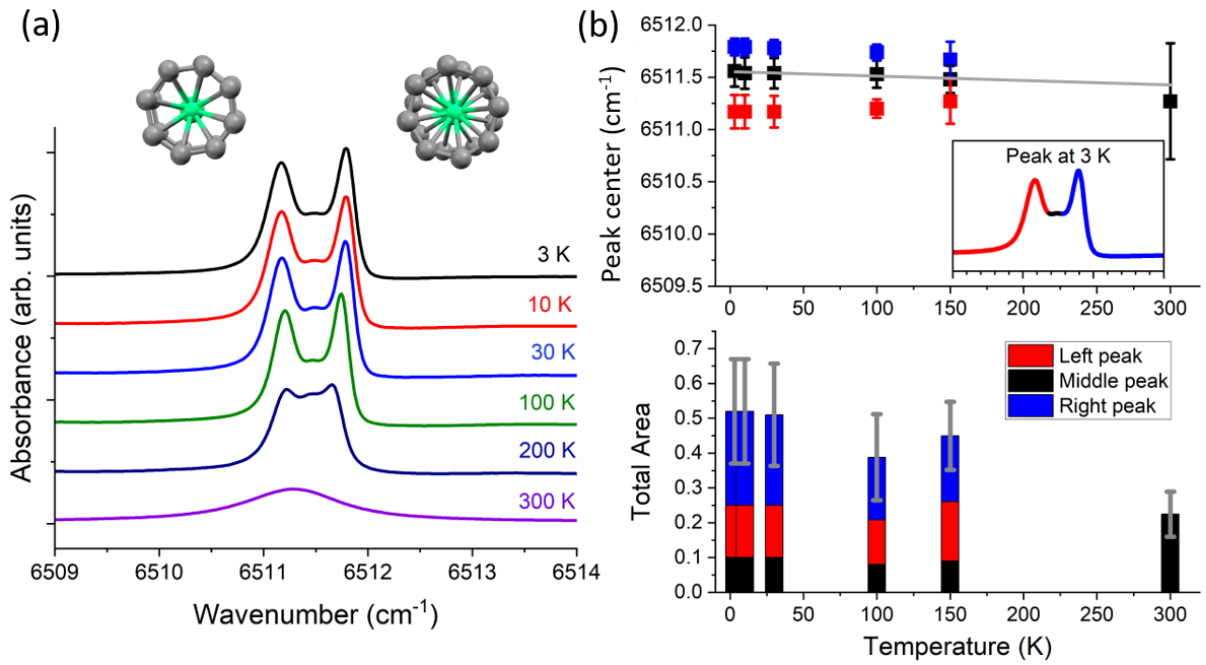

Figure 4.20. (a) Zoom into the most intense absorption peak in the energy region of Er^{3+} transitions from $^4I_{15/2}$ to $^4I_{13/2}$ as a function of temperature of K(18-c-6)Er(COT)$_2$·2THF, together with (b) the shift of the peak position and the temperature evolution of the total area of the peaks. Adapted from ref. 106.

Similarly to compound **3**, Figure 4.20a shows that compound **1** also manifests the splitting of the most intense transition line in two main peaks, separated by 0.6 cm^{-1} at 3 K, associated with two rotamers, as discussed further below. With increasing temperature, the peaks tend to merge into a single broad one, whose center is at lower wavenumbers by 0.3 cm^{-1} at room temperature. Indeed, Figure 4.18b shows that the center of the doubly-split peak shifts linearly to lower wavenumbers with increasing temperature, similarly to the compound **3** and **4** described previously. As discussed further, the shift is attributed to a small variation of the ligand field induced by the thermally induced change of the Er-C distance in the complexes.

To understand further the splitting of the peaks in the FTIR spectra, a linear function is used to fit the temperature-dependent shift of the center of the multi-featured peaks shown in Figure 4.19 and 4.20. The function is subtracted from the position of the side peaks of compounds **1** and **3** as a function of temperature. This results into a linear regression of the position of the peaks, as reported in Figure 4.21. In particular, compound **3** shows that the temperature-driven linear shifts of the peak positions towards the central position happens at ~175 ± 15 K for the left-sided peak in Figure 4.21a (red) and at ~187 ± 10 K for the right-sided one. The peak position at 3 K of the latter peak was excluded from the fit because of the negative shift of the position, considered non-physical in the present case.

In a similar way, linear fits of the left and right-sided peaks of compound **1** reach the central positions at temperatures of 386 K (15 % error) and 794 K (80 % error), respectively.

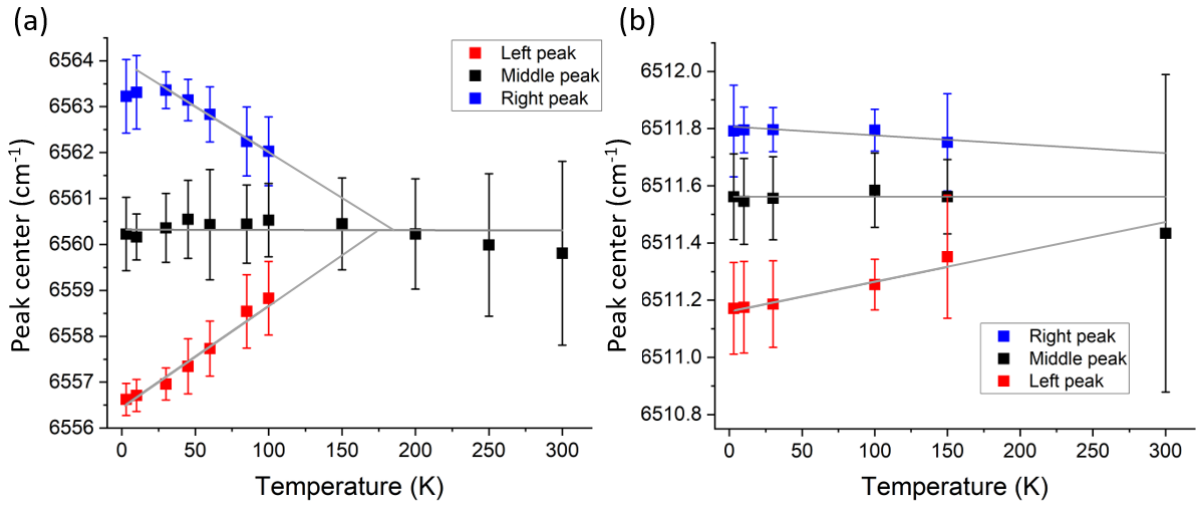

Figure 4.21. Temperature evolution of the peak positions of the strongest transition of Er^{3+} from $^4I_{15/2}$ to $^4I_{13/2}$ manifolds of (a) Cp*ErCOT (**3**) and (b) [K(18-c-6)][Er(COT)$_2$]·2THF (**1**), after removing the contribution of the thermal shift of the central peak, due to the variation of the Er-C inter-distance. Adapted from ref. 106.

As discussed below, it is possible to associate energy barriers to the processes responsible for the temperature-induced evolution of FTIR peaks, in particular those associated with the splitting of the strongest 4f-4f transitions. In case of compound **3**, the temperatures extracted previously from the two peaks indicate a barrier between 1.5 ± 0.1 kJ/mol and 1.6 ± 0.1 kJ/mol. For compound **1** the two values give two different energy barrier values, corresponding to 3.2 ± 0.5 kJ/mol and 6.6 ± 5.3 kJ/mol.

4.2.2 Discussion: intra-4f transitions of ErCOT-based SMMs

Fourier-transform infrared spectroscopy shows clearly that in case of the studied Er^{3+} COT-based complexes the intra-4f transitions are weakly allowed. This behavior is associated to the low symmetry of the complexes and the mixing of the 4f and 5d levels, which induces small oscillator strengths for the 4f-4f transitions. In fact, the dihedral tilt of the ligand planes of few degrees for the bis-COT and bis-COT" containing anions, as well as the heteroleptic Cp* and Cp^{ttt} containing complexes, is a clear indication of lower symmetry of the complexes with respect to the ideal $C_{\infty v}$, playing a fundamental role in the optical properties of these complexes. In particular, the ligand field induces variations in

the IR spectra, although some aspects are common to all studied complexes. The generally large splitting of the m_J levels of the studied Er-based SMMs allows the assumption that at 3 K only the lowest lying energy doublet of the ground state manifold is occupied. As suggested by literature, the Er^{3+} complexes tend to have the ground state doublet coinciding with the largest value of m_J = ±15/2.[38,39,44,57] In case of states with a single m_J component, the selection rules impose only one allowed transition from the m_J = 15/2 state of the ground state manifold to the m_J = 13/5 state of the first excited manifold. This picture fits well the case of complex **1** ([K(18-c-6)][Er(COT)$_2$]·2THF) which shows only one sharp transition in this energy region. The presence of two equivalent and almost parallel COT ligands, with a dihedral angle of only 2.8°,[32] generate an almost symmetric ligand field, resulting in virtually pure m_J energy levels. Upon the functionalization of the COT ligand with the silyl group, the dihedral angle between the two $(COT'')^{2-}$ ligand rings increases to 3.6°[37] and the resulting complex **2** ([Li(DME)$_3$][Er(COT'')$_2$]) shows many more transitions in the aforementioned energy range. Although the two complex have structural similarities in the first coordination shell and the presence of the delocalized π orbitals of the ligand rings, the lower symmetry of the $(COT'')^{2-}$-based molecule causes the mixing of higher energy m_J states, resulting in more transitions observed, already at 3 K. As an example, reported simulations[44] suggest that the wavefunction of the ground state doublet of compound **3** (Cp*ErCOT) is composed as:

$$|\Psi_1\rangle_{J=15/2} = 0.95\left|\Psi_{m_J=\pm15/2}\right\rangle + \sum_{m_J\neq\pm15/2} \alpha_{m_J}\left|\Psi_{m_J}\right\rangle$$

with the sum of the remaining α_{m_J} coefficients being 0.05 (the sum over all the possible m_J states is 1), while the first excited doublet composed as (for one of the conformers):

$$|\Psi_2\rangle_{J=15/2} = 0.22\left|\Psi_{m_J=\pm1/2}\right\rangle + 0.2\left|\Psi_{m_J=\pm13/2}\right\rangle + 0.19\left|\Psi_{m_J=\pm11/2}\right\rangle + \sum_{m_J} \alpha_{m_J}\left|\Psi_{m_J}\right\rangle$$

With a small contributions of the other m_J states of the manifold.[44] Indeed, the complexes **2**, **3** and **4** (Cp^{ttt}ErCOT) show all 7 peaks at 3 K, corresponding to the 7 allowed transitions from the J = 15/2 state to the J = 13/2 state, although with different intensities for each peak, depending on the level of admixing and the oscillator strengths between the different levels. The stronger contribution comes from the transition to the m_J 13/2 doublet, as expected from the performed CASSCF/RASSI-SO/SINGLE-ANISO simulations for the Cp*ErCOT complex.[44] In particular, the measured FTIR spectra of the complexes **3** and **4** at 3 K allow for an exact reconstruction of the energy level scheme of the $^4I_{13/2}$ manifold of the Er^{3+} ion, reported in Table 4.7.

Upon increasing the temperature towards the room temperature, the higher energy doublets of the J = 15/2 state are thermally populated, allowing more transition to occur. However, a precise drawing of the energy levels of the ground state manifold remains elusive, being on the same level of approximation as the reported simulations.[33,39,44] However, relying upon the simulated ground state

manifold and the experimentally determined energy levels of the first excited manifold, it is possible to simulate the temperature population of the ground state doublets. The resulted spectrum, as shown for compound **3** in Figure 4.18, reproduces some of the features of the experimental spectra, but lacks the information about the oscillator strengths of the multiple transitions involved. While the simulated peak positions at energies ~6000 cm^{-1} match the broad features displayed by the experimental spectra at 300 K, ab-initio simulations, based on the ligand-field DFT model,[109] could answer the open question and eventually reproduce better the experimental spectra.

The high resolution of 0.01 cm^{-1} of the FTIR spectra is used to trace the evolution of the fine structure displayed by the IR peaks as a function of temperature. In particular, the strongest 4f-4f transitions of complexes **1** and **3** show a splitting at lower temperatures, while **4** shows only a single transition peak in this energy region. The reason behind such behaviour was attributed to the presence of rotamers in the crystal lattice at low temperatures for the former two compounds, which consist of different stacking configuration of the ligand rings in the complexes, as explained in Chapter 1. Indeed, slightly different positions of the ligands could induce small variations of the ligand field experienced by the central Er ion, which in turn induces a change in the splitting of the m_J levels in the manifolds. The two main rotamer configurations for **1** and **3** were reported in the original papers[32,42] and a "top-view" representing them is shown in Figure 4.17 and 4.18, respectively. Moreover, the ratio of the areas of the two main peaks constituting the strongest transition of **3** (43:57) is very similar to the ratio of the conformers reported by the original paper (38:62).[38]

In particular, the simulations of the ground state multiplet of these compounds show slightly different energy positions for the doublets belonging to different conformers.[33,44] The splitting of the IR spectral lines due to multiple rotamer configurations was reported also for other compounds, in particular for ferrocene.[110] Similarly to compound **1**, ferrocene is a homoleptic complex based on Cp. It has been shown[110] that it crystallize in two different stacking configurations, the staggered and the stacking configuration, depending whether the carbons of the two rings are superimposed or are rotated by $2\pi/10$ with respect to each other. Similarly, the heteroleptic CpTiCOT also crystallizes in two different configurations.[111] As opposed to that, it was recently reported[39] that compound **4** has a single rotamer configuration, due to the large steric pressure coming from the neighbouring atoms in the crystal packing. Thus the presence of only one sharp transition, corresponding to 6556.7 cm^{-1} at 3 K, and other 6 narrow dipole-allowed transition lines is a clear indication that the splitting of the peaks is originating from the presence of different configuration of the ligand rings in the complexes.

Moreover, complexes **1** and **3** show a clear shift of the rotamer-split peak positions and the merging into a single peak at increasing temperatures. Such process is attributed to the temperature-activated rotation of the ligand rings around the main axis of the complexes. At low temperatures, the

complexes are frozen in either of the rotamer configurations, but once the thermal energy is sufficiently high to move the complex out of the local energy minimum of a specific configuration, the Cp*/COT/COT" rings tend to freely rotate between the different configurations. Thus, at room temperature the Er ion experiences a ligand field which is given by an average potential generated by the overlap of the different metastable rotamer configurations, due to the fast rotation of the ligands. Although ab-initio simulations can be helpful in determining the potential energy surface of the compounds in relation to the rotation around the main axis of the complexes, the shift of the peak position, converging to a central peak, can also give an indication of the energy barriers of the onset rotations. In particular, for compound **3** a barrier of 1.5 ± 0.2 kJ/mol is estimated, average of the two barriers reported in the previous Section.

For compound **1** the merging of the peaks occurs at higher temperatures, estimated to be higher than 300 K. From the fits in Figure 4.21, the energy barrier for the activation of the rotation is estimated between 3.2 ± 0.5 kJ/mol and 6.6 ± 5.3 kJ/mol. The large error on the values (especially the latter) originates from the small shift of the peaks, compared to their FWHM values. In comparison, the activation barrier for the rotation around the central axis of ferrocene is estimated to be in the range of 3.9 to 5.4 KJ/mol,[112] while that of CpTiCOT to be 4.2 KJ/mol.[111] The values obtained experimentally from the temperature-dependent FTIR spectra in the present case fall in the range of expected values for similar molecules. The fact that the complex featuring two COT rings, with the COT being smaller in the diameter compared to the Cp* ring, has a higher energy barrier for the activation of the rotation suggests that bulkier ligands, like the Cp*, have lower activation barriers for the rotations. This effect is counterintuitive, but it can be explained by a stronger interaction of the larger Cp* ring with the surrounding environment, which is more sensitive to the motion of ligands induced by thermally-activated roto-vibrational modes of adjacent complexes.

Also, the strongest transition lines of the complexes shift linearly towards lower energies with increasing temperature, independently from the presence of multiple rotamers, as identified by the spectra of complex **4**. The shift is attributed to the temperature–dependent variation of the Er-COT/Cp* ring distance. An increased distance between the Er^{3+} ion and the carbon atoms of the ligand rings at higher temperatures has been reported for complex **3**.[38] The energy level shift can be approximated by a linear fit and explained by a linear dependence of the ligand field parameters of the ligand field Hamiltonian affectin the multiplet splitting. A stronger effect can be seen in the molecules featuring the derivates of the cyclopentadiene ligand. The decreasing of the absorbance with the temperature is a reflection of the ground state depletion due to the Boltzmann population of the ground state multiplet.

The present results show that the different ligand fields originated from different ligands used in Er^{3+}-based SMMs is not the only factor affecting the exact position of the 4f-4f transitions, but temperature and the presence of conformers (rotamers) can also strongly influence the details of the absorbance in the NIR range. The existence of multiple conformers can reduce the transition probabilities of resonant processes featuring the 4f levels of such complexes, but it can also be seen as an ensemble of different sub-states within the same compound. The latter can be useful for spintronic applications that require the presence of multiple populated states even at the lowest temperatures.

Summary

The objective of the work reported in this thesis is to investigate the optical properties in the NIR region in bulk, as well as the magnetic properties within the monolayer range, of organometallic sandwich complexes based on Er^{3+}. These systems, which share a common structural similarity, feature at least one of either the cyclooctatetraenide ligand or its functionalized trimethylsilyl-cyclooctatetraenide counterpart. Additionally, these complexes exhibit a distinct magnetic hysteresis opening in bulk at temperatures of a few kelvin, which is characteristic of single-molecule magnets (SMMs).

Two of the studied complexes exhibit completely different self-assemblies when thermally sublimed on the prototypical metal Ag(100) surface in the monolayer regime, due to different intramolecular interactions, as well as different degrees of interaction with the substrate. In particular, scanning-tunneling microscopy shows that Cp*ErCOT SMMs forms compact rows of alternating standing-up and lying-down molecules parallel to the crystallographic [010] and [001] directions of the substrate, while $K[Er(COT)_2]$ complexes arrange in highly ordered uniaxial domains, oriented with the main rotational axis parallel to the surface. X-ray linear dichroism and X-ray magnetic circular dichroism measurements indicate that the net anisotropy is strong in the case of $K[Er(COT)_2]$ and weak for Cp*ErCOT. The polarization-dependent X-ray absorption spectra are compared to the simulations performed by multiX, a point-charge ab-initio model simulating the electrostatic potential of the charges surrounding the central Er ion. The simulations suggest that the strong in-plane magnetic anisotropy of $K[Er(COT)_2]$/Ag(100) and the mixed in-plane and out-of-plane magnetization of Cp*ErCOT/Ag(100) can be ascribed to the strikingly distinct surface ordering of these two complexes. Compared to the strong SMM behavior of the complexes in bulk, Cp*ErCOT shows a weak hysteresis opening both in plane and out of plane, likely due to the stronger interaction of the molecules with the substrate through their conjugated π orbitals. On the other hand, the hysteresis of $K[Er(COT)_2]$ displays significant openings, implying only a minor influence of the substrate on the magnetic properties. This effect is linked to the poor interaction of the π-conjugated orbitals with the substrate, given by the orientation of the orbitals parallel to the Ag surface. This behavior suggests that the electron cloud engaging directly with the metallic surface experiences a stronger interaction with the substrate. This interaction affects the magnetic properties of the complexes by increasing the magnetization relaxation rate, in contrast to the scenario where the electronic orbitals are aligned parallel to the metal substrate.

While this study demonstrates that Er^{3+} sandwich SMMs based on the COT or COT" ligands can be transferred on the surfaces and partially retain their magnetic hysteresis opening, we also propose that the orientation and interaction of π orbitals can profoundly influence the technologically relevant magnetic properties of these systems. These results instigate further research on this topic, in connection with other similar Ln-based sandwich SMMs and/or different substrates.

At the same time, Fourier-transform infrared spectroscopy in the range of the transitions between the Er^{3+} ground state ($^4I_{15/2}$) and the first excited state ($^4I_{13/2}$) shows the ligand-field induced differences of these manifolds in four Er^{3+}-based SMMs. While the [K(18-c-6)][$Er(COT)_2$]·2THF displays few transitions, [$Li(DME)_3$][$Er(COT")_2$], Cp*ErCOT and Cp^{ttt}ErCOT complexes show a larger number of 4f-4f transitions.

The difference in the spectra is attributed to a different admixing of the m_J doublets of the ground state and first excited state manifolds. In particular, the most symmetric complex, [K(18-c-6)][$Er(COT)_2$]·2THF, shows only 1 intra-4f transition at 3 K, compared to the 7 weakly dipole-allowed transitions detected for the other three compounds. The energies of these transitions are used to extract partial energy level schemes of the complexes in this energy region, which are compared to previously published simulations. Additionally, minor differences arising from distinct ligand fields of the rotamer configurations in the complexes are identified as peak splitting at 3 K. The temperature evolution of the intra-4f transitions unveils the dynamics of ligand ring rotation around their principal/main rotational axis, encompassing thermally induced transitions between meta-stable rotamer positions and culminating in an average effect of the ligand field at temperatures approaching 300 K. The energy barriers of the process governing the relaxation of the static disorder of the complexes are estimated from the spectra and compared to similar barriers in homoleptic and heteroleptic complexes, such as $FeCp_2$ and CpTiCOT.

The m_J level mixing and the different positions of the energy levels of similar Er^{3+}-based SMMs reveal that the intricate environment/structure of the complex significantly influences the intra-4f level transitions, which hold importance for technological applications. In addition, the presence of conformers dictates the precise details of the optically relevant $^4I_{15/2}$ to $^4I_{13/2}$ transitions at temperatures below 300 K.. This circumstance can either present a drawback or offer an advantage, as the conformers may serve as distinct subsets with similar optical properties but different ground states.

In conclusion, this thesis provides a comprehensive study of how the substitution of one or both ligand rings in structurally similar Er^{3+}-based sandwich SMMs affects the magnetic properties in the monolayer range on Ag(100) and the optical properties of those compounds in bulk. The importance of both these regimes is the primary goal of understanding the physical properties of these systems

and, subsequently, the potential for their application in technology. The results presented give a novel insight into these promising organometallic sandwich complexes, laying the foundation for enhanced design and understanding of similar systems on surfaces, as well as the optical behavior correlated with the employed ligands.

Acknowledgments

Coming towards the end of my PhD journey, I understand how much I have experienced, learned, struggled and grown in the past years, in both scientific and personal environment. I enjoyed every single moment of my research, which connected me with amazing people, captivated my interested towards science and showed me the beauty of working in large-scale facilities such as SLS. Even in times of the Covid-19 pandemic, the atmosphere created by the group I have worked with kept my motivation and focus high.

The quality of time spent at SLS would not have been the same without my supervisor and mentor Dr. Jan Dreiser, who collaborated with me on daily basis, sharpened my skills and sparked my mind with constantly new challenges and problem-solving strategies. I would also like to thank him for his patience and friendly attitude, which made my stay in the laboratories feel like being at home.

I would like to thank my co-supervisor Prof. Frithjof Nolting for his guidance, commitment to teach me science and critic thinking, as well as for keeping high my interest towards the world of X-ray spectroscopy.

I would like to acknowledge all my colleagues from the Magnetism and Microscopy group at PSI, who supported me and helped me throughout my stay at the SLS, which made me feel welcomed and part of an amazing research group. Starting from Dr. Urs Staub and Dr. Cinthia Piamonteze, the members of the group showed me that the world of research is made by friendly, smart and open-minded people. With this regard, a special acknowledgement goes to Dr. Diana Vaclavkova, Dr. Ludmila Leroy, Dr. Anna Zakharova and Federico Stramaglia, which were like a family to me and supported me in every aspect of the daily life at PSI.

In addition, I want to thank all the people that worked with me on the projects connected to my research and helped me to carry them out, including: Moritz Bernhardt, Martin Heinrich, Dr. Katie Harriman, Dr. Niéli Daffé, Dr. Bernard Delley, Dr. Maciej Damian Korzyński, Dr. Matthias Muntwiler, Prof. Christophe Copéret, Prof. Muralee Murugesu, Dr. Harry Ramanantoanina, Dr. Guy Matmon and others. My thanks go also to the researchers I have collaborated with on external projects. I would also like to thank Stefan Zeugin that supported me in my daily experimental life and helped me to solve a multitude of issues connected to the performed measurements.

I would also like to thank the people closest to me outside of the research environment, like my mom Olga Radidyal, and my closest friends (Jessica, Lucia, Elvio, Riccardo and the members of the Music club) for their extraordinary support, constantly pushing me forward and motivating me to give always

my best. I thank all those people who are not mentioned here but have always supported me and believed in my success, which gave me the strength to pursue my goals and overcome the troubles met along the way.

Finally, I would like to thank the Swiss National Science Foundation for the grant No. 200020_182599 that financed the research performed and presented in the current work.

List of abbreviations

- **COT** – Cyclooctatetraenide
- **COT"** – Trimethylsilyl-cyclooctatetraenide
- **Cp** – Cyclopentadienide
- **Cp^{ttt}** – Tris(tert-butyl)cyclopentadienide
- **Cp*** - Pentamethyl-cyclopentadienide
- **DME** - Dimethoxyethane
- **FTIR** – Fourier-transform infrared
- **FWHM** – Full width at half-maximum
- **IR** – Infrared
- **LH** – Linear "horizontal" polarization
- **LF-DFT** – Ligand field – density functional theory
- **LV** – Linear "vertical" polarization
- **ML** – Monolayer
- **NIR** – Near infrared
- **PSI** – Paul Scherrer Institut
- **QTM** – Quantum tunneling of magnetization
- **SIM** – Single-ion magnet
- **SMM** – Single-molecule magnet
- **STM** – Scanning-tunneling microscopy
- **SLS** – Swiss Light Source
- **THF** – Tetrahydrofuran
- **UHV** – Ultra-high vacuum
- **XAS** – X-ray absorption spectroscopy/spectrum
- **XAFS** – X-ray absorption fine structure
- **XLD** – X-ray linear dichroism
- **XMCD** – X-ray magnetic circular dichroism
- **XPS** – X-ray photoemission spectroscopy
- **(18-c-6)** – 18-crown-6 ether

Appendix A:
multiX INPUT example file

#all the information about the mutiX code can be found on the website: #http://multiplets.web.psi.ch/
the code is based on the publication reported at #DOI:https://doi.org/10.1103/PhysRevB.85.125133
#uncomment the desired line. XAS and XMCD has separate entry lines.

#new MULT #new multiplet calculation
#new XMCD #XMCD script
#new XAS #XAS script
atom Er
ground_state 3d10 4f12
scaler_coulomb 0.85
scaler_so_coupling 0.95 #0.930
The matrix elements obtained by first principles are scaled by these two values, typically to #fit the experimental data, due to the screening arising from the passive electrons

scaler_xtal_field 1.182
#scales all the charges in the point charge parametrization for the CF/LF field together for #convenient fit optimization

threshold_corr 22.5
#is a parameter to correct for the deficiencies of the underlying DFT based orbital model for #the excitation energy, less than a 2% correction here
core_hole_broad 0.45
deltag1 1.00
wming1 1398.0
wmaxg1 1440.0
#those are empirical parameters describing the Lorentzian lifetime broadening of the core hole due #to the coupling with the relevant continua:
#photon re-emission, Auger, relaxation processes. The later three parameters are for a linear #ramp function of the core hole.

temperature 3 #used for the population of the sub-states

```
#the beam direction is in the xyz frame, where xy is the substrate plane (y pointing "up" in the #experimental
configuration) and z is out of plane direction
#polar_in 0 1 0 # LV in normal incidence (and any else)
#polar_in 1 0 0 # LH in normal incidence
#polar_in 0 1 0 # LV in grazing incidence
#polar_in -0.5 0 -0.866 # LH in grazing incidence 60 deg
#polar_in 0 1 0 # LV in grazing incidence 90 deg
#polar_in 0 0 -1 # LH in grazing incidence 90 deg

#beam_in 0 0 -1 # beam direction in normal for XMCD
beam_in -0.886 0 -0.5 #beam direction in grazing 60 deg
#beam_in -1 0 0 #beam direction in grazing 90 deg

#bfield 0.05
#bfield 6.8
#bfield_dir 0 0 -1 #direction of magnetic field in normal
#bfield_dir -0.886 0 -0.5 #magnetic field direction in grazing 60 deg
#bfield_dir -1 0 0 #magnetic field direction in grazing 90 deg

begin_xtal          #ligand field parameters and positions
   1.000000   [Angstroems]   x y z      q      radius
  -1.8310    1.9120        0    0.2500
  -1.2947    1.9120   -1.2947    0.2500
      0    1.9120   -1.8310    0.2500
   1.2947    1.9120   -1.2947    0.2500
   1.8310    1.9120        0    0.2500
   1.2947    1.9120    1.2947    0.2500
      0    1.9120    1.8310    0.2500
  -1.2947    1.9120    1.2947    0.2500
  -1.8310   -1.9120        0    0.2500
  -1.2947   -1.9120   -1.2947    0.2500
      0   -1.9120   -1.8310    0.2500
   1.2947   -1.9120   -1.2947    0.2500
   1.8310   -1.9120        0    0.2500
   1.2947   -1.9120    1.2947    0.2500
      0   -1.9120    1.8310    0.2500
  -1.2947   -1.9120    1.2947    0.2500
end_xtal
```

Appendix B:
Additional X-ray absorption spectra

Additional XAS/XLD/XMCD spectra and magnetic hysteresis curves of $K[Er(COT)_2]$/Ag(100) and Cp*ErCOT/Ag(100) are reported in this Appendix and compared to the spectra reported in Chapter 4. The additional spectra are obtained from samples that were prepared following the same procedure used for the samples presented in the main text, as explained in Chapter 3.1.1, following the same experimental geometry used for the samples discussed in the main text. In particular, the spectra of 0.5 and 2 MLs coverages of $K[Er(COT)_2]$/Ag(100), which are presented in Sections 4.1.3, 4.1.4 and 4.1.5, are compared to the spectra of the additional sample of 1 ML coverage in Figures B1, B2 and B3. In a similar way, the spectra of 0.5 and 4 MLs coverages of Cp*ErCOT/Ag(100) are compared to the spectra of the additional sample of 2 ML coverage in Figures B4, B5 and B6.

The comparison shows that the linearly/circularly polarized spectra and the XLD/XMCD spectra follow the same trend for each complex, supporting the conclusions discussed in Chapter 4.1.6.

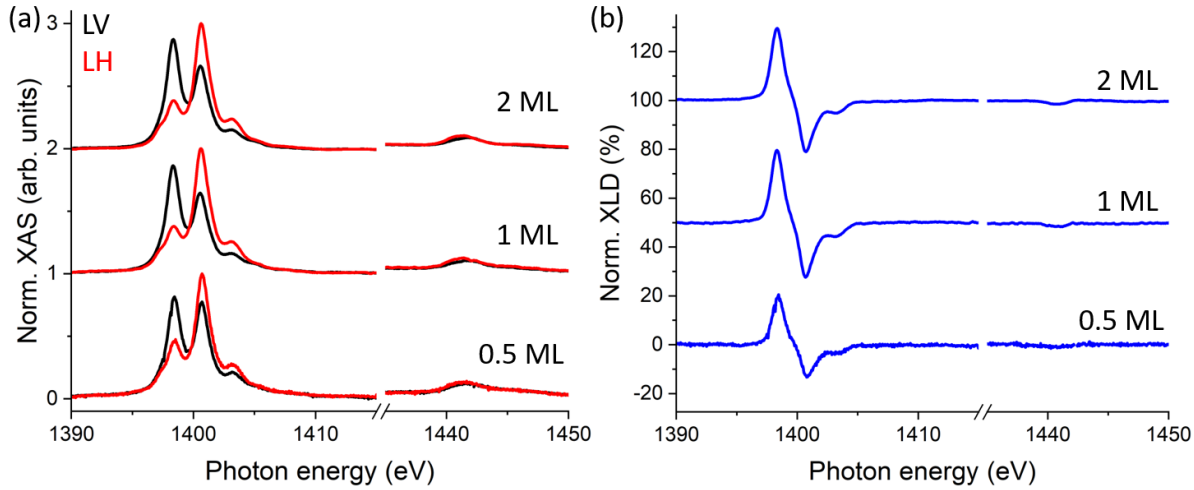

Figure B1. (a) Linearly polarized XAS and (b) XLD spectra of the Er $M_{4,5}$-edge measured at 3 K and 50 mT in grazing incidence of $K[Er(COT)_2]$/Ag(100). The spectra of 0.5 and 2 MLs coverage and the experimental geometry are reported and discussed in Chapter 4.

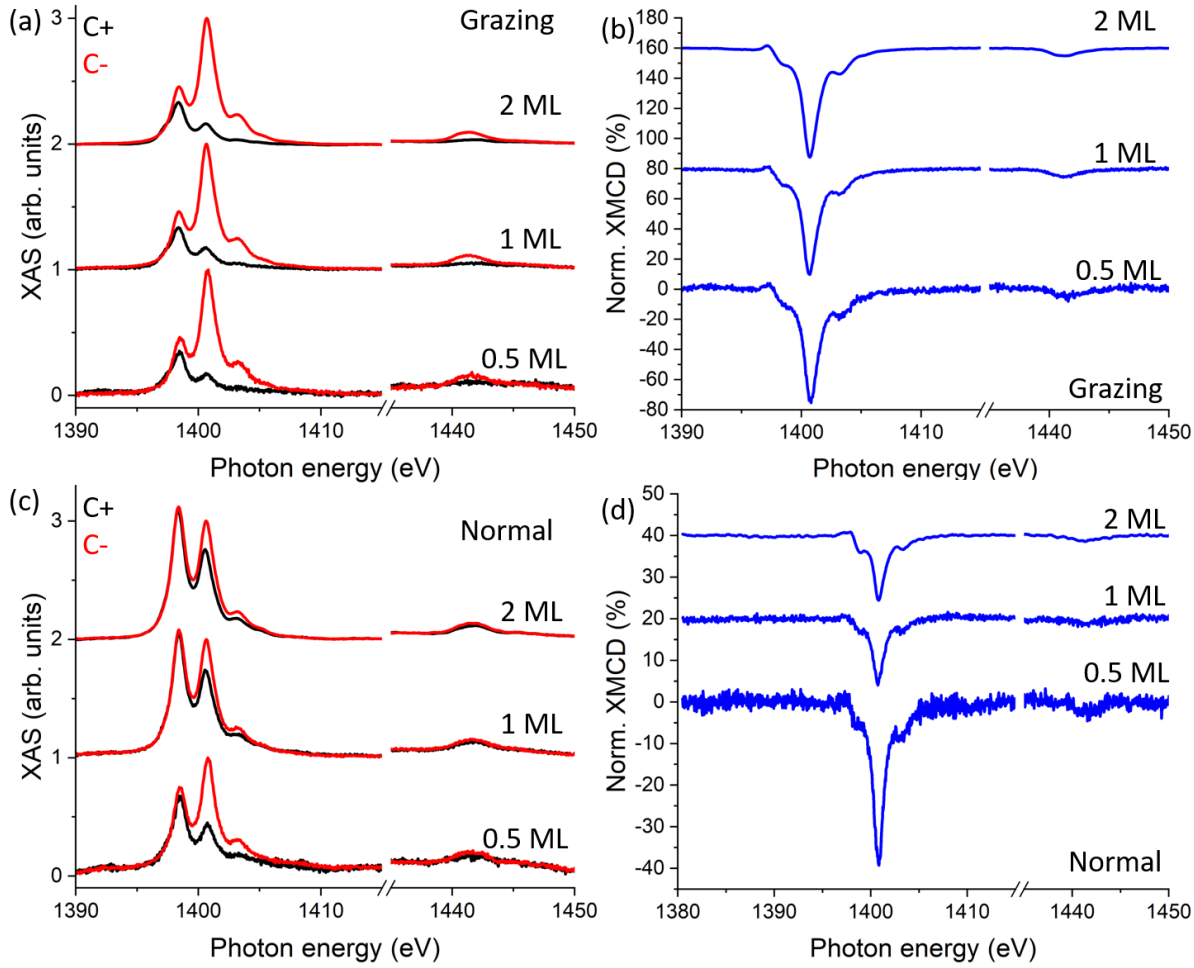

Figure B2. Circularly polarized XAS of the Er $M_{4,5}$-edge measured at 3 K and 6.8 T in (a) grazing and (c) normal incidence of $K[Er(COT)_2]$/Ag(100); (b) and (d) show the XMCD spectra for the two configurations, respectively. The spectra of 0.5 and 2 MLs coverage and the experimental geometry are reported and discussed in Chapter 4.

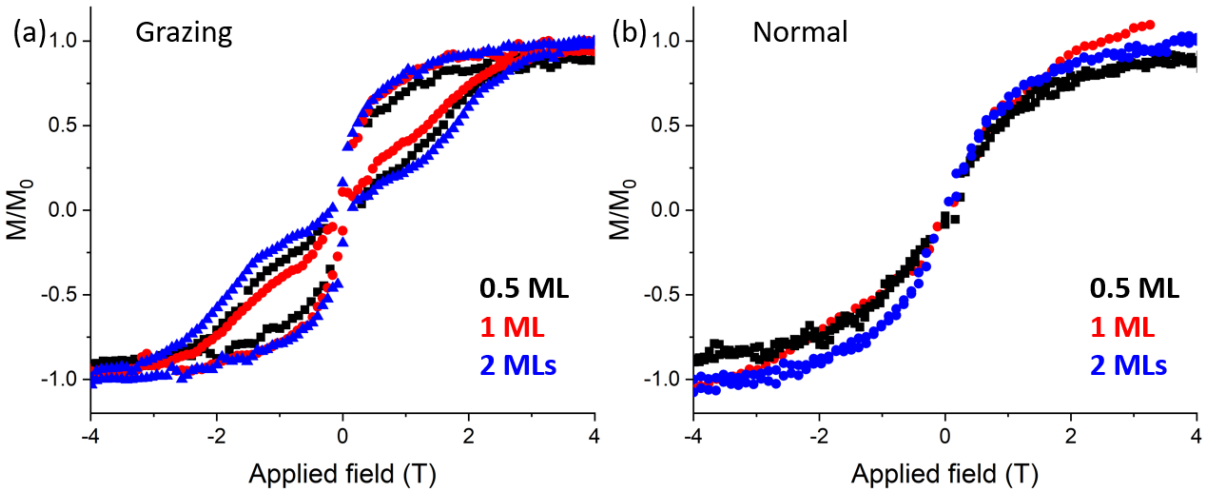

Figure B3. XMCD-detected magnetic hysteresis loops recorded at 3 K of $K[Er(COT)_2]$/Ag(100), at a field sweep rate of 2 T min^{-1}. (a) Grazing (60°) and (b) normal indicate the photon incidence on the sample. The spectra of 0.5 and 2 MLs coverage are reported and discussed in Chapter 4.

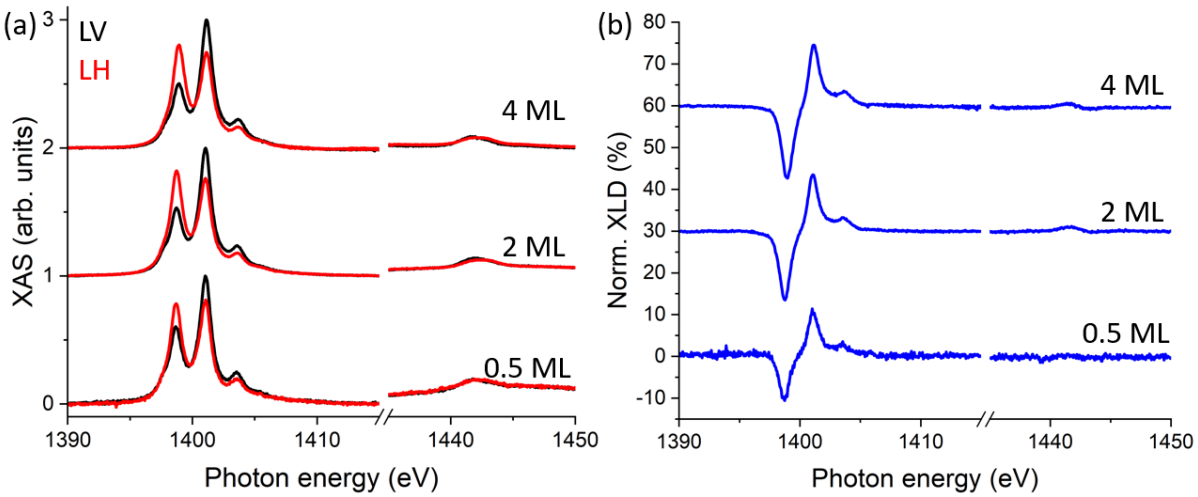

Figure B4. (a) Linearly polarized XAS and (b) XLD spectra of the Er $M_{4,5}$-edge measured at 3 K and 50 mT in grazing incidence of Cp*ErCOT/Ag(100). The spectra of 0.5 and 4 MLs coverage are reported and discussed in Chapter 4.

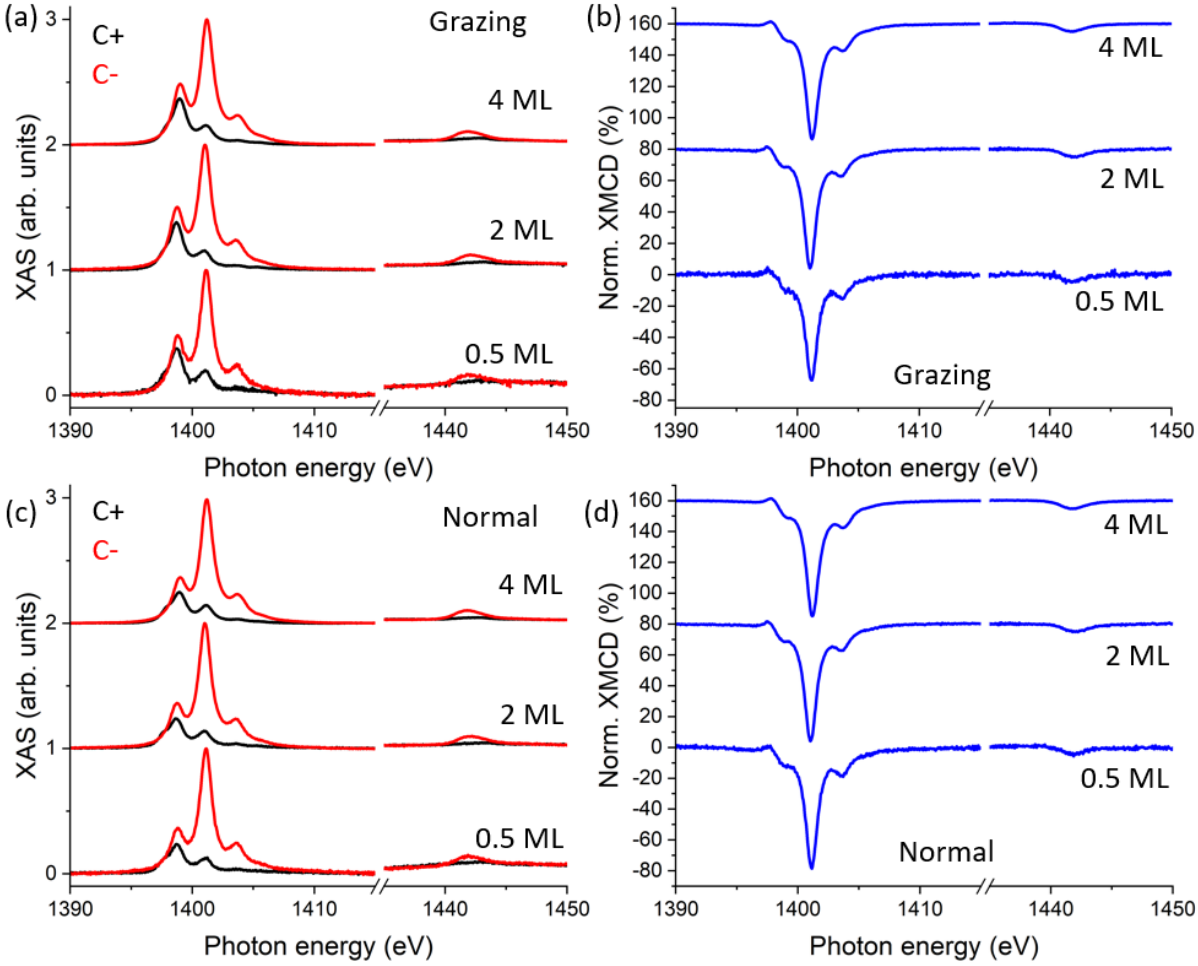

Figure B5. Circularly polarized XAS of the Er $M_{4,5}$-edge measured at 3 K and 6.8 T in (a) grazing and (c) normal incidence of Cp*ErCOT/Ag(100); (b) and (d) show the XMCD spectra for the two configurations, respectively. The spectra of 0.5 and 4 MLs coverage are reported and discussed in Chapter 4.

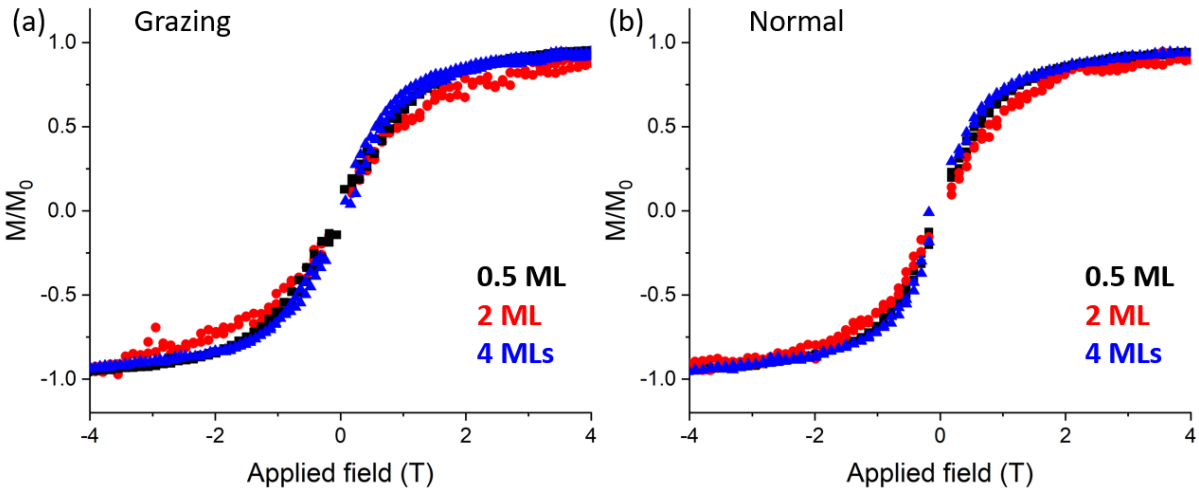

Figure B6. XMCD-detected magnetic hysteresis loops recorded at 3 K of Cp*ErCOT/Ag(100), at a field sweep rate of 2 T min^{-1}. (a) Grazing (60°) and (b) normal indicate the photon incidence on the sample. The spectra of 0.5 MLs coverage are reported and discussed in Chapter 4.

Appendix C: Temperature-dependent FTIR energy levels

This appendix includes tables with detailed data extracted from FTIR spectra presented in Chapter 4. Peaks that are not detected at certain temperature are labelled as “none”, while peaks that could not be fitted due to poor attribution of energy positions and fitting parameter are labelled by “?”.

Table C1. Energy level positions, area, FWHM and absorbance intensity of compound **1** ([K(18-crown-6)][Er(COT)$_2$]·2THF) extracted from fits of the absorbance spectra reported in Figure 4.13, Chapter 4.

Peak	Temperature (K)	Energy (cm^{-1})	Best Fit	Absorbance	FWHM (cm^{-1})	Area
P1	300	6249.5	Lorentz	0.0045	1.77±0.05	0.0121±0.0003
	153	6248.71	Lorentz	0.0029	1.91±0.03	0.0088±0.0001
	100	6248.82	Lorentz	0.0017	2.0±0.2	0.05±0.01
	30	none				
	10	none				
	3	none				
P2	300	6408	Lorentz	0.0021	8.7±0.1	0.0259±0.0003
	153	6409.38	Lorentz	0.0014	2.7±0.3	0.0056±0.0004
	100	6409.56	Lorentz	0.0007	4.6±0.1	0.0051±0.0001
	30	none				
	10	none				
	3	none				
P3	300	6487.95	Lorentz	0.0031	6.27±0.08	0.0338±0.0005
	153	6488.69	Lorentz	0.0021	3.6±0.2	0.0093±0.0004
	100	6488.61	Lorentz	0.0004	3.6±0.1	0.0052±0.0001
	30	none				
	10	none				
	3	none				

Peak	Temperature (K)	Energy (cm^{-1})	Best Fit	Absorbance	FWHM (cm^{-1})	Area
P4	300	6511.27	Lorentz	0.128	1.111±0.001	0.2248±0.0002
	153	6511.27	Lorentz	0.360	0.177±0.002	0.08±0.01
		6511.48		0.057	0.26±0.01	0.09±0.01
		6511.67		0.315	0.34±0.01	0.17±0.01
	100	6511.2	Lorentz	0.495	0.285±0.009	0.221±0.007
		6511.53		0.181	0.26±0.04	0.08±0.01
		6511.74		0.559	0.146±0.006	0.128±0.006
	30	6511.17	Lorentz	0.538	0.303±0.007	0.26±0.01
		6511.54		0.216	0.29±0.03	0.10±0.01
		6511.78		0.606	0.154±0.005	0.15±0.01
P4	10	6511.17	Lorentz	0.533	0.32±0.01	0.27±0.01
		6511.54		0.209	0.30±0.04	0.10±0.02
		6511.79		0.594	0.16±0.01	0.15±0.01
	3	6511.17	Lorentz	0.536	0.32±0.01	0.27±0.01
		6511.56		0.198	0.30±0.04	0.10±0.01
		6511.79		0.596	0.16±0.01	0.15±0.01
P5	300	6561.06	Lorentz	0.0139	6.59±0.02	0.1445±0.004
	153	6563.88	Gauss	0.0155	4.91±0.03	0.096±0.001
	100	6563.58	Lorentz	0.0111	2.76±0.07	0.048±0.001
		6566.94		0.0107	1.65±0.06	0.027±0.001
	30	none				
	10	none				
	3	none				
P6	300	6639.21	Lorentz	0.00149	8.0±0.1	0.0119±0.0001
	153	6642.87	Gauss	0.00122	7.27±0.04	0.0112±0.0001
	100	6643.49	Gauss	0.000714	6.96±0.07	0.0062±0.0001
	30	none				
	10	none				
	3	none				

Table C2. Energy level positions, area, FWHM and absorbance intensity of compound **2** ($[Li(DME)_3][Er(COT'')_2]$) extracted from fits of the absorbance spectra reported in Figure 4.13, Chapter 4.

Peak	Temperature (K)	Energy (cm^{-1})	Best Fit	Absorbance	FWHM (cm^{-1})	Area
P0	300	none				
	151	6239.87	Lorentz	0.011	2.33±0.03	0.041±0.001
	100	6239.37	Lorentz	0.011	1.8±0.02	0.030±0.001
	30	none				
	10	none				
	3	none				
P1	300	6268.32	Lorentz	0.0072	5.80±0.03	0.0652±0.0003
	151	6266.76	Lorentz	0.0663	1.86±0.01	0.193±0.001
	100	6266.39	Lorentz	0.0807	1±0.01	0.127±0.001
	30	none				
	10	none				
	3	none				
P2	300	6413.35	Lorentz	0.00864	9.00±0.03	0.122±0.001
	151	6412.41	Lorentz	0.0541	3.23±0.02	0.276±0.001
	100	6412.22	Lorentz	0.053	2.2±0.1	0.179±0.003
	30	none				
	10	none				
	3	none				
P3	300	6487.36	Lorentz	0.0079	6.44±0.05	0.080±0.001
	151	6487.71	Lorentz	0.046	4.19±0.04	0.325±0.003
	100	6488.27	Lorentz	0.0506	3±0.1	0.24±0.01
	30	none				
	10	none				
	3	none				
P4	300	6509.7	Lorentz	0.267829	1.70±0.01	0.715±0.003
	151	6509.82	Lorentz	1.4232	0.85±0.01	1.90±0.01
	100	6509.56	Lorentz	0.572	0.64±0.02	0.58±0.03
		6509.78		1.596	0.078±0.04	0.201±0.006
		6510.04		1.025	0.41±0.02	0.65±0.04
		6510.14		0.099	2.6±0.8	0.40±0.06
		6510.48		0.102	0.3±0.1	0.05±0.03
	30	6508.66	Lorentz	0.188	0.09±0.03	0.036±0.01
		6509.3		0.439	0.34±0.03	0.233±0.01
		6509.53		0.317	0.10±0.01	0.051±0.01
		6509.82		2.555	0.174±0.003	0.7±0.01
		6509.98		1.7	0.073±0.004	0.192±0.001
		6510.11		0.277	0.23±0.04	0.10±0.02

Peak	Temperature (K)	Energy (cm^{-1})	Best Fit	Absorbance	FWHM (cm^{-1})	Area
		6510.53		0.262	0.15±0.02	0.06±0.01
	10	6508.64	Lorentz	0.1463	0.14±0.02	0.033±0.004
		6509.23		0.408	0.23±0.02	0.15±0.02
		6509.35		0.11495	0.112±0.08	0.02±0.02
		6509.49		0.3187	0.17±0.02	0.09±0.02
		6509.73		1.4025	0.074±0.002	0.16±0.01
		6509.85		1.358	0.085±0.003	0.18±0.01
		6509.97		1.366	0.086±0.003	0.19±0.01
		6510.07		0.641	0.14±0.01	0.14±0.01
		6510.52		0.2445	0.15±0.01	0.056±0.003
	3	6508.63	Lorentz	0.205275	0.14±0.02	0.04±0.01
		6509.22		0.435	0.24±0.04	0.16±0.05
		6509.3		0.090966	0.08±0.11	0.01±0.03
		6509.46		0.3407	0.12±0.02	0.07±0.01
		6509.71		0.3508	0.14±0.04	0.08±0.04
		6509.87		1.6055	0.32±0.02	0.8±0.1
		6510.04		0.4135	0.16±0.04	0.10±0.04
		6510.5		0.2535	0.12±0.02	0.049±0.008
P5	300	6532.48	Lorentz	0.008948	8.25±0.07	0.116±0.001
	151	6534.27	Lorentz	0.05658	5.1±0.1	0.453±0.004
	100	6534.93	Lorentz	0.051	5.9±0.2	0.46±0.02
	30	none				
	10	none				
	3	none				
P6	300	6558.06	Lorentz	0.058868	5.97±0.02	0.552±0.002
	151	6560.69	Lorentz	0.4338	3.08±0.01	2.16±0.01
	100	6561.41	Lorentz	0.638	2.11±0.01	2.11±0.01
	30	6562.24	Lorentz	0.811	0.598±0.003	0.759±0.003
	10	6562.43	Lorentz	0.4407	0.38±0.01	0.262±0.002
	3	6562.5	Lorentz	0.128845	0.22±0.01	0.045±0.001
P7	300	6631.75	Lorentz	0.011198	8.96±0.01	0.1659±0.0003
	151	6635.97	Lorentz	0.107	4.16±0.01	0.7±0.01
	100	6637.22	Lorentz	0.141	3.08±0.03	0.68±0.01
	30	6638.59	Lorentz	0.091	1.63±0.03	0.233±0.005
	10	6638.82	Lorentz	0.0321	1.47±0.03	0.0744±0.0004
	3	none				

Peak	Temperature (K)	Energy (cm^{-1})	Best Fit	Absorbance	FWHM (cm^{-1})	Area
P8	300	6657.6	Lorentz	0.00654	13.83±0.03	0.1540±0.0004
	151	6662.62	Lorentz	0.046	5.3±0.1	0.41±0.01
	100	6663.78	Lorentz	0.051	4.7±0.1	0.37±0.01
	30	none				
	10	none				
	3	none				
P9	300	6678.47	Lorentz	0.00109	7.6±0.1	0.0195±0.0003
	151	6682.52	Lorentz	0.036	4.2±0.1	0.24±0.01
	100	6684	Lorentz	0.049	3.8±0.1	0.30±0.01
	30	6685.89	Lorentz	0.024	5.2±0.4	0.20±0.01
	10	none				
	3	none				
P10	300	6800.15	Lorentz	0.0038	8.90±0.07	0.0539±0.0004
	151	6803.89	Lorentz	0.0524	3.1±0.1	0.26±0.01
	100	6805.05	Lorentz	0.091	3.3±0.1	0.48±0.01
	30	6805.49	Lorentz	0.138	1.7±0.05	0.37±0.01
		6808.07		0.094	3.0±0.1	0.44±0.02
	10	6805.53	Lorentz	0.147	1.55±0.01	0.356±0.004
		6808.23		0.117	2.71±0.03	0.50±0.01
	3	6805.56	Lorentz	0.154533	1.89±0.02	0.46±0.01
		6808.32		0.132269	2.67±0.03	0.55±0.01
P11	300	6838.37	Lorentz	0.0117	20.37±0.04	0.375±0.001
	151	6841.28	Lorentz	0.072	7.59±0.05	0.88±0.01
		6847.14		0.067	8.5±0.1	0.93±0.01
	100	6842.62	Lorentz	0.101	5.63±0.03	0.89±0.01
		6846.97		0.116	6.12±0.03	1.12±0.01
	30	6843.91	Lorentz	0.059	2.8±0.1	0.26±0.01
		6848.54		0.097	4.3±0.1	0.65±0.01
	10	6847.79	Lorentz	0.033	6.64±0.07	0.345±0.003
	3	none				
P12	300	6900.04	Lorentz	0.01034	9.53±0.05	0.155±0.001
	151	6905.61	Lorentz	0.1897	5.43±0.04	1.61±0.01
	100	6907.14	Lorentz	0.34	4.12±0.02	2.20±0.01
	30	6808.8	Lorentz	0.65	3.19±0.01	3.26±0.01
	10	6909.07	Lorentz	0.7485	3.01±0.01	3.54±0.01
	3	6909.12	Lorentz	0.78787	2.99±0.01	3.70±0.01

Peak	Temperature (K)	Energy (cm^{-1})	Best Fit	Absorbance	FWHM (cm^{-1})	Area
P13	300	6961.94	Lorentz	0.001882	14.1±0.4	0.042±0.001
	151	6964.53	Lorentz	0.0235	9.2±0.4	0.36±0.01
	100	6964.01	Lorentz	0.036	5.04±0.04	0.291±0.002
		6969.29		0.037	4.84±0.04	0.288±0.002
	30	6965.16	Lorentz	0.079	2.6±0.1	0.33±0.01
		6969.55		0.102	3.7±0.1	0.60±0.01
	10	6965.19	Lorentz	0.0873	1.96±0.03	0.270±0.004
		6969.62		0.133	3.59±0.03	0.75±0.01
	3	6965.31	Lorentz	0.095714	1.83±0.02	0.275±0.002
		6969.57		0.14518	3.43±0.02	0.782±0.004
P14	300	7029.23	Lorentz	0.022	34.9±0.2	1.26±0.01
	151	7019.67	Lorentz	0.021	2.6±0.1	0.083±0.001
		7035.89		0.2134	19±0.1	6.35±0.3
		7058.17		0.021	3.8±0.1	0.128±0.004
	100	7020.34	Lorentz	0.037	4.0±0.1	0.36±0.01
		7038.48		0.386	17.5±0.1	10.64±0.01
		7056.14		0.03	1.20±0.03	0.058
		7058.92		0.043	2.25±0.04	0.154
	30	7020.85	Lorentz	0.078	2.4±0.1	0.32±0.02
		7040.96		0.66	14.5±0.1	15.11±0.01
		7056.14		0.076	1.3±0.1	0.18±0.01
		7058.76		0.123	1.1±0.1	0.23±0.01
	10	7021.06	Lorentz	0.087	2.0±0.1	0.29±0.01
		7027.96		0.069	1.3±0.1	0.16±0.01
		7041.3		0.707	13.7±0.1	15.65±0.07
		7055.97		0.104	1.1±0.1	0.17±0.01
		7058.82		0.138	1.3±0.1	0.28±0.01
	3	7021.06	Lorentz	0.093	2.30±0.04	0.348±0.006
		7027.97		0.071	1.26±0.05	0.16±0.01
		7041.45		0.77	13.5±0.1	16.46±0.07
		7056.01		0.102	1.01±0.04	0.172±0.006
		7058.8		0.141	1.21±0.04	0.28±0.01
P15	300	7169.39	Lorentz	0.003	19.4±0.7	0.098±0.003
	151	7169.47		0.114	21.5±0.2	3.85±0.04
	100	7173		0.023	13.6±0.1	0.68±0.02
	30	7166		0.03	21±1	1.08±0.01
	10	7163.65		0.02	18±1	0.70±0.06
	3	7165.1		0.042	20.1±0.4	1.36±0.03

Table C3. Energy level positions, area, FWHM and absorbance intensity of compound **3** (Cp*ErCOT) extracted from fits of the absorbance spectra reported in Figure 4.13, Chapter 4.

Peak	Temperature (K)	Energy (cm^{-1})	Best Fit	Absorbance	FWHM (cm^{-1})	Area
P1	3	6556.7	Lorentz	0.8085	0.7	0.8501
		6559.7		0.2174	1.7	0.3722
		6560.9		0.2278	1.6	0.3948
		6563.3		1.0944	0.4	0.6681
	10	6556.7	Lorentz	0.7734	0.7	0.799
		6559.7		0.202	1.1	0.253
		6560.6		0.212	0.9	0.1759
		6563.3		1.0685	0.4	0.608
	30	6556.7	Lorentz	0.6647	0.7	0.6615
		6559.5		0.2872	1.2	0.3129
		6560.7		0.265	1.8	0.6753
		6563.1		0.8721	0.4	0.5358
	45	6556.9	Lorentz	0.5267	0.84	0.567
		6560.1		0.422	2.8	1.736
		6562.7		0.581	0.9	0.733
	60	6557.1	Lorentz	0.43	1.2	0.7273
		6559.8		0.4739	2.4	1.653
		6562.2		0.401	1.2	0.6665
	85	6557.6	Lorentz	0.3073	1.6	0.5873
		6559.5		0.5626	1.7	1.3057
		6561.3		0.3337	1.5	0.5696
	100	6557.7	Lorentz		1.8	0.4794
		6559.4		0.5862	1.6	1.2648
		6560.9			1.5	0.4446
	150	6558.7	Lorentz	0.4744	2	1.4958
	200	6557.86		0.2959	2.4	1.1268
	250	6557		0.1787	3.1	0.912
	300	6556.2		0.1207	4	0.7716
P2	3	6695.5	Lorentz	0.0074	2.9	0.0343
	10	6695.5		0.008	4	0.0404
	30	6695.9		0.0044	3.1	0.0166
	45	6698.1		0.0036	18.2	0.086
P2	60	none				
	85	none				
P3	3	6708	Lorentz	0.0154	3.6	0.0877
	10	6708		0.016	4	0.0886
	30	6709.1		0.0089	5.4	0.0672
	45	6710.2		0.0064	8.5	0.0679
	60	6703.6		0.0057	48.8	0.4531
	85	6703.9		0.0032	25.9	0.1149
	100	6700.5		0.0017	23.8	0.0598

Peak	Temperature (K)	Energy (cm^{-1})	Best Fit	Absorbance	FWHM (cm^{-1})	Area
P3 #2	3	6712.9	Lorentz	0.01	1.2	0.0174
	10	6712.9		0.0096	1.4	0.0167
	30	6712.4		0.007	1.6	0.007
	45	none				
	60	none				
	85	none				
P4	3	6731.3	Lorentz	0.03	2.7	0.1247
	10	6731.4		0.0274	2.7	0.1105
	30	6731.4		0.0189	4.2	0.1159
	45	6731.7		0.0158	4.9	0.0979
	60	6731.9		0.0114	5.3	0.0737
	85	6731.9		0.008	7.9	0.0699
	100	6731.3		0.006	8.3	0.0586
P5	3	6744.1	Lorentz	0.04	5.2	0.3048
	10	6744.1		0.0348	5.3	0.276
	30	6744.7		0.0245	8	0.3073
	45	6745.8		0.0221	11.6	0.3937
	60	6746.5		0.018	13	0.3508
	85	6746.8		0.0117	13	0.2325
	100	6746.5		0.0086	13.6	0.1748
P6	3	6760.1	Lorentz	0.016	2.3	0.055
	10	6760		0.0142	2.4	0.047
	30	6757.5		0.0068	10	0.07
P7	3	6821.7	Lorentz	0.0215	17.6	0.6396
	10	6821.7		0.0184	17.5	0.5482
	30	6821		0.0183	18.8	0.5615
	45	6820		0.016	21.8	0.6435
	60	6819.1		0.0128	21.5	0.4889
	85	6818.3		0.0102	27.4	0.426
	100	6818.5		0.0072	33.2	0.3864

Table C4. Energy level positions, area, FWHM and absorbance intensity of compound **3** ($Cp^{ttt}ErCOT$) extracted from fits of the absorbance spectra reported in Figure 4.13, Chapter 4.

Peak	Temperature (K)	Energy (cm^{-1})	Best Fit	Absorbance	FWHM (cm^{-1})	Area
P1	50	6437.1	Lorentz	0.009	9.7	0.0938
	100	6436.9	Lorentz	0.0128	12.9	0.1632
	200	6435	Lorentz		53.8	1.4134
P2	50	6455.8	Lorentz	0.0207	14.1	0.4142
	100	6455.8	Lorentz	0.0292	15	0.5764
	200	6455.8	Lorentz		26.6	1.8278
P3	50	6469.9	Lorentz	0.022	9.1	0.2387
	100	6469.9	Lorentz	0.0296	10.2	0.3367
	200	6469.9	Lorentz		20.2	0.9173
P4	30	6484.6	Lorentz	0.0027	4	0.018
	50	6484.4	Lorentz	0.024	9.4	0.3053
	100	6484.2	Lorentz	0.0313	10.4	0.4107
	200	6484	Lorentz		21.9	1.1844
P5	30	6498.4	Lorentz	0.0022	2.5	0.0091
	50	6496.6	Lorentz	0.0198	7.9	0.206
	100	6496.4	Lorentz	0.0254	9.1	0.2892
	200	6496	Lorentz		22.3	0.732
P6	50	6516.5	Lorentz	0.0052	5.6	0.0342
	100	6516.3	Lorentz	0.0066	7.2	0.0526
	200	6516	Lorentz		16.8	0.1314
P7	3	6556.7	Lorentz	2.34	0.2	0.776
	3	6556.7	Gauss		0.2	0.566
	10	6556.6	Lorentz	2.5276	0.2	0.83077
	30	6556.5	Lorentz	2.2136	0.2	0.9855
	50	6556.1	Lorentz	1.558	0.4	1.0524
	100	6556	Lorentz	1.78	0.4	1.1448
	200	6554.8	Lorentz	0.409	1.6	1.045
	300	6553.5	Lorentz	0.1504	3.1	0.7534
P8	3	6702.3	Lorentz	0.0075	0.6	0.0051
	10	6702.3	Lorentz	0.0038	0.8	0.0051
	30	6702.1	Lorentz	0.0028	1	0.0046
	50	6701.1	Lorentz?		0.6?	0.0018
	100	none				

Peak	Temperature (K)	Energy (cm^{-1})	Best Fit	Absorbance	FWHM (cm^{-1})	Area
P9	3	6716.2	Lorentz	0.0108	0.8	0.0103
	10	6716	Lorentz	0.005	1.1	0.0108
	30	6715.7	Lorentz	0.0039	1.5	0.0102
	50	6715.1	Lorentz	0.0022	1.8	0.0069
	100	6715	Lorentz	0.0021	2.6	0.0078
	200	?				
P10	3	6735	Lorentz	0.018	0.8	0.0207
	10	6734.7	Lorentz	0.0118	1.2	0.0237
	30	6734.3	Lorentz	0.0086	1.5	0.0219
	50	6733.3	Lorentz	0.0041	2.6	0.0168
	100	6732.8	Lorentz	0.0037	3	0.0178
	200	?				
P11	3	6747.5	Lorentz	0.0347	1.3	0.07
	10	6747.3	Lorentz	0.0244	1.9	0.0787
	30	6747.1	Lorentz	0.0164	2.7	0.0759
	50	6746.8	Lorentz	0.007	4.2	0.0497
	100	6746.8	Lorentz	0.0069	4.6	0.046
	200	?				
P12	3	6762.8	Lorentz	0.0695	1	0.106
	10	6762.6	Lorentz	0.0456	1.6	0.118
	30	6762.3	Lorentz	0.0318	2.3	0.1178
	50	6761.7	Lorentz	0.0144	4.1	0.1002
	100	6761.5	Lorentz	0.013	4.5	0.0985
	200	6759.1	Lorentz	0.0022	11.2	0.0449
P13	3	6804.8	Lorentz	0.0261	7.8	0.294
	3	6804.8	Gauss	0.0253	7.2	0.19
	10	6804.7	Lorentz	0.02	9.2	0.3304
	10	6804.7	Gauss	0.02	7.2	0.1726
	30	6804	Lorentz	0.0169	10.1	0.3033
	50	6803.1	Lorentz	0.0107	13.8	0.2474
	100	6803	Lorentz	0.0102	13.6	0.2178
	200	6803.4	Lorentz	0.0018	51.9	0.281

Appendix D:
Additional details relative to IR transitions of Er(III)-based SMMs

The graphs in this Appendix are complementary to the simulations reported in Chapter 4.1.2 for the temperature-dependent FTIR spectra of [K(18-c-6)][Er(COT)$_2$]·2THF and Cp*ErCOT complexes dispersed in KBr in the energy region corresponding to the transition of Er^{3+} from the $^4I_{15/2}$ manifold to the $^4I_{13/2}$ manifold.

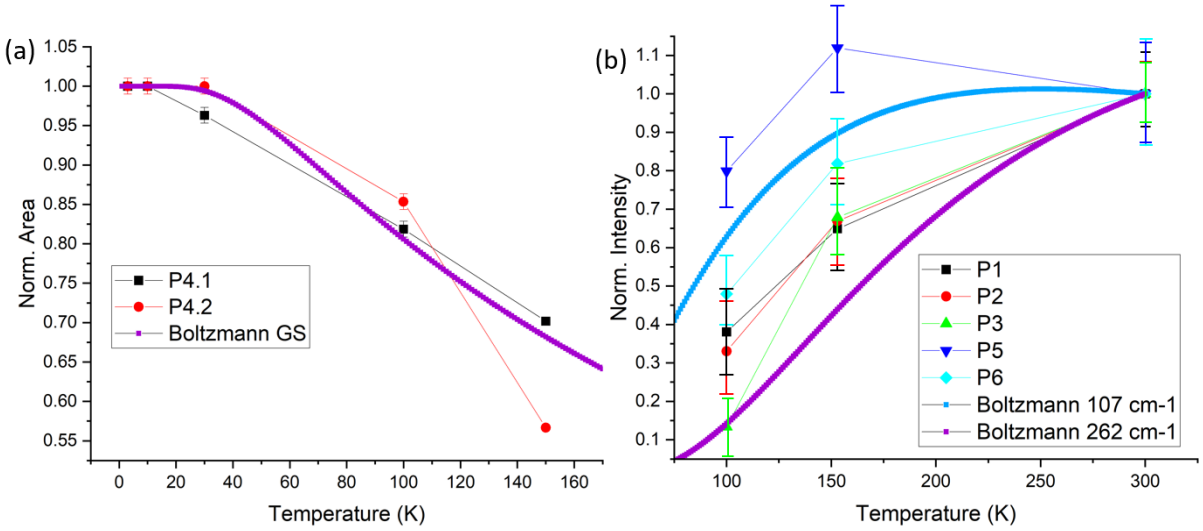

Figure D1. Temperature evolution of the absorbance (integrals of the peaks) divided in trends, corresponding to different group of transitions of complex **1** ([K(18-c-6)][Er(COT)$_2$]·2THF). The plots show the evolution of (a) the strongest double peak (P4.1 and P4.2) and (b) the other peaks (P1, P2, P3, P5 and P6) of the complex, together with the Boltzmann distributions, as explained in Chapter 4.2.1. Higher energy states for the simulations were extracted from published simulations,[33] also reported in Table 4.6.

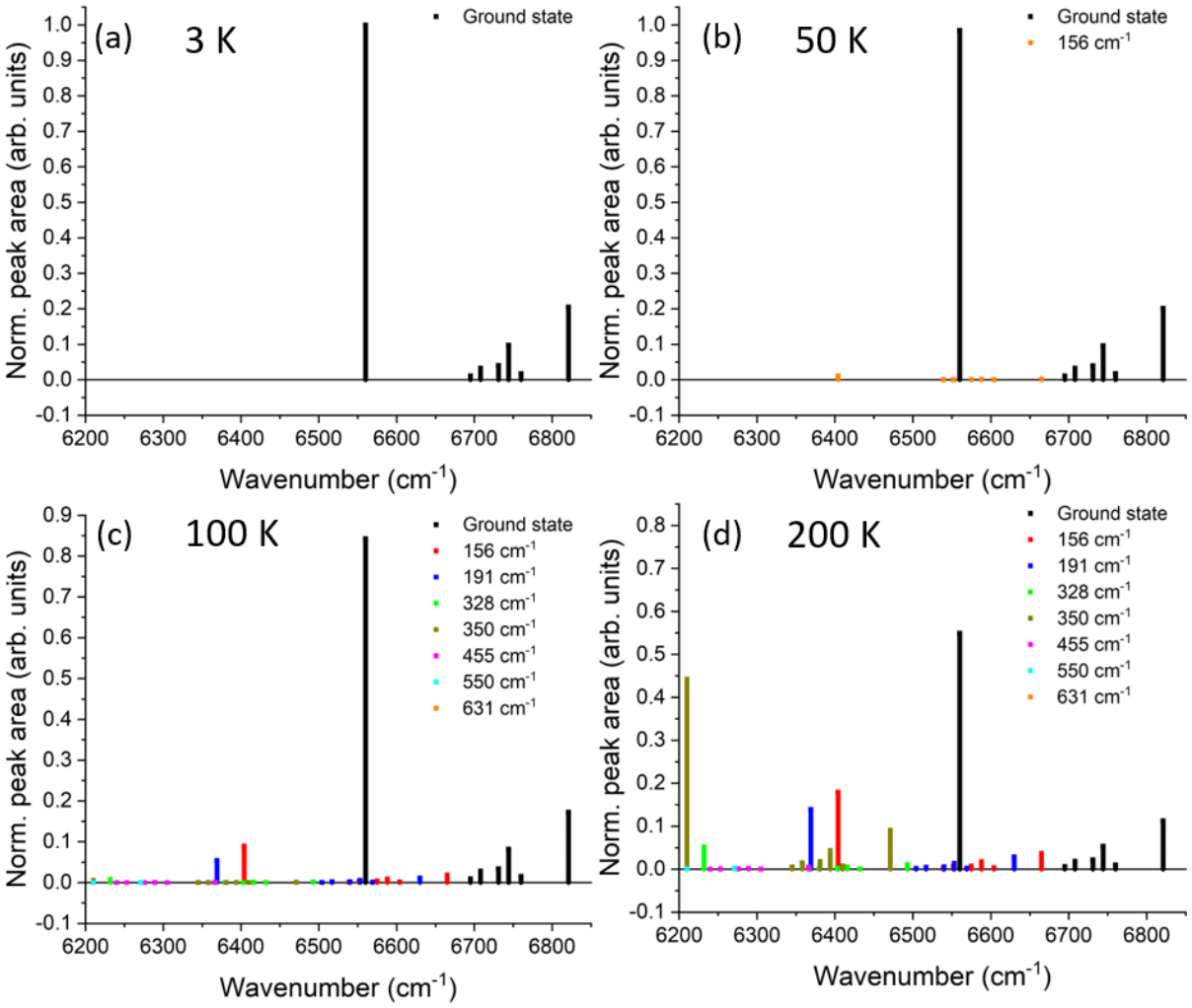

Figure D2. Normalized peak areas representing the simulated absorbance of Er(III) from the $^4I_{15/2}$ manifold to the $^4I_{13/2}$ manifold of Cp*ErCOT at, (a) 3 K, (b) 50 K, (c) 100 K and (d) 200 K. The legend indicates the initial energy level for transitions to all the 7 doublets of the excited manifold, as explained in Chapter 4.2.1.

Appendix E:
Matlab input file

This section shows the code used to estimate the population of the crystal field levels of the Er $^4I_{15/2}$ ground state multiplet of Cp*ErCOT, based on published simulations of the energy positions of those states.[44]

```
clear all; %erase all variables in workspace

kB=0.695; %Boltzman in cm-1/K, while it is 8.617E-5  in eV
TT=1:1:300; % T dependence
T=3;        % T is starting

D_1=0;              % values taken from CASSCF simulations in literature
D_2=112;
D_3=125;
D_4=146.8;
D_5=158.8;
D_6=194.8;
D_7=209.9;
D_8=303.8;

Ztot= exp(-D_1 ./(kB*TT))+ exp(-D_2 ./(kB*TT))+exp(-D_3 ./(kB*TT))+exp(-D_4
./(kB*TT))+exp(-D_5 ./(kB*TT))+exp(-D_6 ./(kB*TT))+exp(-D_7
./(kB*TT))+exp(-D_8 ./(kB*TT)); %Partition function Z (Boltzman statistics)

Z_1= exp(-D_1 ./(kB*TT)) ./Ztot;
figure(1)
plot(TT, Z_1) %for plotting partition fuction vs temperature
xlabel('Temperature (K)')
ylabel('Occupation level 1')
xy = [TT(:), Z_1(:)];
dlmwrite('Peak_1.txt', xy, 'delimiter', ',');

Z_2= exp(-D_2 ./(kB*TT)) ./Ztot;
figure(2)
plot(TT, Z_2) %for plotting partition fuction vs temperature
xlabel('Temperature (K)')
ylabel('Occupation level 2')
xy = [TT(:), Z_2(:)];
dlmwrite('Peak_2.txt', xy, 'delimiter', ',');

Z_3= exp(-D_3 ./(kB*TT)) ./Ztot;
figure(3)
plot(TT, Z_3) %for plotting partition fuction vs temperature
xlabel('Temperature (K)')
ylabel('Occupation level 3')
xy = [TT(:), Z_3(:)];
dlmwrite('Peak_3.txt', xy, 'delimiter', ',');
```

```
Z_4= exp(-D_4 ./(kB*TT)) ./Ztot;
figure(4)
plot(TT, Z_4) %for plotting partition fuction vs temperature
xlabel('Temperature (K)')
ylabel('Occupation level 4')
xy = [TT(:), Z_4(:)];
dlmwrite('Peak_4.txt', xy, 'delimiter', ',');

Z_5= exp(-D_5 ./(kB*TT)) ./Ztot;
figure(5)
plot(TT, Z_5) %for plotting partition fuction vs temperature
xlabel('Temperature (K)')
ylabel('Occupation level 5')
xy = [TT(:), Z_5(:)];
dlmwrite('Peak_5.txt', xy, 'delimiter', ',');

Z_6= exp(-D_6 ./(kB*TT)) ./Ztot;
figure(6)
plot(TT, Z_6) %for plotting partition fuction vs temperature
xlabel('Temperature (K)')
ylabel('Occupation level 6')
xy = [TT(:), Z_6(:)];
dlmwrite('Peak_6.txt', xy, 'delimiter', ',');

Z_7= exp(-D_7 ./(kB*TT)) ./Ztot;
figure(7)
plot(TT, Z_7) %for plotting partition fuction vs temperature
xlabel('Temperature (K)')
ylabel('Occupation level 7')
xy = [TT(:), Z_7(:)];
dlmwrite('Peak_7.txt', xy, 'delimiter', ',');

Z_8= exp(-D_8 ./(kB*TT)) ./Ztot;
figure(8)
plot(TT, Z_8) %for plotting partition fuction vs temperature
xlabel('Temperature (K)')
ylabel('Occupation level 8')
xy = [TT(:), Z_8(:)];
dlmwrite('Peak_8.txt', xy, 'delimiter', ',');
```

Bibliography

1. Sessoli, R. *et al.* High-spin molecules: $[Mn_{12}O_{12}(O_2CR)_{16}(H_2O)_4]$. *J. Am. Chem. Soc.* **115**, 1804–1816 (1993).

2. Sessoli, R., Gatteschi, D., Caneschi, A. & Novak, M. A. Magnetic bistability in a metal-ion cluster. *Nature* **365**, 141–143 (1993).

3. Gao, S. *Molecular Nanomagnets and Related Phenomena*. *Structure and Bonding* (Springer Berlin Heidelberg, 2015). doi:10.1007/978-3-662-45723-8

4. Sanvito, S. Molecular spintronics. *Chem. Soc. Rev.* **40**, 3336 (2011).

5. Rocha, A. R. *et al.* Towards molecular spintronics. *Nat. Mater.* **4**, 335–339 (2005).

6. Sorace, L., Benelli, C. & Gatteschi, D. Lanthanides in molecular magnetism: old tools in a new field. *Chem. Soc. Rev.* **40**, 3092 (2011).

7. Gaita-Ariño, A., Luis, F., Hill, S. & Coronado, E. Molecular spins for quantum computation. *Nat. Chem.* **11**, 301–309 (2019).

8. Rinehart, J. D. & Long, J. R. Exploiting single-ion anisotropy in the design of f-element single-molecule magnets. *Chem. Sci.* **2**, 2078–2085 (2011).

9. Vincent, A. H., Whyatt, Y. L., Chilton, N. F. & Long, J. R. Strong Axiality in a Dysprosium(III) Bis(borolide) Complex Leads to Magnetic Blocking at 65 K. *J. Am. Chem. Soc.* **145**, 1572–1579 (2023).

10. Ishikawa, N., Sugita, M., Ishikawa, T., Koshihara, S. & Kaizu, Y. Lanthanide Double-Decker Complexes Functioning as Magnets at the Single-Molecular Level. *J. Am. Chem. Soc.* **125**, 8694–8695 (2003).

11. Le Roy, J. J. *et al.* An Organometallic Building Block Approach To Produce a Multidecker 4 f Single-Molecule Magnet. *J. Am. Chem. Soc.* **135**, 3502–3510 (2013).

12. Corradini, V. *et al.* Probing magnetic coupling between LnPc2 (Ln = Tb, Er) molecules and the graphene/Ni (111) substrate with and without Au-intercalation: Role of the dipolar field. *Nanoscale* **10**, 277–283 (2018).

13. Bernbeck, M. G., Hilgar, J. D. & Rinehart, J. D. Probing axial anisotropy in dinuclear alkoxide-bridged Er–COT single-molecule magnets. *Polyhedron* **175**, 114206 (2020).

14. Vanjak, J. C. *et al.* A High-Performance Single-Molecule Magnet Utilizing Dianionic Aminoborolide Ligands. *J. Am. Chem. Soc.* **144**, 17743–17747 (2022).

15. Hilgar, J. D., Bernbeck, M. G., Flores, B. S. & Rinehart, J. D. Metal-ligand pair anisotropy in a series of mononuclear Er-COT complexes. *Chem. Sci.* **9**, 7204–7209 (2018).

16. Jiang, S.-D. *et al.* Series of Lanthanide Organometallic Single-Ion Magnets. *Inorg. Chem.* **51**, 3079–3087 (2012).

17. Guo, F. S. *et al.* Magnetic hysteresis up to 80 kelvin in a dysprosium metallocene single-molecule magnet. *Science.* **362**, 1400–1403 (2018).

18. Dreiser, J. Molecular lanthanide single-ion magnets: From bulk to submonolayers. *J. Phys. Condens. Matter* **27**, (2015).

19. Stepanow, S. *et al.* Spin and Orbital Magnetic Moment Anisotropies of Monodispersed Bis(Phthalocyaninato)Terbium on a Copper Surface. *J. Am. Chem. Soc.* **132**, 11900–11901 (2010).

20. Westerström, R. *et al.* Surface Aligned Magnetic Moments and Hysteresis of an Endohedral Single-Molecule Magnet on a Metal. *Phys. Rev. Lett.* **114**, 087201 (2015).

21. Gonidec, M. *et al.* Surface Supramolecular Organization of a Terbium(III) Double-Decker Complex on Graphite and its Single Molecule Magnet Behavior. *J. Am. Chem. Soc.* **133**, 6603–6612 (2011).

22. Klar, D. *et al.* Hysteretic behaviour in a vacuum deposited submonolayer of single ion magnets. *Dalt. Trans.* **43**, 10686–10689 (2014).

23. Mannini, M. *et al.* Magnetic memory of a single-molecule quantum magnet wired to a gold surface. *Nat. Mater.* **8**, 194–197 (2009).

24. Serrano, G. *et al.* Magnetic bistability of a $TbPc_2$ submonolayer on a graphene/SiC(0001) conductive electrode. *Nanoscale* **10**, 2715–2720 (2018).

25. Koutsouflakis, E. *et al.* Metamagnetic transition and a loss of magnetic hysteresis caused by electron trapping in monolayers of single-molecule magnet Tb2 @C_{79}N. *Nanoscale* **14**, 9877–9892 (2022).

26. Wäckerlin, C. *et al.* Giant Hysteresis of Single-Molecule Magnets Adsorbed on a Nonmagnetic Insulator. *Adv. Mater.* **28**, 5195–5199 (2016).

27. Studniarek, M. *et al.* Understanding the Superior Stability of Single-Molecule Magnets on an Oxide Film. *Adv. Sci.* **1901736**, 1901736 (2019).

28. Cope, A. C. & Overberger, C. G. The Synthesis of Cycloöctatetraene from Pseudopelletierine. *J. Am. Chem. Soc.* **69**, 976 (1947).

29. Willstätter, R. & Waser, E. Über Cyclo-octatetraen. *Berichte der Dtsch. Chem. Gesellschaft* **44**, 3423–3445 (1911).

30. Avdeef, A., Raymond, K. N., Hodgson, K. O. & Zalkin, A. Two Isostructural Actinide π Complexes. The Crystal and Molecular Structure of Bis(cyclooctatetraenyl)uranium(IV), $U(C_8H_8)_2$, and Bis(cyclooctatetraenyl)thorium(IV), $Th(C_8H_8)_2$. *Inorg. Chem.* **11**, 1083–1088 (1972).

31. Wayda, A. L., Cheng, S. & Mukerji, I. Cyclooctatetraenide derivatives of divalent samarium. *J. Organomet. Chem.* **330**, C17–C19 (1987).

32. Meihaus, K. R. & Long, J. R. Magnetic blocking at 10 K and a Dipolar-mediated avalanche in salts of the bis(η8-cyclooctatetraenide) complex $[Er(COT)_2]^-$. *J. Am. Chem. Soc.* **135**, 17952–17957 (2013).

33. Ungur, L., Leroy, J. J., Korobkov, I., Murugesu, M. & Chibotaru, L. F. Fine-tuning the local symmetry to attain record blocking temperature and magnetic remanence in a single-ion magnet. *Angew. Chemie - Int. Ed.* **53**, 4413–4417 (2014).

34. Le Roy, J. J., Ungur, L., Korobkov, I., Chibotaru, L. F. & Murugesu, M. Coupling strategies to

enhance single-molecule magnet properties of erbium-cyclooctatetraenyl complexes. *J. Am. Chem. Soc.* **136**, 8003–8010 (2014).

35. Hilgar, J. D., Bernbeck, M. G. & Rinehart, J. D. Million-fold Relaxation Time Enhancement across a Series of Phosphino-Supported Erbium Single-Molecule Magnets. *J. Am. Chem. Soc.* **141**, 1913–1917 (2019).

36. Orlova, A. P., Hilgar, J. D., Bernbeck, M. G., Gembicky, M. & Rinehart, J. D. Intuitive Control of Low-Energy Magnetic Excitations via Directed Dipolar Interactions in a Series of Er(III)-Based Complexes. *J. Am. Chem. Soc.* **144**, 11316–11325 (2022).

37. Le Roy, J. J., Korobkov, I. & Murugesu, M. A sandwich complex with axial symmetry for harnessing the anisotropy in a prolate erbium(iii) ion. *Chem. Commun.* **50**, 1602–1604 (2014).

38. Jiang, S.-D., Wang, B.-W., Sun, H.-L., Wang, Z.-M. & Gao, S. An Organometallic Single-Ion Magnet. *J. Am. Chem. Soc.* **133**, 4730–4733 (2011).

39. Korzyński, M. D. *et al.* Cyclooctatetraenide-based single-ion magnets featuring bulky cyclopentadienyl ligand. *Chem. Sci.* **13**, 10574–10580 (2022).

40. Ormaza, M. *et al.* Assembly of Ferrocene Molecules on Metal Surfaces Revisited. *J. Phys. Chem. Lett.* **6**, 395–400 (2015).

41. Bachellier, N. *et al.* Unveiling nickelocene bonding to a noble metal surface. *Phys. Rev. B* **93**, 1–6 (2016).

42. Boulon, M.-E. *et al.* Angular-Resolved Magnetometry Beyond Triclinic Crystals: Out-of-Equilibrium Studies of Cp*ErCOT Single-Molecule Magnet. *Chem. - A Eur. J.* **19**, 13726–13731 (2013).

43. Perfetti, M. *et al.* Angular-Resolved Magnetometry beyond Triclinic Crystals Part II: Torque Magnetometry of Cp∗ErCOT Single-Molecule Magnets. *Chem. - A Eur. J.* **20**, 14051–14056 (2014).

44. Baldoví, J. J., Clemente-Juan, J. M., Coronado, E. & Gaita-Ariño, A. Molecular anisotropy analysis of single-ion magnets using an effective electrostatic model. *Inorg. Chem.* **53**, 11323–11327 (2014).

45. Stöhr, J. & Siegmann, H. C. *Magnetism: From fundamentals to nanoscale dynamics*. *Magnetism: From Fundamentals to Nanoscale Dynamics* (Springer Berlin Heidelberg, 2006). doi:10.1007/978-3-540-30283-4

46. Tang, J. & Zhang, P. Polynuclear Lanthanide Single Molecule Magnets. in *Lanthanides and Actinides in Molecular Magnetism* 61–88 (Wiley-VCH Verlag GmbH & Co. KGaA, 2015). doi:10.1002/9783527673476.ch3

47. Woodruff, D. N., Winpenny, R. E. P. & Layfield, R. A. Lanthanide Single-Molecule Magnets. *Chem. Rev.* **113**, 5110–5148 (2013).

48. Malta, O. L. & Carlos, L. D. Intensities of 4f-4f transitions in glass materials. *Quim. Nova* **26**, 889–895 (2003).

49. Flanagan, B. M., Bernhardt, P. V., Krausz, E. R., Lüthi, S. R. & Riley, M. J. Ligand-field analysis of an Er(III) complex with a heptadentate tripodal N_4O_3 ligand. *Inorg. Chem.* **40**, 5401–5407 (2001).

50. Grimm, M., Beckert, A., Aeppli, G. & Müller, M. Universal Quantum Computing Using Electronuclear Wavefunctions of Rare-Earth Ions. *PRX Quantum* **2**, 1 (2021).

51. Hakkel, K. D. *et al.* Integrated near-infrared spectral sensing. *Nat. Commun.* **13**, 103 (2022).

52. Ozaki, Y., Huck, C. W. & Beć, K. B. Near-IR Spectroscopy and Its Applications. in *Molecular and Laser Spectroscopy* 11–38 (Elsevier, 2018). doi:10.1016/B978-0-12-849883-5.00002-4

53. Grimm, M., Beckert, A., Aeppli, G. & Müller, M. Universal Quantum Computing Using Electronuclear Wavefunctions of Rare-Earth Ions. *PRX Quantum* **2**, 010312 (2021).

54. Klintenberg, M., Edvardsson, S. & Thomas, J. O. Energy level and oscillator strength calculations for Er^{3+}:Y_2O_3: A molecular dynamics based study. *J. Alloys Compd.* **275**–**277**, 174–176 (1998).

55. Irfanullah, M. & Iftikhar, K. The Correlation Between f–f Absorption and Sensitized Visible Light Emission of Luminescent Pr(III) Complexes: Role of Solvents and Ancillary Ligands on Sensitivity. *J. Fluoresc.* **21**, 673–686 (2011).

56. Alonso, P. J. & Martínez, J. I. Magnetic properties of a Kramers doublet. An univocal bridge between experimental results and theoretical predictions. *J. Magn. Reson.* **255**, 1–14 (2015).

57. Münzfeld, L. *et al.* Synthesis, structures and magnetic properties of [(η^9-C_9H_9)Ln(η^8-C_8H_8)] super sandwich complexes. *Nat. Commun.* **10**, 1–7 (2019).

58. Lunghi, A. & Sanvito, S. Multiple spin-phonon relaxation pathways in a Kramer single-ion magnet. *J. Chem. Phys.* **153**, (2020).

59. A. Balerna & S. Mobilio. *Synchrotron Radiation*. *Synchrotron Radiation: Basics, Methods and Applications* (Springer Berlin Heidelberg, 2015). doi:10.1007/978-3-642-55315-8

60. Van Der Laan, G. & Figueroa, A. I. X-ray magnetic circular dichroism - A versatile tool to study magnetism. *Coord. Chem. Rev.* **277**, 95–129 (2014).

61. Thole, B. T., Carra, P., Sette, F. & van der Laan, G. X-ray circular dichroism as a probe of orbital magnetization. *Phys. Rev. Lett.* **68**, 1943–1946 (1992).

62. Carra, P., Thole, B. T., Altarelli, M. & Wang, X. X-ray circular dichroism and local magnetic fields. *Phys. Rev. Lett.* **70**, 694–697 (1993).

63. Šipr, O., Minár, J. & Ebert, H. On the importance of the magnetic dipole term T z in analyzing X-ray magnetic circular dichroism spectra of clusters. *Europhys. Lett.* **87**, 67007 (2009).

64. Teramura, Y., Tanaka, A., Thole, B. T. & Jo, T. Effect of Coulomb Interaction on the X-Ray Magnetic Circular Dichroism Spin Sum Rule in Rare Earths. *J. Phys. Soc. Japan* **65**, 3056–3059 (1996).

65. Piamonteze, C., Miedema, P. & de Groot, F. M. F. Accuracy of the spin sum rule in XMCD for the transition-metal *L* edges from manganese to copper. *Phys. Rev. B* **80**, 184410 (2009).

66. Uldry, A., Vernay, F. & Delley, B. Systematic computation of crystal-field multiplets for x-ray core spectroscopies. *Phys. Rev. B* **85**, 125133 (2012).

67. Baltic, R. *et al.* Magnetic properties of single rare-earth atoms on graphene/Ir(111). *Phys. Rev. B* **98**, 024412 (2018).

68. Wäckerlin, C. *et al.* Strong antiferromagnetic exchange between manganese phthalocyanine and ferromagnetic europium oxide. *Chem. Commun.* **51**, 12958–12961 (2015).

69. Wäckerlin, C. *et al.* Role of the Magnetic Anisotropy in Atomic-Spin Sensing of 1D Molecular Chains. *ACS Nano* **16**, 16402–16413 (2022).

70. Yeh, J. J. & Lindau, I. Atomic subshell photoionization cross sections and asymmetry parameters: $1 \leqslant Z \leqslant 103$. *At. Data Nucl. Data Tables* **32**, 1–155 (1985).

71. Griffiths, P. R. Fourier Transform Infrared Spectrometry. *Science.* **222**, 297–302 (1983).

72. Chen, C. J. *Introduction to Scanning Tunneling Microscopy*. *Monographs on the Physics and Chemistry of Materials* (Oxford University PressOxford, 2007). doi:10.1093/acprof:oso/9780199211500.001.0001

73. Piamonteze, C. *et al.* X-Treme beamline at SLS: X-ray magnetic circular and linear dichroism at high field and low temperature. *J. Synchrotron Radiat.* **19**, 661–674 (2012).

74. Muntwiler, M. *et al.* Surface science at the PEARL beamline of the Swiss Light Source. *J. Synchrotron Radiat.* **24**, 354–366 (2017).

75. Nečas, D. & Klapetek, P. Gwyddion: An open-source software for SPM data analysis. *Cent. Eur. J. Phys.* **10**, 181–188 (2012).

76. Lerch, P. *et al.* IR beamline at the Swiss Light Source. *J. Phys. Conf. Ser.* **359**, 012003 (2012).

77. Bruin, P., Booij, M., Teuben, J. H. & Oskam, A. Mixed sandwiches of group 3 elements: synthesis and UPS studies of pentamethylcyclopentadienylcyclooctatetraenescandium, -yttrium and -lanthanum. *J. Organomet. Chem.* **350**, 17–23 (1988).

78. Seah, M. P. & Dench, W. A. Quantitative Electron Spectroscopy. *Surf. Interface Anal.* **1**, (1979).

79. Tas, S., Kaynan, O., Ozden-Yenigun, E. & Nijmeijer, K. Polyacrylonitrile (PAN)/crown ether composite nanofibers for the selective adsorption of cations. *RSC Adv.* **6**, 3608–3616 (2016).

80. Johnston, E. E., Bryers, J. D. & Ratner, B. D. Plasma deposition and surface characterization of oligoglyme, dioxane, and crown ether nonfouling films. *Langmuir* **21**, 870–881 (2005).

81. Zhuang, G. R., Wang, K., Chen, Y. & Ross, P. N. Study of the reactions of Li with tetrahydrofuran and propylene carbonate by photoemission spectroscopy. *J. Vac. Sci. Technol. A Vacuum, Surfaces, Film.* **16**, 3041–3045 (1998).

82. Romankov, V. *et al.* Influence of self-assembly on the magnetic properties of Er(III) cyclooctatetraenide-based single-molecule magnets deposited on Ag(100). Manuscript in preparation.

83. Groenenboom, C. J., Sawatzky, G., de Liefde Meijer, H. J. & Jellinek, F. Electron spectroscopy of some cyclopentadienylcycloheptatrienylmetal compounds. *J. Organomet. Chem.* **76**, C4–C6 (1974).

84. Woodbridge, C. M., Pugmire, D. L., Johnson, R. C., Boag, N. M. & Langell, M. A. HREELS and XPS Studies of Ferrocene on Ag(100). *J. Phys. Chem. B* **104**, 3085–3093 (2000).

85. Briganti, M. *et al.* Mixed-Sandwich Titanium(III) Qubits on Au(111): Electron Delocalization Ruled by Molecular Packing. *Nano Lett.* **22**, 8626–8632 (2022).

86. Mao, C. *et al.* Effect of Er doping on microstructure and optical properties of ZnO thin films prepared by sol–gel method. *J. Mater. Sci. Mater. Electron.* **26**, 8732–8739 (2015).

87. Oh, S., Seo, J., Choi, G. & Lee, H. S. Understanding adsorption geometry of organometallic molecules on graphite. *Sci. Rep.* **11**, 18497 (2021).

88. Ormaza, M. *et al.* Assembly of ferrocene molecules on metal surfaces revisited. *J. Phys. Chem. Lett.* **6**, 395–400 (2015).

89. Huttmann, F. *et al.* Europium Cyclooctatetraene Nanowire Carpets: A Low-Dimensional, Organometallic, and Ferromagnetic Insulator. *J. Phys. Chem. Lett.* **10**, 911–917 (2019).

90. Singha, A. *et al.* ^{4}f occupancy and magnetism of rare-earth atoms adsorbed on metal substrates. *Phys. Rev. B* **96**, 224418 (2017).

91. Dreiser, J. *et al.* Out-of-Plane Alignment of Er(trensal) Easy Magnetization Axes Using Graphene. *ACS Nano* **10**, 2887–2892 (2016).

92. Teramura, Y., Tanaka, A. & Jo, T. Effect of Coulomb Interaction on the X-Ray Magnetic Circular Dichroism Spin Sum Rule in 3 d Transition Elements. *J. Phys. Soc. Japan* **65**, 1053–1055 (1996).

93. Jiang, S. Da, Wang, B. W., Sun, H. L., Wang, Z. M. & Gao, S. An organometallic single-ion magnet. *J. Am. Chem. Soc.* **133**, 4730–4733 (2011).

94. Kraus, S. *et al.* Uniaxially Aligned 1D Sandwich-Molecular Wires: Electronic Structure and Magnetism. *J. Phys. Chem. C* **126**, 3140–3150 (2022).

95. Chambers, S. A. *et al.* Band alignment, built-in potential, and the absence of conductivity at the $LaCrO_3/SrTiO_3$(001) heterojunction. *Phys. Rev. Lett.* **107**, 206802 (2011).

96. Taucher, T. C., Hehn, I., Hofmann, O. T., Zharnikov, M. & Zojer, E. Understanding Chemical versus Electrostatic Shifts in X-ray Photoelectron Spectra of Organic Self-Assembled Monolayers. *J. Phys. Chem. C* **120**, 3428–3437 (2016).

97. Cano, A. *et al.* Relevant electronic interactions related to the coordination chemistry of tetracyanometallates. An XPS study. *New J. Chem.* **43**, 18384–18393 (2019).

98. Ayyoob, M. & Hegde, M. S. An XPS study of the adsorption of oxygen on silver and platinum surfaces covered with potassium or cesium. *Surf. Sci.* **133**, 516–532 (1983).

99. Kalugin, N. G., Roy, A. J., Artyushkova, K. & Serov, A. Synthesis, characterization, and photoluminescence of Er_2O_3–Er_2SO_2 nanoparticles on reduced graphene oxide. *Nanotechnology* **28**, 195603 (2017).

100. Chase, S. J., Bacsa, W. S., Mitch, M. G., Pilione, L. J. & Lannin, J. S. Surface-enhanced Raman scattering and photoemission of C60 on noble-metal surfaces. *Phys. Rev. B* **46**, 7873–7877 (1992).

101. Tsuei, K. D. & Yuh, J. Y. Photoemission and photoabsorption study of adsorption on Cu(111) surfaces. *Phys. Rev. B - Condens. Matter Mater. Phys.* **56**, 15412–15420 (1997).

102. Akimov, A. V., Williams, C. & Kolomeisky, A. B. Charge Transfer and Chemisorption of Fullerene Molecules on Metal Surfaces: Application to Dynamics of Nanocars. *J. Phys. Chem. C* **116**, 13816–13826 (2012).

103. Hoogenboom, B., Hesper, R., Tjeng, L. & Sawatzky, G. Charge transfer and doping-dependent

hybridization of on noble metals. *Phys. Rev. B - Condens. Matter Mater. Phys.* **57**, 11939–11942 (1998).

104. Hunt, M. R. C., Modesti, S., Rudolf, P. & Palmer, R. E. Charge transfer and structure in C60 adsorption on metal surfaces. *Phys. Rev. B* **51**, 10039–10047 (1995).

105. Dreiser, J. *et al.* X-ray induced demagnetization of single-molecule magnets. *Appl. Phys. Lett.* **105**, 032411 (2014).

106. Romankov, V. *et al.* Optical access to rotammer-split 4f levels of Er(III) cyclooctatetraenide-based single-molecule magnets. Manuscript in preparation.

107. Bhattacharjee, S. & Chattopadhyay, K. K. Laser-induced Fano asymmetry, electron-phonon coupling, and phase transition in lanthanide sesquioxide (Ln_2O_3 ; Ln = Eu, Gd, Dy) nanoparticles: A Raman spectroscopic investigation. *J. Appl. Phys.* **132**, 215107 (2022).

108. Inc., T. M. MATLAB version 9.13.0 (R2022b). (2022).

109. Ramanantoanina, H. A DFT-based theoretical model for the calculation of spectral profiles of lanthanide M4,5-edge x-ray absorption. *J. Chem. Phys.* **149**, (2018).

110. Mohammadi, N., Ganesan, A., Chantler, C. T. & Wang, F. Differentiation of ferrocene D5d and D5h conformers using IR spectroscopy. *J. Organomet. Chem.* **713**, 51–59 (2012).

111. De Camargo, L. C. *et al.* Exploring the Organometallic Route to Molecular Spin Qubits: The [CpTi(cot)] Case. *Angew. Chemie - Int. Ed.* **60**, 2588–2593 (2021).

112. Appel, M., Frick, B., Spehr, T. L. & Stühn, B. Molecular ring rotation in solid ferrocene revisited. *J. Chem. Phys.* **142**, 114503 (2015).